Master's thesis

NTNU
Norwegian University of Science and Technology
Faculty of Natural Sciences
Department of Materials Science and Engineering

Vegard Vesterdal Viki

Computational Prediction and Characterisation of Novel Li-ion Solid Electrolytes based on Earth Abundant LiSiNO

Master's thesis in Chemical Engineering and Biotechnology
Supervisor: Sverre Magnus Selbach
Co-supervisor: Benjamin Williamson
July 2022

NTNU
Norwegian University of
Science and Technology

Vegard Vesterdal Viki

Computational Prediction and Characterisation of Novel Li-ion Solid Electrolytes based on Earth Abundant LiSiNO

Master's thesis in Chemical Engineering and Biotechnology
Supervisor: Sverre Magnus Selbach
Co-supervisor: Benjamin Williamson
July 2022

Norwegian University of Science and Technology
Faculty of Natural Sciences
Department of Materials Science and Engineering

NTNU
Norwegian University of
Science and Technology

Preface

This master's thesis is a result of the specialisation course *TMT4900 - Materials Technology, Master's Thesis* at the Department of Materials Science and Technology at the Norwegian University of Technology and Science.

Acknowledgements

I would like to thank my supervisors Prof. Sverre M. Selbach, Post Doc. Dr. Benjamin Williamson and Kristoffer Eggestad for helping me throughout the semester. I would especially thank Sverre for his help in guiding me through the writing process and Ben and Kristoffer for helping me familiarise with VASP and UNIX, and helping me with the calculations. I definitevly could not have made it without their help. I would also like to thank everyone in the FACET group for their input and guidance, as well as all my fellow students helping me get through this semester. Lastly i would like to thank all the Sous-chefs and chefs at UKA for all the good times.

Abstract

All solid-state batteries(ASSB) based on solid-state electrolytes(SSE) are a promising solution to contemporary battery technology's current safety issues. The LiSiNO structure has previously shown great promise for the use as solid-state electrolyte based on its very large band gap and preferable Li-ion migration paths. In this master thesis, the possibilities of improving the properties of LiSiNO by the creation of $LiSi_{1-x}Ge_xNO$ and $LiSiNO_{1-x}S_x$ solid-solutions are being explored. Density functional theory(DFT) calculations with the PBEsol functional are being used to calculate 25%, 50% and 75% substitutions of $LiSi_{1-x}Ge_xNO$ and $LiSiNO_{1-x}S_x$. This thesis aims to analyse the enthalpy- and Gibb's free energy of mixing for the two solid-solution systems. Additionally, the density of states and band-gap will be calculated to get an approximation of the electrochemical stability window of the materials. Finally, the Li-ion mobility will be investigated using a machine-learning Molecular dynamics(ML-MD) method for all the structures and nudged elastic band(NEB) calculations will calculate possible Li migration paths for $LiSiNO_{0.75}S_{0.25}$.

The two solid-solution systems both have a positive enthalpy of mixing and Gibb's free energy of mixing. The investigated solid-solutions also closely followed Vegard's rule, except from $LiSiNO_0.25S_{0.75}$ which negatively deviated from linearity. The electronic structure analysis showed a decrease in band-gap with increasing Ge and S substitution. However, the solid-solutions still performed favourably compared to competing solid electrolytes such as LISICON, LLTO and LGPS. A short-term ML-MD analysis of 100 ps demonstrated an improvement in Li-ion mean square displacement(MSD) for LiSiNO when substituting with 25 and 50% S. However, the substitution of Si for Ge showed no impact on Li-ion MSD. The long-term ML-MD simulation of 10 ns further supported the reliability of the short-term simulation results by producing similar trends. However, no diffusion regime was achieved. The NEB analysis for $LiSiNO_{0.75}S_{0.25}$ produced three Li-paths equivalent to the three found in LiSiNO and LiSiNS. The three migration paths had migration energy barriers of 0.31 eV, 0.65 eV and 0.24 eV, respectively. Here the migration barrier improved from LiSiNO for the first path but increased for path 2 and 3. However the migration barrier for path 3 was still substantially low. The results thus showed that $LiSiNO_{1-x}S_x$ solid-solutions could be beneficial for producing better Li-ion migration at a relatively lower cost in band-gap, while the $LiSi_{1-x}Ge_xNO$ solid-solutions only lowered the band-gap without seemingly impacting the Li mobility. conclusion

Sammendrag

"All solid-state-batterier" (ASSB) basert på faststoff elektrolytter (SSE) er en lovende løsning på de nåværende sikkerhetsproblemene som moderne batteriteknologi står ovenfor. LiSiNO-strukturen har tidligere vist seg lovende for bruk som faststoffelektrolytt basert på sitt stor båndgap og gunstige Li-ion migrasjonsveier. I denne masteroppgaven er mulighetene for å forbedre egenskapene til LiSiNO ved å lage $LiSi_{1x}Ge_xNO$ og $LiSiNO_{1x}S_x$ solide løsninger utforskes. Density functional theory (DFT) beregninger med "PBE- sol-functional" brukes for beregne 25%, 50% og 75% substitusjoner av $LiSi_{1x}Ge_xNO$ og $LiSiNO_{1x}S_x$. Målet med oppgaven er å analysere entalpi- og Gibbs frie energi av mixing for de to faststoffløsning systemene. I tillegg vil "density of states" og båndgap bli beregnet for å få en tilnærming av det elektrokjemiske stabilitetsvinduet til materialene. Til slutt vil Li-ion mobiliteten bli undersøkt ved hjelp av en maskinlæring "Molecular Dynamics" (ML-MD) metode for alle strukturene og "nudged elastic band" (NEB) beregninger vil beregne mulige Li-migrasjonsveier for $LiSiNO_{0.75}S_{0.25}$.

De to faststoffløsningssystemene ble begge funnet til å ha positiv blandingsentalpi og Gibbs frie energi for mixing. Vegards lov ble også nært fulgt av de undersøkte faststoffløsningene, bortsett fra LiSiNO0.25S0.75 som negativt avvek fra linearitet. Analysen av den elektroniske strukturen viste videre en nedgang i båndgap med økende Ge- og S-substitusjon. Faststoffløsningene presterte fortsatt gunstig sammenlignet med konkurrerende faste elektrolytter slik som LISICON, LLTO og LGPS. Den kortsiktige ML-MD analysen på 100 ps demonstrerte en forbedring i Li-ion mean square displacement(MSD) for LiSiNO ved erstatning med 25% og 50% S, men substitusjonen av Si for Ge viste ingen innvirkning på Li-ion MSD. De langsiktig ML-MD-simulering på 10 ns støttet ytterligere påliteligheten til kort sikt simuleringsresultater ved å produsere de samme trendene, men dessverre ble ingen diffusjonsregime oppnådd. NEB-analysen for $LiSiNO_{0.75}S_{0.25}$ produserte tre Li-migrationsveier som var ekvivalente med de funnet i LiSiNO og LiSiNS. De tre migrasjonsveiene hadde migrasjonsenergibarrierer på 0.31 eV, 0.65 eV og 0.24 eV henholdsvis. Her ble migrasjonsbarrieren forbedret fra LiSiNO for første vei, men økt for vei 2 og 3. Migrasjonsbarrieren for vei 3 var imidlertid fortsatt betydelig lav. Resultatene viste dermed at $LiSiNO_{1-x}S_x$ kan være gunstig for å produsere bedre Li-ion-migrering på bekostning av en relativt lav kostnad i båndgap, mens $LiSi_{1x}Ge_xNO$ faststoffløsningene bare senket båndgapet uten å tilsynelatende påvirke Li-mobiliteten.

Table of Contents

1 Background

1.1 Motivation

The global electric vehicle and energy storage system markets are among the fastest growing markets in the world[1]. As the global society are searching for greener technology as alternatives for fossil fuel based solutions, the demand for energy storage are continuously increasing. Li-ion batteries (LiB) are currently the most favoured choice of battery technology. All contemporary electric vehicles are based on Li-ion battery technology, while Li-ion batteries also possesses a large market share for newer energy storage systems[2][3]. Li-ion batteries are massively favoured due to its very high theoretical capacity and long cycle life[4]. Current LiB technology however exhibit certain issues regarding safety and stability. Some of the safety issues are due to the high flammability and instability of their liquid organic electrolytes. The battery cells can undergo thermal runaway leading to fire or combustion, when the cell are subjected to deformations or short-circuiting. Additionally, as the market evolves a growing need for improved Li-ion batteries are needed. Therefore improved electrolytes are needed to utilise more advanced cathodes and anodes.

A proposed solution to the safety challenges of liquid organic electrolytes are all solid-state batteries(ASSB). These batteries substitute the liquid electrolyte with solid-state materials. Solid-state electrolytes exhibit much higher thermodynamic stability, as well as enabling the possibility of use of metallic anodes which noticeably increase the energy density. A consequence of using metallic anodes together with liquid electrolytes is the formation Li-dendrites from the anodes and through the electrolyte. This process can cause short-circuiting and thermal runaway, deteriorating the battery cell. The biggest challenges with ASSB technology are combining high electrochemical stability together with high ionic conductivity. Recent effort in solid-state electrolyte research have been focused on improving the ionic conductivity at operating temperatures to reach levels on par with conventional Li-ion batteries. The biggest factor in improving the ionic conductivity is uncovering materials with crystal structure that have either enhanced paths for Li migration or the prospect of superionic conductivity. However, a very high ionic conductivity often come at the expense of electrochemical stability.

LiSiNO structured materials are recently discovered as candidates for the use as solid-electrolytes. LiSiNO, LiSiNS and LiGeNO all are stable materials and have the $Pca2_1$ space group. LiSiNO have previously been trialled as an amorphous electrolyte, where it achieved an ionic conductivity of $2.47{\cdot}10^{-6}$ S/cm[5]. Additionally have first principle calculations concluded the material to have a band-gap of 6.95 eV, thus indicating a very high electrochemical stability[6]. The sulfide material LiSiNS are expected to have higher ionic conductivity as a consequence of the softer sulfide anion lattice. However sulfide materials often have a lower electrochemical stability compared to oxide materials. A combination of high ionic conductivity and electrochemical stability might be possible by analysing potential solid-solutions between these three materials. Therefore are LiSiNO structured materials very promising materials to analyse for the use as solid-electrolytes.

1.2 Scope of the work

The scope of this master thesis involves analysing the electrochemical stability and Li migration of solid solutions between LiSiNO and LiGeNO, and LiSiNO and LiSiNS. The analysis will involve the structures $LiSi_{1-x}Ge_xNO$ and $LiSiNO_{1-x}S_x$, with 25%, 50% and 75% substitution. Density Functional Theory(DFT) will be used to simulate and geometry optimise each structure. From these calculated solid-solution the band-gap will be determined to get an insight into the electrochemical stability of the solid-solutions. The Li-ion migration will be analysed by performing Nudged elastic bands(NEB) analysis to investigate possible Li-ion migration paths in each structure. A further aim is to investigate the behaviour of Li diffusion by performing molecular dynamics simulations. The goal of the analysis is to achieve solid-solutions which shows a promising compromise between high electrochemical stability and ionic conductivity, by exhibiting a wide band-gap as well as migration paths with lower activation energy.

2 Introduction

2.1 Rechargeable Li-ion Batteries

Rechargeable batteries store energy in modern large-scale applications, such as energy-storing systems(ESS) and electric vehicles(EV). The main components in a modern secondary battery are an electrolyte, a separator and a negative and a positive electrode. When the battery is fully charged, all the charge will be stored at the negative electrode. Then, the charge carriers and the electrons will be separated to utilize the energy stored in the battery. The separation causes the charge carriers to migrate through the electrolyte and towards the positive electrode. Consequently, the electrons start to move through an external circuit towards the positive electrode producing a current. The current is then reversed when the cell is charged, and the charge carrier is transported back to the negative electrode through the electrolyte. Due to the transport of the charge carrier's integral part to the process, the most critical factors of a secondary battery are a high ionic conductivity, high thermodynamic and electrochemical stability of the electrolyte, low resistance between the electrolyte and the electrodes and low cost[7].

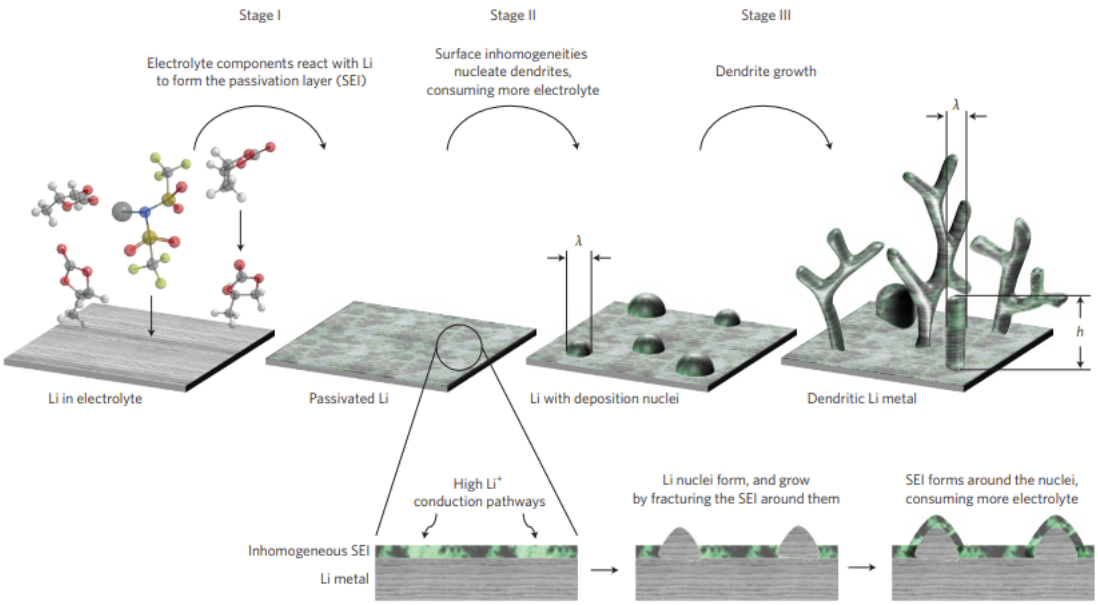

Figure 1: Illustration of the formation of Li dendrites through the liquid electrolyte in LiB using Li-metal anode. Figure adapted from Tikekar, M. D. et.al.[8]

Current commercial battery technology is based on Li-ions as charge carriers. The Li-ions are reversibly inserted into the electrodes during charge/discharge cycles. The electrodes are made of crystalline structures to enable this "intercalation". The ions are intercalated and stored in empty channels in the crystalline structure[9]. Currently, the most stable high voltage cathodes with the highest capacity are the lithium transition-oxide electrodes, while the most used anodes are made of graphite. A higher operating voltage is desired to improve the performance of Li-ion batteries. By utilising cathodes with higher voltage potential, one can further improve the charge

of the battery[10]. To utilise even higher voltage cathodes, an electrolyte with high electrochemical stability is needed for the electrolyte to not react with the cathode. Current commercial battery cells use a liquid organic electrolyte. Liquid organic electrolytes are chosen for their high ionic conductivity and stability at high voltage ranges[7]. However, these electrolytes are severely limited by their low thermal stability, resulting in high flammability. The capacity of Li-ion batteries can be significantly increased by utilising Li-metal anodes, which have a very high specific capacity at 3860 mAh/g and very low potential[11]. Li-ion batteries with Li-metal anodes would be a significant step towards breaking the current energy density bottleneck of current Li-ion technology. However, liquid organic electrolytes prevent the use of Li-metal anodes due to the formation of Li dendrites. As a result, a battery cell with a liquid organic electrolyte can catch fire under abuse conditions due to heat generation and possible oxygen production at the cathode[7]. The Li-ions in the electrolyte can react with the Li-metal anodes and create Li dendrites that penetrate through the electrolyte and eventually connect with the cathode. This connection leads to short-circuiting of the cell and thermal runaway. An illustration of dendrite formation through the cell is shown in figure 1 adapted from Mukul D. Tikekar et.al[8].

2.2 Solid-state electrolytes

All solid-state batteries(ASSB) are proposed as a solution to the current battery technology's safety challenges. An inorganic solid-state electrolyte would not come with the same concerns regarding flammability and therefore remove the current safety risks of thermal instability. An ASSB substitutes its liquid organic electrolyte with a solid-state electrolyte. Cationic single-ion conducting inorganic electrolytes are among the most favoured current SSEs. Solid-state materials usually have a higher charge carrier transport efficiency than liquid electrolytes due to their high ionic conductivity and low electronic conductivity[8]. An additional promising attribute of SSEs is the possibility of utilising bipolar electrodes. Bipolar electrodes will significantly increase the volumetric energy density due to the denser packing efficiency[8]. A solid-state electrolyte's inherent properties also open up the possibility of using a Li-metal anode in the battery cells. The use of Li-metal anodes would contribute to an increase in energy density.

A large amount of research from the latest decade has contributed to achieving SSEs with ionic conductivity approaching the levels of liquid inorganic electrolytes. However, further research is still needed to reach satisfactory levels at operating temperature. The technology still faces important challenges to be safely used in commercial battery cells. The electrode-electrolyte interface is one of the technology's most critical challenges[11]. The connectivity between the electrode material and the electrolyte is lacking due to the significant volume changes of the active material and the inflexibility of SSEs. This leads to concentrated contacts with increased resistivity between the electrode and electrolyte during charge/discharge cycles[12]. Li can additionally form on these contacts if Li-metal anodes are used. Thus dendrites can be produced from these contacts and further penetrate through the electrolyte along grain boundaries[13]. Electron conducting or ionically resistive decomposition products can also form at the anode[13]. A process called Li-metal plating can occur in ASSEs when such decomposition products form in possible voids at the electrode/electrolyte interface. This leads to smaller voids being trapped at the anode surface, eventually decreasing the amount of contact between electrolyte and anode. This process is illustrated in figure 2.

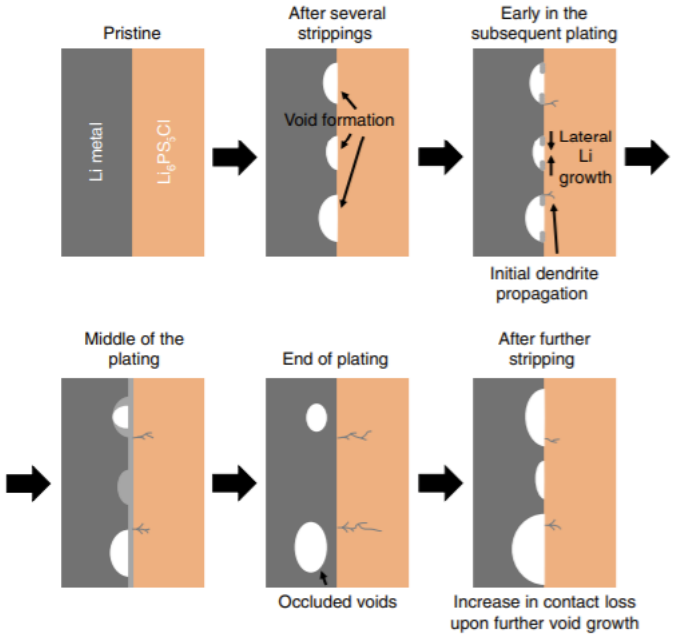

Figure 2: Illustration of void formation and plating with Li-metal anodes and SSE. Figure adopted from Kasemchainan, J.*et al.*[12]

2.3 Current Solid-State Electrolytes

Oxide and sulfide materials are among the most promising classes of current SSEs[14][15][16]. The best performing current oxide structures are the garnet type $Li_7La_3Za_2O_{12}$(LLZO), the perovskite $Li_3xLa_{2/3-x}TiO_3$ (LLTO), LISICON-type $Li_{2+2x}Zn_{1-x}GeO_4$ and NASICON-type $NaM_2(XO_4)_3$(M = Ge, Ti, Zr; X = S, P, As)[14][15]. The LLZO material can achieve high ionic conductivity levels at 10^{-3}-10^{-4}S/cm, having an average migration energy barrier at 0.35-0.4eV[14]. It does further have high thermodynamic stability vs Li at wide potential ranges and is thermally stable at higher temperature ranges. However, these levels are achieved by the cubic structure, which has proven to be challenging to stabilise. The band gap of LLZO has been measured at 5.5 eV, while it has also been calculated with the PBE functional to 4.3 eV.[17]. LLTO materials can achieve a high ionic conductivity at 10^{-3}S/cm, having an average migration energy barrier of 0.3-0.4eV[16]. However, this material often exhibits a lower ionic conductivity due to high grain boundary resistance. These electrolytes are stable in air at wide temperature ranges, although they are reduced in contact with Li at 1.5V[16]. A DFT analysis of the band-gap of LLTO has been performed with the GGA-PBE functional, where the band-gap was determined to be 2.56 eV[18]. The LISICON structures have an average migration energy barrier of 0.4-0.6eV, giving an ionic conductivity in the range of 10^{-7}-10^{-3}S/cm[16]. The advantage of these materials is their high thermodynamic stability at high temperatures. The lower ionic conductivity and stability towards Li though, have proven to be great challenges. However, by doping this structure, one can flatten the energy landscape resulting in a "superionic" conduction mechanism which gives a higher ionic conductivity[15]. The band-gap of the LISICON structure has also been investigated with the GGA-PBE functional, and has been

calculated to 3.63 eV[18]. Lastly, NASICON-type materials are among the oxide electrolytes with the highest bulk ionic conductivities at around 10^{-3} S/cm due to the superionic conduction mechanism. As a result, it has relatively low migration energy barriers, being between 0.3-0.4 eV[16]. However, a big drawback of this material is that the Ti reduces from Ti^{4+} to Ti^{3+} when in contact with Li[14]. The band-gap of NASICON has been calculated with the GGA-PBE functional to be 4.34 eV[18].

$Li_{10}MP_2S_{12}$(LGPS) (M=Si,Ge,Sn) one of most promising sulfide materials for use as SSE[14][16]. The LGPS electrolytes have a higher ionic conductivity compared to the oxides, reaching values at around 10^{-2}S/cm, having migration energy barriers around 0.2-0.25eV[14][16]. The deformable nature of the structures produces a more robust material. However, the electrochemical stability window of the material is smaller, making it less stable when in contact with the electrodes[14]. The band-gap calculated with the GGA-PBE functional has been determined to be 2.21 eV. It also has the possibility of producing hazardous H_2S gas when in contact with water. Table 1 compares the values of the conductivity, average Li migration energy barrier, molar mass and PBE functional calculated band-gap between the aforementioned solid-state electrolytes.

Table 1: Comparison between the conductivity, σ, average migration energy barrier, E_m, and the band-gap calculated with the PBE functional between competing oxide and sulfide SSEs found in the literature.

Structure	σ [S/cm]	E_m [eV]	Band-gap [eV]
LLZO	10^{-3}-10^{-4} [14]	0.35-0.40[14]	4.30[17]
LLTO	10^{-3}[16]	0.30-0.40[16]	2.56[18]
LISICON	10^{-7}-10^{-3}[16]	0.40-0.60[16]	3.63 [18]
NASICON	10^{-3}[16]	0.30-0.40[16]	4.34[18]
LGPS	10^{-2}[14][16]	0.20-0.25[14][16]	2.21 [18]

2.4 Preliminary work

A preliminary first-principles study about the structures LiGeNO, LiGeNS, LiSiNO and LiSiNS was previously performed, studying the crystal structures of the materials as well as the band gap and Li-ion migration paths. Here the four structures were modelled and calculated with DFT using the Vienna Ab-inito Simulation Package(VASP). All four structures have the $Pca2_1$ space group, and each Li-ion occupy the equivalent Wyckoff-site 4a. The structures consist of a corner- and edge-sharing cation polyhedra and Li-ion polyhedra. All of the structures inhibit N_3BX tetrahedrons, where B is the cation and X is the anion. However, differences in the anion lattice and cation size result in differing Li-ion polyhedra. Here the two oxygen structures inhibit $LiNO_3$ tetrahedrons, while the LiGeNS inhibits $LiNO_4$ pentahedrons and LiSiNS $LiNS_5$ octahedrons.

The density of states for the four structures was calculated using the HSE06 functional, and a nudged elastic band(NEB) analysis was performed to calculate the migration energy barrier for the Li-ions. Each structure has three Li-ion migration paths via vacancy mechanics, corresponding in the hop of either Li_2, Li_3 or Li_4 to a vacancy at the Li_1 site. The resulting calculated band gaps are presented in table 2, together with the migration energy barrier for the three paths. The stronger electron shielding of the sulphur-ions' core contributes to a higher valence-band energy. Thus the sulphide materials have a lower band-gap compared to the oxide materials. The lower band gap of the Germanium materials is due to Ge's s-orbitals contribution to the conduction band. Whereas

for Si, only the p-orbital contributes to the conduction band. This explains why LiSiNO has the highest band gap, followed by LiGeNO and LiSiNS, while LiGeNS have the lowest. From the NEB analysis, it is clear that the most energetically preferable migration path is between L_4 and Li_1 for all four structures. Additionally, the structure with the lowest migration energy barrier is LiSiNO, which had an energy barrier of 0.171 eV for path 3. LiSiNO, LiSiNS and LiGeNS all had relatively lower energy barriers for paths 1 and 3, while LiGeNO had slightly higher energy barriers. The differences in energy barriers for each structure were largely down to the difference in Li-polyhedra, cation size and anion-lattice softness.

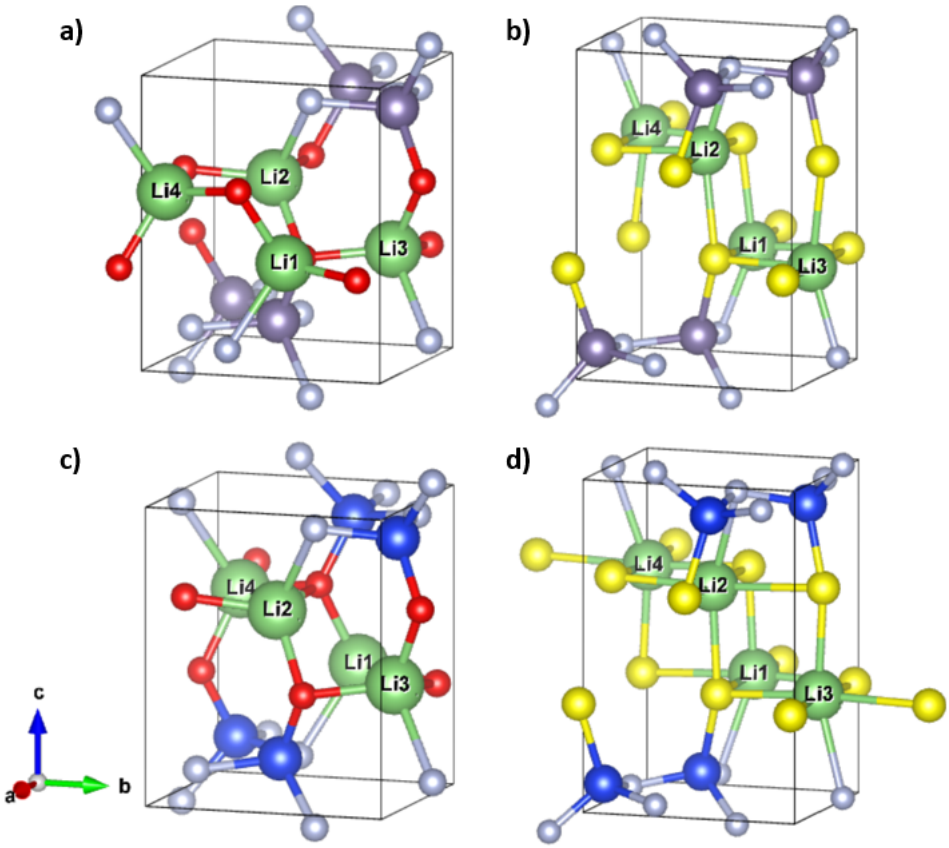

Figure 3: Illustration of the four structures LiGeNO(a), LiGeNS(b), LiSiNO(c) and LiSiNS(d). Each Li-ion is labelled to further illustrate the differing Li-ion polyhedrons.

2.5 Previous studies of LiSiNO materials

Outside of the preliminary study, a limited amount of studies have been performed on LiSiNO materials. However, two papers have been published using first-principles calculations to study the band gap, and electronic conductivity of LiSiNO[19][6]. An article by Y. Y. Ma. et al. [19] examined the electronic properties of LiSiNO for the analysis of the material as UV-based LEDs. In this paper, LiSiNO doped with Eu^{2+} and Mn^{2+} were experimentally fabricated and analysed.

Table 2: The molar mass and the band gap of the four structures calculated with the HSE06 functional, together with the migration energy barrier for each Li migration path.

	LiGeNO	LiGeNS	LiSiNO	LiSiNS
Molar mass [g/mol]	110	126	65	81
Band gap [eV]	4.979	3.778	7.166	4.954
Path 1 [eV]	0.588	0.335	0.422	0.363
Path 2 [eV]	0.690	0.690	0.587	0.759
Path 3 [eV]	0.378	0.286	0.171	0.354

First-principles calculations were used to determine the material to be an insulator with an indirect band-gap of 5.4 eV. This was further supported by experimental data obtained from diffuse reflection spectrum. The article by X. Zhang et al. examined the band gap of LiSiNO using the First-principles High throughput Screening Pipeline for non-linear optical materials(FHSP-NLO) method. This method consists of combining linear and non-linear optical property calculations and DFT calculations together with data transformation and extraction. Using an HSE functional, the band gap was accurately calculated to be 6.95 eV[6]. Outside of first-principles calculations, D. Na et al. have synthesised LiSiNO as an amorphous electrolyte, which was applied using RF sputtering in Ar/N_2 atmosphere[5]. The results showed a measured ionic conductivity of $2.47{\cdot}10^{-6}$S/cm[5].

3 Theory

3.1 Solid-solutions

Solid-solutions are a combination of two materials with the same crystallographic structure. This necessitates a continuous variation in compound stoichiometry without a change in structural type[20]. An example of this is the two perovskite crystals LaFe(III)O_3 and SrFe(IV)O_3 which can form a solid-solution where x amount of La ions are substituted with x amount of Sr ions giving the following compound, $La_{1-x}Sr_xFeO_3$[20]. The change in lattice parameters as a function of the composition can be described as a weighted mean of the two constituents' lattice parameters by Vegard's law[20],

$$a_{A_{(1-x)}B_x} = (1-x)a_A + xa_b \tag{1}$$

Depending on the substituting ions, the solid-solutions can be described by either the ideal or regular solution model[21]. The ideal solution model assumes that there is no energy change associated with rearrangements of atoms A and B. Therefore, the energies of the solid-solutions can be described as the weighted mean of the average energy of each ion at the given temperature and the amount of each ion[21],

$$E = N_A u_A + N_B u_B = E_B + E_A \tag{2}$$

Where E is the energy, N_i is the amount of ion i and u_i is the average energy of ion i. A consequence of this definition is that for an ideal solution, the enthalpy of mixing will be equal to zero. For the regular solution model, the energy of the solid-solution is determined by the pair-wise contributions between the ions[21]. Therefore the energy for a solid-solution defined by the regular solution model can be described by the energies of the individual ions and the pair-wise contributions,

$$E = E_A + E_B + N_{AB}\omega_{AB} \tag{3}$$

Where ω_{AB} is the pairwise contributions. Therefore will the enthalpy of mixing here be given by the molar interaction coefficient Ω_{AB},

$$\Delta_{mix}H_m \approx \Delta_{mix}E_m = \Omega_{AB}x_A x_B \tag{4}$$

The interaction coefficient describes the interaction between the different ions. The enthalpies of mixing can further be described as a function of the composition of the solid-solution[22],

$$\Delta_{mix}H = E(A_{1-x}B_x) - (1-x)E(A) - xE(B) \tag{5}$$

Where E($A_{1-x}B_x$) is the average energy of the solid-solution and E(i) is the energy of the pure phase i. Then the ΔG_{mix} can be calculated from equation 6,

$$\Delta_{mix}G = \Delta_{mix}H + RT[x_A ln(x_A) + x_B ln(x_B)] \tag{6}$$

Where the last contribution represents the entropy of mixing. Due to the definition of the models, the ideal solution model is more suited for two ions of similar sizes and properties, while the regular solution more accurately describes solid-solutions where the two ions differ in sizes and properties[21]. In a theoretical solid-solution with x A ions and 1-x B ions, the different ions can be distributed in numerous different ways. Each of these distinguishable distributions is called a configuration. In the regular solution model, these configurations will have different energies due to the resulting different pair-wise contributions. Therefore there will be some configurations which will be more likely to occur experimentally due to their lower energy. While in the ideal solution model, the pair-wise contributions are neglected, and the configurations are only important to the degeneracy for the single energy state[21].

3.2 Ionic conductivity in solids

Achieving solid-state electrolytes with satisfactory levels of ionic conductivity under working temperature is an extremely important factor in commercialising ASSBs. The ionic conductivity in solid-state materials can be expressed by the following equation,

$$\sigma = nq\mu \tag{7}$$

Where n is the number of charge carriers, q is the charge of the carriers, and μ is the mobility of the charge carriers[23][24]. The charge carriers in LiBs only have one positive charge, as the charger carriers are Li^+. The mobility of the charge carriers is crucial for the ionic conductivity in electrolytes. Because of the restriction of ionic movements in crystal structures compared to liquid electrolytes, the mobility is often lower for solid-state electrolytes. However, pathways for ionic propagation in crystal structures can lead to increased ionic mobility in specific directions[23][24]. These pathways work as open channels where the ions can migrate either one, two or three-dimensionally. Lastly, the charge carrier density also dramatically affects the materials' ionic conductivity. Ionic transport in solid-state electrolytes is defined by diffusion mechanisms in the microscopic sense[15]. The migration of the charge carriers can therefore be described as hops between ground-state stable sites and intermediate meta-stable sites of the anion framework[14]. The energy difference between these two states is defined as the migration energy barrier. Ions have a hopping attempt frequency, v_o, given by the lattice vibration frequency to overcome this energy barrier[15]. The ion mobility can further be defined by the migration energy barrier, giving the following equation for ionic conduction.

$$\sigma = nq\mu_0 e^{\frac{-E_m}{k_b T}} \tag{8}$$

Where E_m is the migration energy barrier, k_b is the Boltzmann constant and T is the temperature[23][24]. The migration energy barrier is dictated by the spatial availability of the path and the local ion coordination[14][15]. This results in ions jumping from a tetrahedral site to another tetrahedral site are more energetically favourable than an ion in a tetrahedral site jumping to an octahedral site. Additionally, ions passing between face-sharing polyhedrons are more energetically favoured than ions passing through edge-sharing polyhedrons due to the larger space to move through[14][15].

Vacancy, interstitial and interstitialcy mechanisms are the three different conduction mechanisms for crystalline structures[23][24]. For vacancy conduction, vacancies in the structure are vital for ionic conduction. Here the charge carrier jumps from their site to a compatible vacancy in the structure,

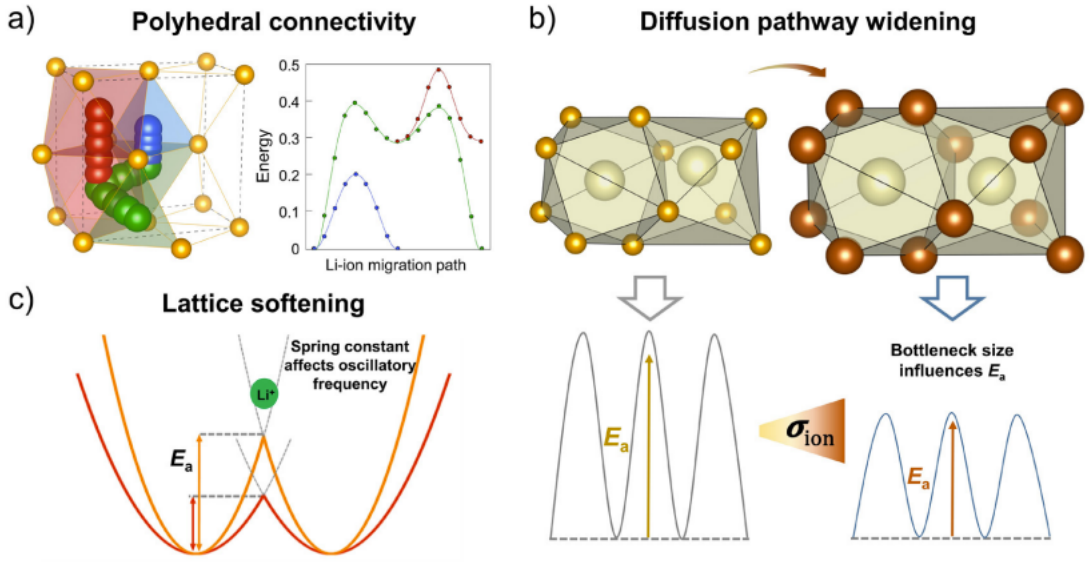

Figure 4: Illustration of the influence of polyhedral connectivity(a), diffusion pathway widening(b) and lattice softening on the migration energy barrier of a path. figure adopted from Saneyuki Ohno et. al.[14].

leaving a new vacancy in its original site. Interstitial conduction mechanisms rely on charge carriers in interstitial positions moving through the crystal structure interstitially. Lastly, the interstitialcy mechanism also relies on charge carriers in interstitial positions. However, these charge carriers migrate by pushing other charge carriers into an interstitial position and taking their original site in the crystal structure. The vacancy conduction mechanism is the most prevalent mechanism in cation conducting solid electrolytes[24]. To increase the ionic conductivity in a solid-state material, one can try increasing the structural bottlenecks' size by substituting cations with different ionic radii. Increasing the bottleneck size widens the diffusion pathways and therefore increases the charge carrier mobility. Secondly, the charge carrier density can be increased by substituting heterovalent cations and increasing the amount of empty sites[15]. Lastly, softening the anion-framework can weaken the bonding between the anions and cations, further flattening the energy landscape. However, an unfortunate consequence of this can be a lower lattice vibration and therefore lower hopping frequency for the charge carriers[15]. The effects of these mechanisms are illustrated in figure 4.

3.3 Electrochemical stability

The electrochemical stability of the electrolyte towards the electrodes is critical for the performance of the battery cell. If the electrochemical stability window of the electrode is too low, the electrolyte can start to react with the high-voltage cathode or the anode. Therefore a sizeable electrochemical stability window is vital for ensuring the inertness of the solid-state electrolyte[25]. If the electrolyte gets reduced or oxidised, the cell will produce unwanted deposition products, leading to increased electrode/electrolyte interface resistance. Achieving an SSE with high ionic conductivity and a wide electrochemical stability window is essential to commercialise all solid-state batteries. The material's

band gap characterises the electrolyte's electrochemical stability window. However, the size of the band gap alone does not fully describe the electrochemical stability window, as the band gap needs to be aligned with the electrochemical potential of the electrodes. For it not to be energetically favourable for the anode to reduce the electrolyte, the lowest unoccupied molecular orbital(LUMO) needs to be higher than the electrochemical potential of the anode, μ_a[26]. On the other side, it will not be energetically favourable for the cathode to oxidise the electrolyte if the highest occupied molecular orbital of the electrolyte is lower than the electrochemical potential of the cathode, μ_c[26]. The mechanics of the electrochemical stability window of the electrolyte in relation to the electrodes are further illustrated in figure 5[26].

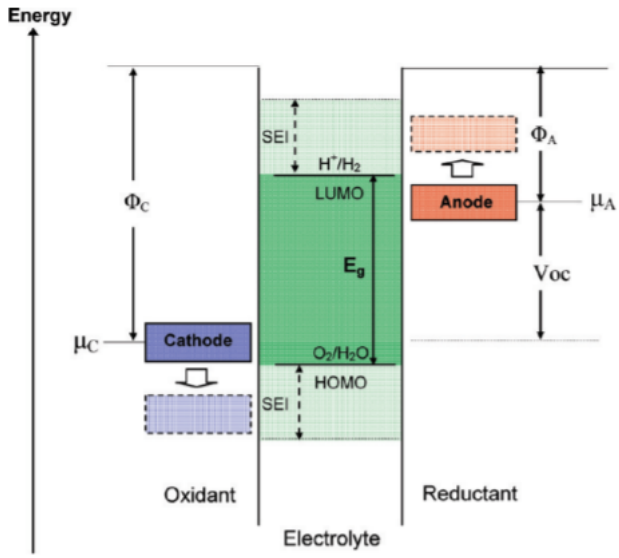

Figure 5: Illustration of the importance of the relationship between the LUMO and HOMO levels of the electrolyte and the electrochemical potential of the anode and the cathode. Figure adopted from Goodenough, J. B. and Kim, Y [26]

The maximum operating voltage of the cell is dictated by the difference in electrochemical potential for the cathode and the anode. A higher electrochemical stability window for the electrolyte would enable a higher operating voltage. However, a solid/electrolyte interface(SEI) layer can form on the electrolyte if either the HOMO or LUMO is higher or lower than the electrochemical potential for the cathode or the anode, respectively. This layer can act as a barrier for the electrolyte to keep it from reacting while still allowing charge carriers to travel through. On the other hand, a too-thick SEI layer could lead to obstruction for Li-ions to pass between the interface. Therefore the SEI layer is a very complex system that can both help stabilise the electrode/electrolyte interface and decrease the ionic conductivity. A consequence of the existence of the SEI layer is that the stability window indicated by a computed band gap can often be extended due to stabilising kinetic effects[14]. The anion framework dictates an electrolyte's oxidation stability, where a higher ionisation potential gives a higher stability[14]. The electron affinity of the non-mobile cations further dictates the reduction stability of the electrolyte[14]. The electrochemical stability window of an SSE can therefore be extended by substituting anions with higher ionisation potential or cations with better electron affinity.

3.4 Quantum Mechanics

Chemistry can be defined as knowing the energy as a function of nuclear coordinates[27]. Today's advancements in computational power enable computational models of systems that produce results that rival that of experiments[28]. To accurately simulate and model chemical structures, the chemical dynamics problems of the system need to be solved[29]. To accomplish this, we need to define the energy of the components. The Schrodinger equation can define the ground state of the system[30]. The Schrodinger equation can be solved by the Hamiltonian operator, H, and is defined as the following,

$$H\psi_n = E\psi_n \tag{9}$$

Here ψ_n is the wave function of system n, and E is the energy. The wave function describes the state of the particle, and therefore the energy is an eigenvalue of the wave function[28][31]. The energy consists of two components, the kinetic and the potential energy. The kinetic energy of the system is constant, as each particle has a particular kinetic energy, while the potential energy is unique for each type of quantum mechanical system[28]. The wave function is a function of N amount of electrons in the three spatial directions. This makes it a many-body problem which quickly becomes unsolvable computationally. Therefore the Schrodinger equation is only possible to solve exactly for a few concrete model systems. Therefore, a simplification must be made to be able to computationally accurately model any chemical system. To simplify the description of the system, the electron motion and the nuclei motion can be separated. This is called the Born-Oppenheimer approximation. As the electron travel at a much higher velocity than the nuclei, the nuclei can be assumed to be in a fixed position[28]. This gives a simpler wave function,

$$\psi_{tot} = \psi_{nuc}\psi_{el} \tag{10}$$

Where ψ_{nuc} is the wave function describing the nucleus and ψ_{el} is the wave function of the electrons. Thus the energy of the system can be described by the molecular geometry. Calculating the system's energy from different molecular geometries can derive the potential energy surface of the system[28]. This allows solving the motion of the nuclei on the potential energy surface by quantum methods. When using the Born-Oppenheimer approximation, the biggest challenge is to determine the electronic energy, as this includes both the electron-nuclei interactions and the electron-electron interactions[28][27]. The wast amount of electrons in molecular structures makes it too costly to calculate the energy exactly for each electron. Therefore atomic- and molecular orbitals have to be introduced. In these calculations, atomic orbitals are predetermined as input functions called basis sets. From here, the molecular orbitals are obtained as linear combinations of the atomic orbitals[28]. For these calculations, the electronic energy is not a result of the Schrodinger equation but rather provided explicitly as "building blocks" for the molecular orbitals[27]. Different basis sets can be chosen depending on how many additional orbitals for the atoms are wanted and the level of description of the chemical bonds. By increasing the amount of data in the basis set, the more accurate description is obtained. However, the more complex the basis set is, the higher the computational cost will be. A consequence of using such "force fields" is that the dynamics of the atoms are treated by classical mechanics[27]. Although these calculations are fast, they have some considerable downsides. Because of the dependency of force fields as input to the calculations, the force field calculations are most suited for molecular classes where a large amount of information

already exists[27]. The force field calculations also struggle to accurately include electron correlation into the molecular model.

3.5 Density Functional Theory

Density functional theory(DFT) is a method based on the electron density, rather than the wave function[30][27]. The reason for this is that wave function cannot be directly observed. What is observed is the probability of a set of N electrons in any order having the coordinates $\mathbf{r}_1$, $\mathbf{r}_2$, ...,$\mathbf{r}_N$[27]. This can further be defined in terms of the single-electron wave function

$$n(\mathbf{r}) = 2\sum_i \Psi_i^*(\mathbf{r})\Psi_i(\mathbf{r}) \tag{11}$$

This is called the electron density[30]. The calculation method is based on the Hohenberg-Kohn theorems and the Kohn-Sham equations. The Hohenberg-Kohn theorem states, "*The ground-state energy from Schrodinger's equation is a unique functional of the electron density*"[30]. The theorem means that the energy of the system can be fully described by the energy density[32][30]. The reason this is so favourable compared to the wave function is that the energy density is only dependent on the 3 spatial variables, compared to the wave function which is described by 3N variables[27]. Thus the complexity of the calculation does not scale with the size of the system for DFT calculations, while for wave function calculations, the complexity increases exponentially with the size. However, to use the electron density to calculate the energy surface accurately, the correlation between the energy and the electron density is needed.

The Kohn-Sham equations define the correlation between the energy of the system and the electron density. They establish that the energy can be determined from the interaction between a single electron and the nuclei, $\mathrm{V}(\mathbf{r})$, the Coulomb repulsion between a single electron and the electron density, $\mathrm{V}_H(\mathbf{r})$, and the exchange and correlation contributions to single electrons, $\mathrm{V}_{XC}(\mathbf{r})$[30],

$$\left[-\frac{\hbar^2}{2m}\nabla^2 + V(\mathbf{r}) + V_H(\mathbf{r}) + V_{XC}(\mathbf{r})\right]\Psi_i\mathbf{r} = \varepsilon_i\Psi_i(\mathbf{r}) \tag{12}$$

From equation 12 the exchange-correlation functional is the only potential that is not known, while the other potential can be calculated. The second Hohenberg-Kohn theorem states, "*The electron density that minimises the energy of the overall functional is the true electron density corresponding to the full solution of the Schrodinger equation*"[30]. The second theorem means that if the exchange-correlation functional were known, the electron density could be varied until the lowest energy is achieved to achieve the correct energy for the system. Additionally, it is imperative to acknowledge that the computed energy will always be higher or equal to that of the exact energy of any model system according to the variational theorem[28]. Therefore, the exchange-correlation functional must be approximated to perform DFT calculations. One approach is the generalised gradient approximation(GGA). This functional uses the local gradient in the electron density and therefore describes the spatial variation of the density. One of the most used GGA functionals is the Perdew Burke-Ernzerhof revised for solids(PBEsol) functional. This is a non-empirical GGA functional. The PBEsol functional is a good representation of the exchange-correlation potential for solid-state crystalline structures. However, GGA functionals often overestimate thermal expansion coefficients

and lattice constants and systematically underestimate band gaps. The most significant difference between the regular GGA-PBE functional and the PBEsol functional is that the regular GGA-PBE often overestimates bond lengths and cell volumes[33][34][35]. However, the difference in the calculated band gap by the two functionals is negligible[36].

Then lastly, what is needed is to solve the potential energy surface for the desired crystal structure using the Kohn-Sham equations and the exchange-correlation functional. To achieve this, an iterative algorithm is used. First, an initial electron density is chosen, which is used to calculate the single electron wave function using the Kohn-sham equation. Then using equation 11 a new electron density is calculated. Then the two electron densities are compared. If the difference is sufficiently small enough, the electron density is kept, if not then the algorithm starts over again with the new electron density. If the two electron densities compared are the same, then the ground-state electron density is achieved and can be used to calculate the total energy. In general, the relaxation of the electronic self-consistent loop will stop when the change in band-structure energy and total free energy between two steps both are smaller than the chosen global break condition. A break condition for the ionic relaxation loop can also be provided to inform the program to stop the relaxation when the norm of all the forces is smaller than the break condition.

3.6 Molecular dynamics

Molecular dynamics(MD) is a method that can accurately calculate and simulate ionic steps for materials over a relatively long time period[37]. The particle interactions can be either calculated by classical force-fields or quantum mechanics[37]. Calculations using classical force-fields enable faster but less accurate calculations, while calculations using quantum mechanics more accurately describe the system but at a higher computational cost. Ab-initio MD simulations use DFT calculations to calculate forces acting on the nuclei from the electronic structure "on-the-fly"[38]. The basic structure of MD calculations is that it starts with an initial position and velocity for all particles. Then it obtains the interatomic forces either through Ab-initio or classical calculations. Then it performs a time step which results in new positions and velocities. Then it calculates the new forces and applies another time step and so on[37]. A time step-integrator is used to calculate the new positions and velocities for each time step. The most critical factors with time step-integrators are that they are area-preservable and time-reversible[37]. This is because time step-integrators that are area-preservable and time-reversible possess a shadow hamiltonian that is exactly preserved. Consequently, the total energy of these integrators equals the shadow hamiltonian up to a certain order in Δ T[37]. This effect limits the errors so that they do not build up. This way, the total energy will always be close to absolutely conserved. Ensembles are used to ensure that the environment of the simulated system is equal to that of an experimental environment. An ensemble specifies the criteria of the experiment[37][38]. The most practical ensemble is the NVT ensemble, which states that the experiment is performed with a constant amount of material, volume and temperature[37][39]. To achieve these criteria, the NVT ensemble uses a thermostat to influence the system. The thermostat can be likened to an experiment with a system in a heat bath. Different thermostats have been developed to accurately simulate different aspects of an experimental environment. One such thermostat is the Nosé-Hoover thermostat. Here the thermostat is described by the Hamiltonian and an extended Lagrangian formulation. The extended Lagrangian formulation contains additional artificial coordinates and velocities of the particles, and an extra degree of freedom is introduced to the Hamiltonian[37][39]. This enables deterministic constant temperature MD calculations[37].

3.6.1 Machine Learning MD

Machine learning MD(ML-MD) are a method that successfully combines the accuracy of Ab-initio MD with the computational efficiency of classical force field calculations. This method uses a machine-learning algorithm to develop very accurate force fields using Ab-initio calculations, which it then uses to perform classical force field MD calculations[40][41][42]. To perform ML-MD, one first has to perform a relatively short Ab-initio run to accurately calculate the potentials of the ions. Then the program can predict initial force fields with the given structure's energy, forces, stress tensors and uncertainties. Then based on a probability model for estimation of errors, the program decides whether or not to perform additional Ab-initio calculations to update the force fields further[40][42]. A time step is then performed where the positions and velocities are calculated using either the force-fields if they are accurate enough or new Ab-initio calculations. This process is looped until the desired amount of time steps are calculated[42]. In practice, this ML-MD process means that the program initially performs MD with Ab-initio calculations while updating the force fields on-the-fly. When it becomes more "confident" with the force fields, it starts to incorporate sole force fields calculated time steps in between the Ab-initio calculated time steps. Gradually it increases the amount of force field calculated time steps until it is sufficiently confident and only performs classical force field calculations. The probability model for estimation of errors are based on bayesian error estimation[40][41][42].

4 Computational methods

4.1 Solid-solutions

Solid-solutions between LiSiNO and LiGeNO, and LiSiNO and LiSiNS were chosen to analyse possible solid-solutions between LiSiNO materials. Here three structures of both $LiSiNO_{1-x}S_x$ and $LiSi_{1-x}Ge_xNO$ with x chosen at 0.25, 0.50 and 0.75 were calculated and simulated. To create the solid-solutions, the Supercell program was utilised to produce all the possible configurations for each solid-solution[43]. First, a POSCAR of a 2 × 2 × 2 supercell of LiSiNO, with 32 Li, 32 Si, 32 N and 32 O, were chosen and then converted to a .cif file. Then all O sites and Si sites were duplicated and substituted with S and Si respectively for the $LiSiNO_{1-x}S_x$ and $LiSi_{1-x}Ge_xNO$ solid-solutions. The occupancy of the sites was then changed to match each desired solid-solution. For example, occupancy of 0.25 for all O sites and 0.75 for all S sites for the $LiSiNO_{0.25}S_{0.75}$ structure. Ten configurations were then chosen for each solid-solution from all non-symmetry equivalent configurations.

4.2 Vienna Ab-initio Simulation Package

Vienna Ab-initio Simulation Package(VASP) is a program used to perform the DFT calculations. It is a simulation program which uses DFT for atomic-scale materials modelling[44][45][46]. The program uses these five specific files to calculate the energies of the structures, POSCAR, POTCAR, INCAR, KPOINTS and job. VASP DFT calculations excel at focusing on periodically occurring arrangements of atoms, like a crystal structure. In these situations, the arrangement is a periodically occurring unit cell, described by three vectors in real space, a_1, a_2 and a_3. VASP uses k-vectors in reciprocal space to solve the integrals for the molecular models. Therefore it is necessary to specify the number of k-points in each direction in reciprocal space for VASP to calculate. The amount of k-points in each direction is often labelled as M × N × P. Using more k-points will consequently give a more accurate calculation. However, by increasing the amount of k-points the amount of computational effort also increases.

The POSCAR file describes the unit cell of the structure that VASP is supposed to simulate. It contains the position of each atom and the interatomic lengths together with the lattice vectors. The program uses border conditions, so only one unit cell is needed as input, which will be substantially repeated to obtain the desired properties. A supercell combination of several unit cells can be given as input when periodical changes in the unit cell are needed, such as vacancies or impurities. The k-point density for VASP to calculate over is given in the KPOINTS file. The POTCAR file describes the pseudo-potentials for the basis sets for each used atom. VASP receives all the input parameters for the calculations from the INCAR file. This file directly informs VASP what kind of calculations it should perform, together with calculation parameters. A detailed explanation of the different parameters in the INCAR file is given in the INCAR section of the *VASPwiki*. Lastly, the job file gives a simple description of the job to VASP. It contains the name of the job, account name, max computing time and the number of nodes to calculate over.

4.3 Structure analysis

The ten configurations of each solid-solution were then geometry-optimised by performing ionic relaxation calculations with increasing ionic steps until the break conditions were reached. For each calculation, the POSCAR was replaced by the updated CONTCAR from the previous calculation. The ionic relaxation was calculated with a quasi-Newton algorithm with the PBEsol functional. For each successful calculation, the max ionic step was increased by ten until the structures were fully relaxed. When all configurations were geometry-optimised, the configuration with the lowest total energy per atom for each solid-solution was chosen for further analysis. The enthalpy and Gibbs free energy for the solid-solution systems were calculated by all the configurations using the SOD module[47].

The density of states for each solid-solution were calculated using the PBEsol functional to achieve an estimation of the electrochemical stability of the materials. Further were the band structure calculated using the PBEsol functional to observe the trends in the band gap for the solid-solution systems.

4.4 Nudged elastic Band

Nudged Elastic Band is a method used to analyse the energy landscape of manually chosen migration paths in a crystal structure. This method introduces a vacancy to the unit cell to investigate the vacancy migration mechanics. Then a start- and endpoint of an ion migrating to the vacancy is chosen. The possible ion-migration paths to be analysed then must be manually chosen. The saddle points and minimum energy paths between the start and -endpoint for each path are then determined by energy optimising a number of "images" of the unit cell along the path. These images are optimised by relaxing to the lowest possible energy while keeping equal spacing to neighbouring images. Spring forces along the band between each image are introduced to be able to achieve this optimisation. For the climbing-NEB method, the saddle point can be more accurately determined by driving the highest energy image towards the saddle point. Unlike the other images, this image does not feel the spring forces along the band. Instead, it maximises the energy along the band and minimises it in all other directions. This results in the image being located directly at the saddle point. A consequence is that the spacing between the saddle point image and the two other neighbouring images will not have the same distance.

The start- and endpoint for the possible Li migration paths to an inserted vacancy were determined using pymatgen.analysis.diffusion.neb module. The POSCAR for each start- and endpoint of all the paths were then geometry optimised before five intermediate images between each start- and endpoint was extrapolated using pymatgen.analysis-.path_finder[48]. The resulting POSCAR images were then relaxed to the lowest possible energy while still maintaining equal spacing to the neighbouring images.

4.5 Molecular dynamics

A short-term and a long-term machine learning Molecular-Dynamics analysis was performed on each solid-solution and pure structure to analyse the Li-mobility of the structures. The NVT thermostat were used in each simulation to closely simulate an experimental environment.

For the short-term analysis, 100 ps were simulated for each structure with temperatures at 500 K, 600 K, 700 K, 800 K, 900 K and 1000 K. For each of the temperature simulations, a warm-up simulation was first performed with a start temperature set to 0 K and an end temperature set to the simulation temperature. Here 2000 steps were calculated with a time-step of 2 fs. Then an equilibrium run was simulated with constant temperature over the same time frame. After the equilibrium simulation, the final production run for 100 ps was simulated by calculating 50,000 steps with a time-step set to 2 fs. New force-fields were developed for each run. Gamma-point 1x1x1 k-points were chosen for each structure. Examples of the INCAR used for the warm-up, equilibrium and production simulations are presented in Appendix **??**, E.7 and E.8. The Li-trajectories were analysed using Kinisi[49][50].

For the long-term simulations, 10 ns of each structure were simulated at 800 K. Here, the developed force-fields from the short-term simulations were used as a starting point. To simulate 10 ns, 2,000,000 steps were calculated with a time-step of 5 fs. The chosen force-field was continuously developed. The same k-pints were used as in the short-term simulations. An example of an INCAR used for the long-term MD simulations is presented in Appendix E.9.

4.6 Visualisation

VESTA was used to visualise the solid-solutions crystal structures and obtain relevant unit parameters, bond lengths and volume[51]. Further, were Sumo used to plot the calculated density of states of the materials[52]. Finally, were all energy calculations related to the structural data, cell parameters, band gap and molecular dynamics data plotted using Matplotlib[53]. To better describe the settings and parameters used in each VASP calculation, the INCAR used for each section is presented in Appendix E.

5 Results

5.1 Structural data

The total amount of configurations (N), non symmetry-equivalent configurations (M) and configurations selected (S) for the analysis for the substitution of N_s amount of the 32 available Si or O ions in the 2x2x2 128 ion LiSiNO supercell are presented in Table 3. To analyse the stability of the solid-solution systems, the Gibbs free energy of mixing and enthalpy of mixing were calculated from the total energy and cell parameter from all ten configurations of each solid-solution. The total energy per atom of the configurations is presented in Appendix A. The enthalpy- and Gibbs free energy of mixing is presented in Figures 6 and 7. Both systems have an approximately equal positive enthalpy- and Gibbs free energy of mixing, indicating an exothermic mixing process. For the $LiSi_{1-x}Ge_xNO$ system, the two mixing energies increase towards a peak at $LiSi_{0.25}Ge_{0.75}NO$, while the $LiSiNO_{1-x}S_x$ system immediately peaks with $LiSiNO_{0.75}S_{0.25}$. For both systems, the Gibbs free energy of mixing decreases with increasing temperature.

Table 3: The total number of configurations(N) for the LiSiGeNO and LiSiNOS systems with N_s substitutions, the number of inequivalent configurations(M) and the number of configuration selected for analysis(S).

N_s	X	N	M	S
0	0	1	1	1
8	0.25	10,518,300	329,116	10
16	0.50	601,080,390	18,786,630	10
24	0.75	10,518,300	329,116	10
32	1	1	1	1

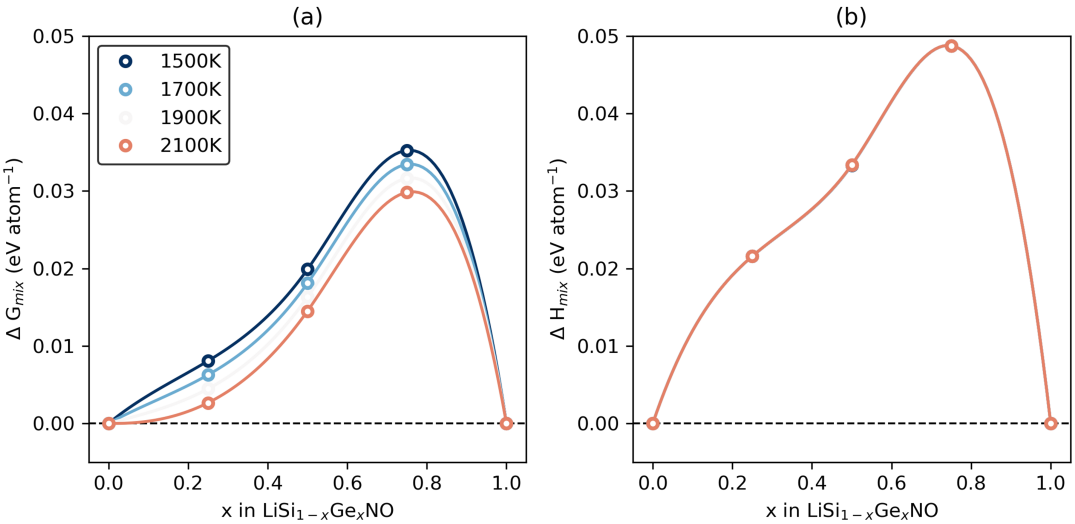

Figure 6: The enthalpy(b) of mixing and the Gibbs free energy of mixing with increasing temperature of the $LiSi_{1-x}Ge_xNO$ solid-solution systems plotted against concentration of substituent.

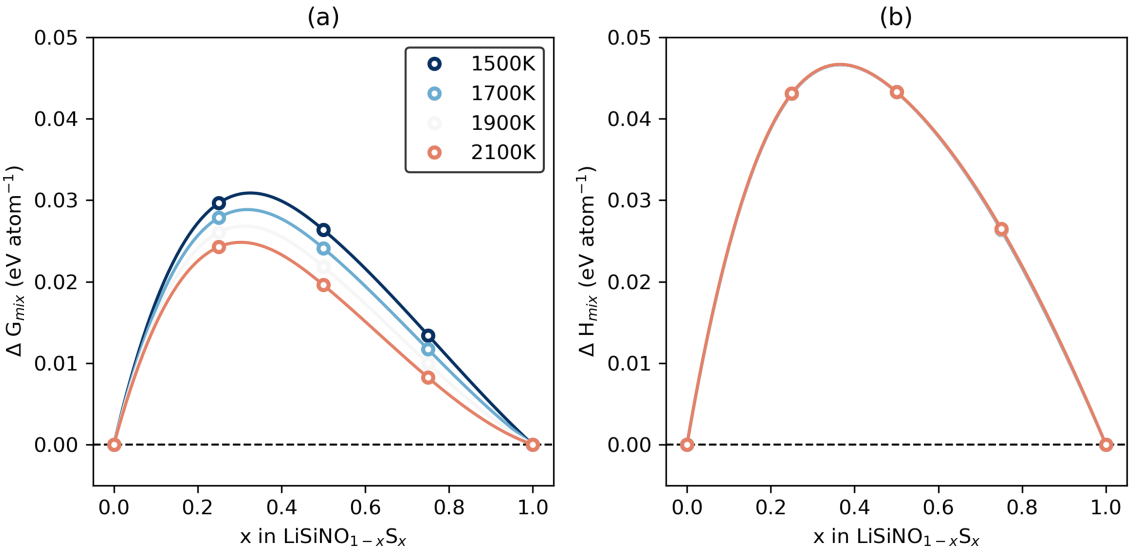

Figure 7: The enthalpy(b) of mixing and the Gibbs free energy of mixing with increasing temperature of the $LiSiNO_{1-x}S_x$ solid-solution systems plotted against concentration of substituent.

Figure 8 presents the geometry optimised supercells of the solid solutions. Each structure was visualised using the 3D visualisation program VESTA[51], and a legend of the ions involved are presented on the figure's left. The figure illustrates the crystal structure of each solid-solution and further shows the ordering of the substituted ions.

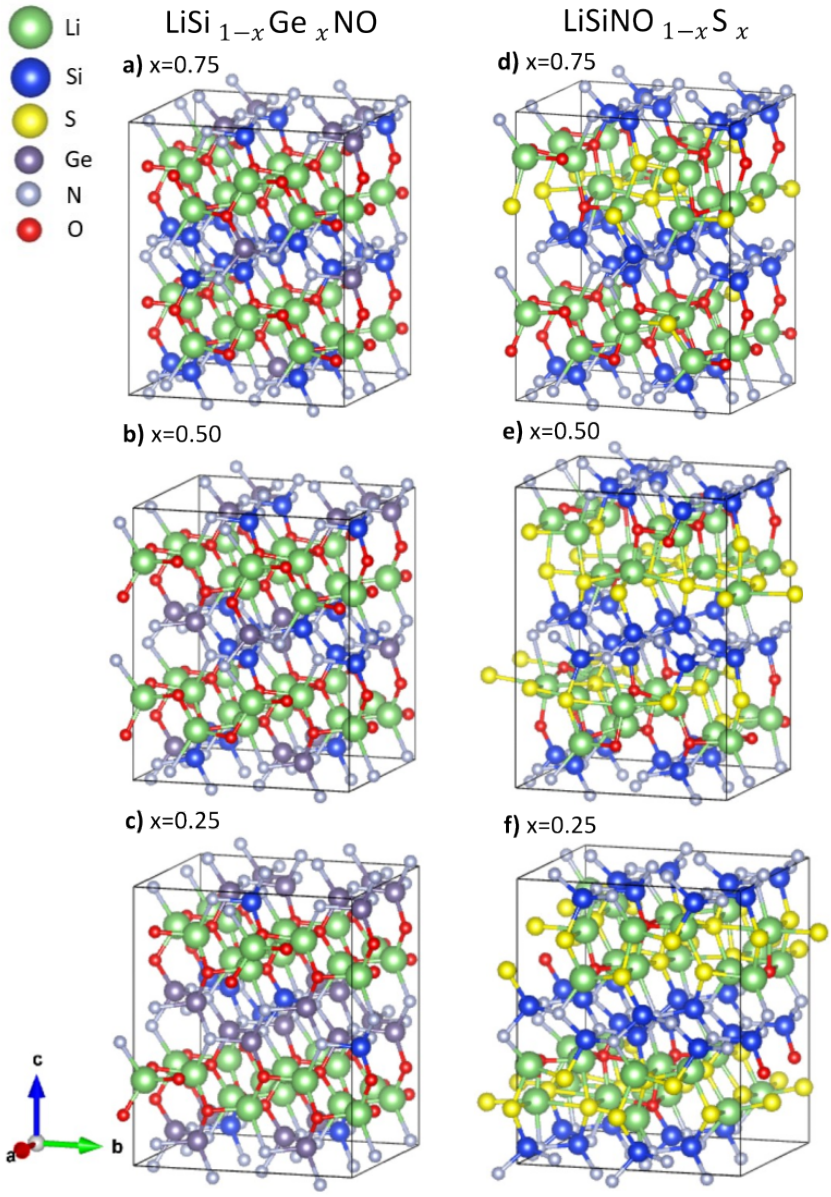

Figure 8: Illustration of the supercell of each solid-solution, showing the change in order with substituent concentration. A legend for the different ions is presented on the left.

The unit volume, unit parameters and average Li-Li distances of the LiSiGeNO and LiSiNOS solid-solution systems are presented in Tables 4 and 5, together with the average Li-S and Li-O distances and the average N-Si and N-Ge distances for the LiSiNOS and LiSiGeNO solid-solutions respectively. The parameters are taken from the configurations with the lowest total energy per atom. The table illustrates the trend of increasing volume and ion distances with increased concentration of substituent. The exceptions from this trend are the $LiSiNO_{0.25}S_{0.75}$ and $LiSi_{0.25}Ge_{0.75}NO$ solid-solutions, which both exhibit volume on par with LiSiNO. Further does $LiSiNO_{0.25}S_{0.75}$'s average Li-Li distances lay between the values for $LiSiNO_{0.75}S_{0.25}$ and $LiSiNO_{0.50}S_{0.50}$, the average Li-Li distances for $LiSi_{0.25}Ge_{0.75}NO$ however are lower than LiSiNO. For $LiSiNO_{0.25}S_{0.75}$ the average Li-O distances are similar to that of LiSiNO, while it also has the shortest average Li-S distances. The same trends occur for the N-Si and N-Ge distances for the LiSiGeNO structures. Here the average N-Si and N-Ge distances steadily increase until $LiSi_{0.25}Ge_{0.75}NO$, which has the lowest average distance. To further illustrate the change in lattice parameter for the six chosen configurations, each lattice parameter has been plotted against the composition in Figure 9. It is evident from the figure that both solid-solution configurations with 75% substituent break from linearity in increasing lattice parameters following Vegard's law.

Table 4: Presentation of the volume and unit parameters for the $LiSiNO_{1-x}S_x$ solid-solution system, as well as the change in the average Li-Li, Li-O and Li-S distances with substituent.

Unit	x=0	x=0.25	x=0.50	x=0.75	x=1
Volume [Å^3]	1256	1384	1510	1260	1730
a	9.450	9.579	9.642	9.500	9.809
b	10.391	10.566	10.684	10.399	10.797
c	12.728	13.674	14.657	12.756	16.338
Av. Li-Li [Å]	2.930	3.030	3.234	3.176	3.609
Av. Li-S [Å]	-	2.460	2.535	2.282	2.574
Av. Li-O [Å]	1.943	2.105	2.142	1.999	-

Table 5: Presentation of the volume and unit parameters for the $LiSi_{1-x}Ge_xNO$ solid-solution system, as well as the change in the average Li-Li, N-Si and N-Ge distances with substituent.

Unit	x=0	x=0.25	x=0.50	x=0.75	1
Volume [Å^2]	1256	1301	1341	1260	1416
a	9.450	9.645	9.782	9.500	10.043
b	10.391	10.520	10.643	10.399	10.870
c	12.728	12.827	12.882	12.756	12.972
Av. Li-Li [Å]	2.930	2.954	2.979	2.915	3.048
Av. N-Si	1.756	1.761	1.764	1.745	-
Av. N-Ge	-	1.872	1.878	1.858	1.888

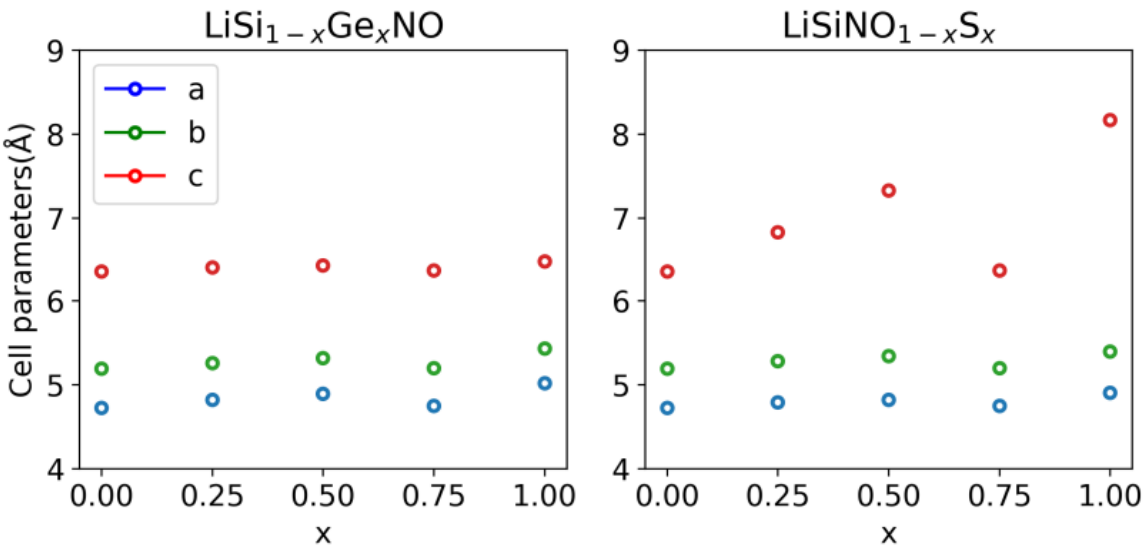

Figure 9: Lattice parameters a, b and c for the $LiSiNO_{1-x}S_x$ and $LiSi_{1-x}Ge_xNO$ solid-solution systems plotted against concentration of substituent.

5.2 Band Gap and Electrochemical Stability prediction

Using the PBEsol functional, the DOS and band-gap of the structures have been calculated to study the electrochemical stability of the materials. The density of states plot for the six solid-solutions is presented in Figure 10. The plotted Density of States illustrates how the change of ions and introductions of orbitals affects the electronic structure of the solid-solutions. The density of states plot shows a lowering of the band gap with increasing Ge and S substitution, as Ge s-orbitals and S p-orbitals contribute to a lowering of the conduction band and raising of the valence band, respectively.

The calculated band-gaps from the geometry optimised solid-solutions and pure structures are shown in Table 6, and are plotted against composition in Figure 11. The results show how the band-gap of the materials decrease with increasing S and Ge substitution. It is also evident that the $LiSi_{1-x}Ge_xNO$ solid solutions experience a linear decrease in band-gap from LiSiNO to LiGeNO. However, $LiSiNO_{1-x}S_x$ show an especially immediate drop in band-gap from LiSiNO to $LiSiNO_{0.75}S_{0.25}$ before linearly decreasing towards LiSiNS. The complete density of state plots for the solid-solutions are provided in Appendix B.

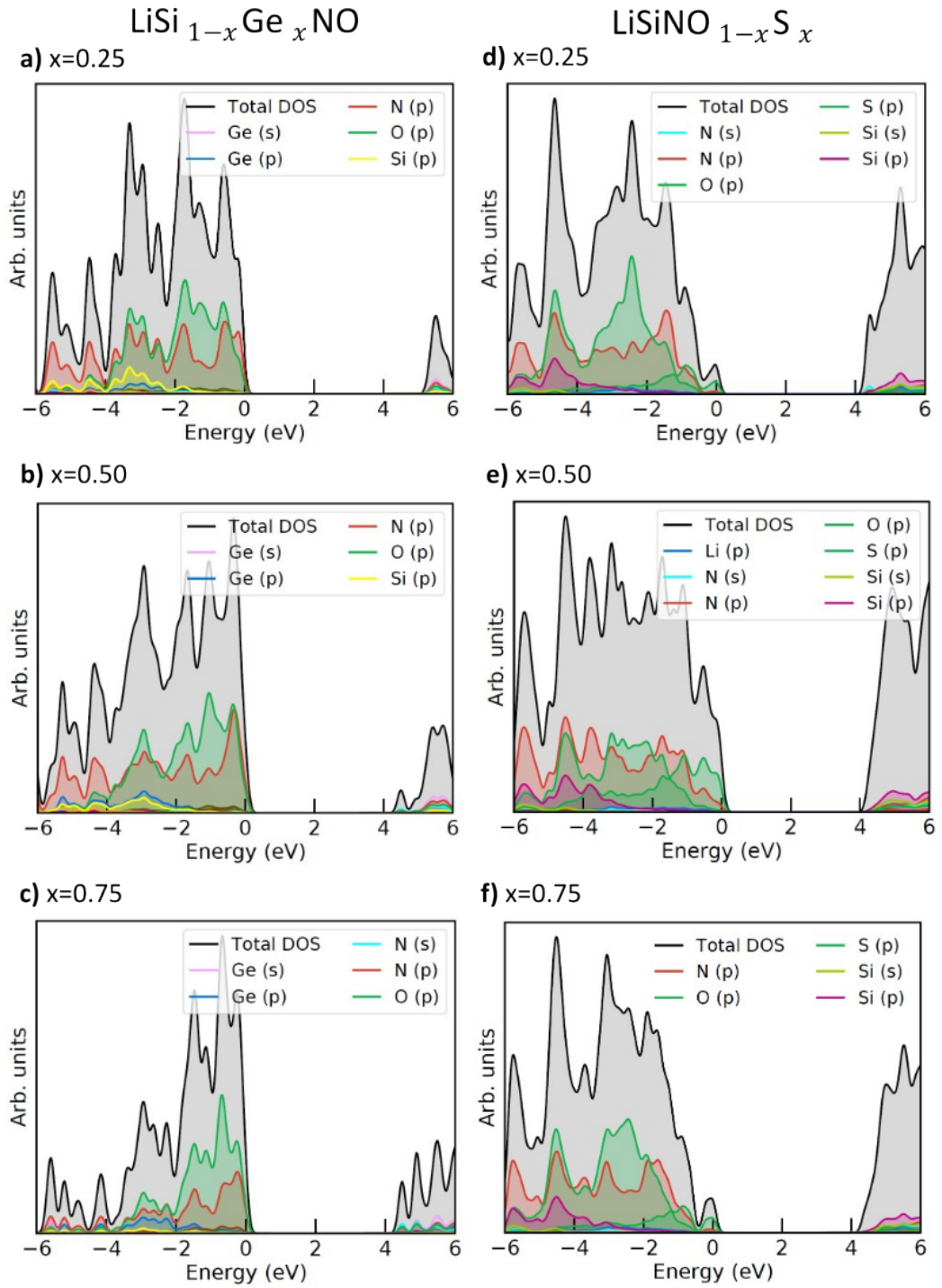

Figure 10: The density of states plotted for the six solid-solutions, with the valence-band maximum centred at zero eV.

Table 6: The band-gap of each of the analysed structures in the $LiSi_{1-x}Ge_xNO$ solid-solution system.

	x=0	x=0.25	x=0.50	x=0.75	x=1
band-gap [eV]	5.37	4.43	4.01	3.57	3.19

Table 7: The band-gap of each structures analysed in the $LiSiNO_{1-x}S_x$ solid-solution system.

	x=0	x=0.25	x=0.50	x=0.75	x=1
band-gap [eV]	5.37	4.05	3.97	3.75	3.71

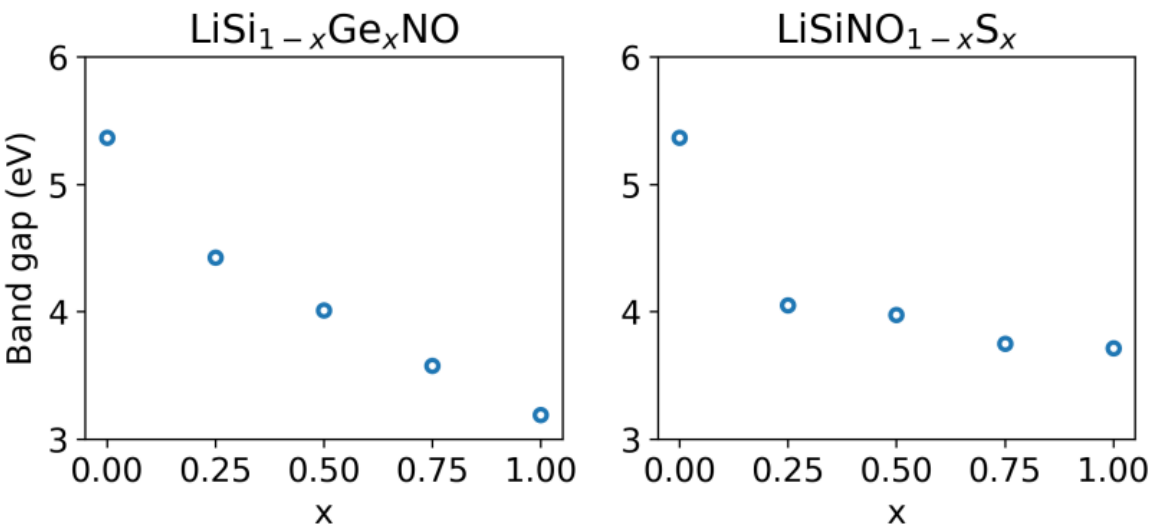

Figure 11: The band-gap of each solid-solution plotted against the concentration of the substituent.

5.3 Kinetics

5.3.1 Short term Li trajectories

Machine learning molecular dynamics was used to simulate 100 ps of all nine structures. The bayesian error was plotted to determine the accuracy of each structure's ab-initio calculated force fields. The complete bayesian error plot for each structure is presented in Appendix C. An example of the bayesian errors for $LiSiNO_{0.50}S_{0.50}$ are given in Figure 12. The initial spike and ensuing decrease in the bayesian error during the first 10,000 steps for all the ML-MD calculations suggest that the initial force fields were inaccurate predictions. However, the stabilisation in error after the first 10,000 steps suggests that the machine learned force fields from the first 10,000 steps are good estimates for the ab-initio reference result. A slight broad peak can be observed between the 45,000- and 50,000th steps. Therefore the Li-ion MSD were calculated between 20-80 ps for all the simulations.

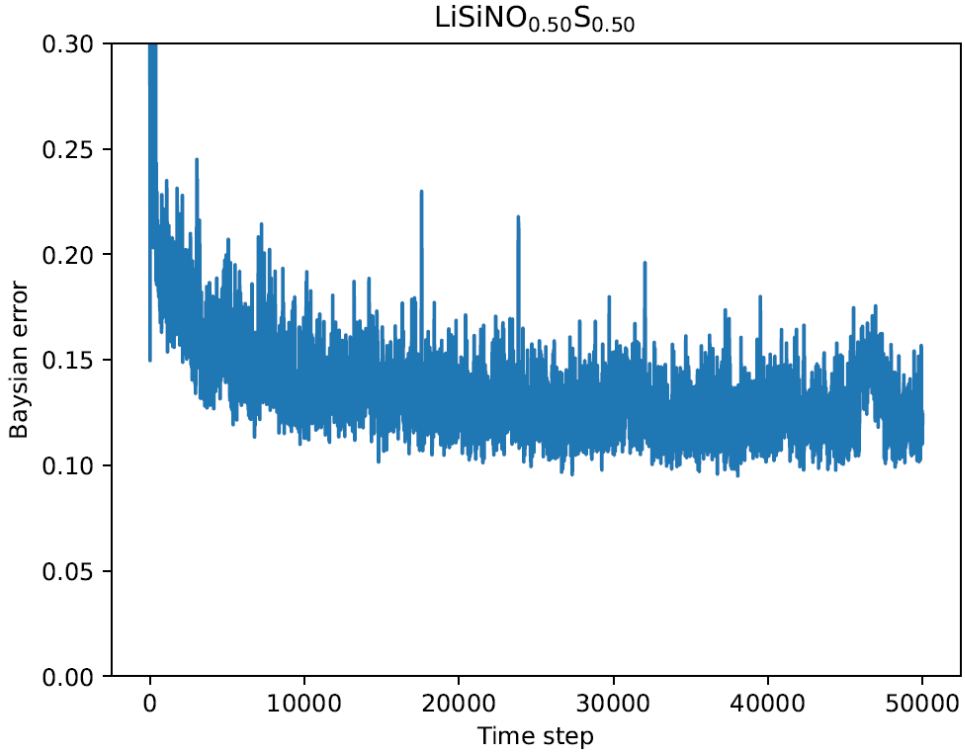

Figure 12: The plotted bayesian error for the 100 ps ML-MD simulation of $LiSiNO_{0.50}S_{0.50}$

The mean square displacements of the 32 Li-ions in each solid-solution structure were calculated from the 100 ps ML-MD simulations at 800K. Figure 13 presents the Li-ion MSD for the 60 ps between 20- and 80 ps from the simulations where the bayesian error was deemed satisfactory. Here the LiSiGeNO structures are presented in Figure 13 a) and the LiSiNOS structures are presented in Figure 13 b). In the figures, the Li-MSD is plotted against the simulated time. The MSD illustrates the deviation of the Li-ion from its site position. It can therefore be used to compare Li's potential

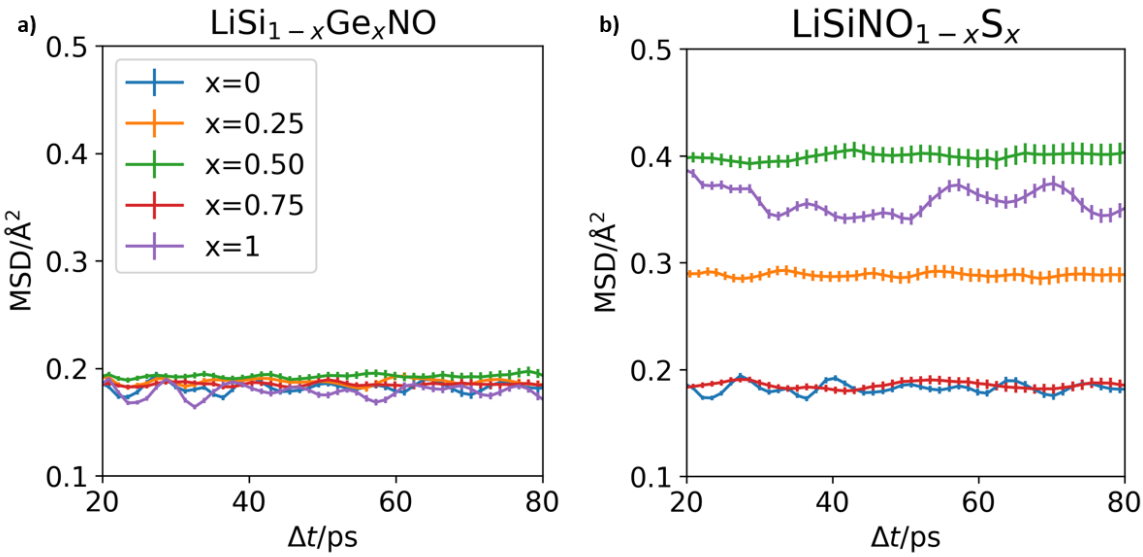

Figure 13: The plotted Li-ion MSD for the LiSiGeNO and LiSiNOS structures against the simulated time.

local mobility between solid-solution and pure structures. From Figure 13 it is clear that the MSD varies much greater with S substitution than for Ge substitution. In Figure 13 b) the MSD increases from the initial value of LiSiNO to $LiSiNO_{0.75}S_{0.25}$ and then peaks with $LiSiNO_{0.50}S_{0.50}$. However, the MSD value then drops down to the LiSiNO level for the $LiSiNO_{0.25}S_{0.75}$ solid-solution and then LiSiNS measure a second highest MSD value between $LiSiNO_{0.75}S_{0.25}$ and $LiSiNO_{0.50}S_{0.50}$. Figure 13 a) shows the much lower variance in MSD between the LiSiGeNO solid-solutions. However, some of the trends from the LiSiNOS solid-solutions reoccur, such as the $LiSi_{0.50}Ge_{0.50}NO$ solid-solution having the highest MSD values while LiSiNO being towards the bottom. Here the values of LiGeNO are on par with LiSiNO, while $LiSi_{0.25}Ge_{0.75}$ has values close to $LiSi_{0.75}Ge_{0.25}$.

5.3.2 Long term diffusion

Lastly, a long-term diffusion analysis was performed by executing ML-MD simulations of 10 ns for all the solid-solutions and the three pristine structures. The long-term simulations' goal was to achieve diffusion regimes where estimations of diffusion coefficients and migration energy barriers could be gathered to gain insight into the Li-ion migration in the materials. The bootstrapped mean square displacements of the Li ions for all the simulations are plotted against the simulated time for the LiSiNOS and LiSiGeNO systems in Figure 14. The individual plots of the calculated MSD for the complete simulation of each structure is presented in Appendix D. The simulation of $LiSi_{0.25}Ge_{0.75}NO$ were unsuccessful as it showed the unit cell to be indefinitely expanding. Additionally, were the $LiSiNO_{0.50}S_{0.50}$, $LiSiNO_{0.25}S_{0.75}$ and LiGeNO simulations cut short as they experienced corruption of data.

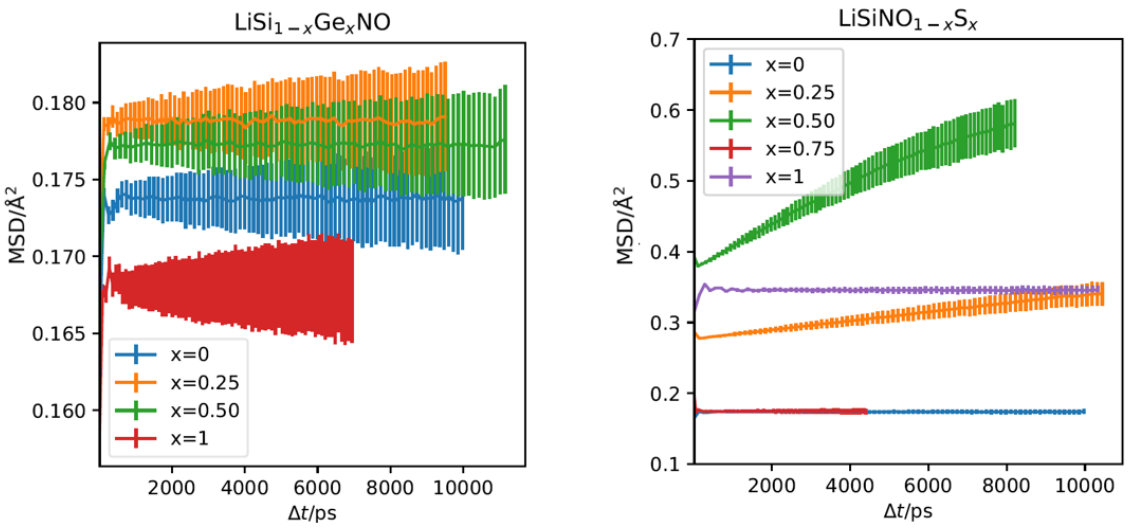

Figure 14: The plotted Li-ion MSD from the 10 ns long term ML-MD simulations for the LiSiGeNO and LiSiNOS structures against the simulated time.

It is clear that the trends in MSD follow the results from the short-term MD simulations of 100 ps. Where the LiSiGeNO structures experience little change with Ge concentration, while the LiSiNOS structures linearly increase towards a peak at $LiSiNO_{0.50}S_{0.50}$, before decreasing at $LiSiNO_{0.25}S_{0.75}$ and then again increasing at LiSiNS.

5.4 Li-ion Mobility

Three Li migration paths to the randomly inserted Li vacancy were found during the nudged elastic band analyses of $LiSiNO_{0.75}S_{0.25}$. Each path corresponded to the migration of the three remaining Li-ions in the unit cell from Figure 3. Path one was the migration of Li_2 to a vacancy in the Li_1 site, path two the migration of Li_3 and path four the migration of Li_4. An illustration of the three Li migration paths is provided in Figure 15 to present a better understanding of each path. Further, are he migration energy of each path plotted against the migration distance in Figure 16 and the energy barriers and path distances are presented in Table 8.

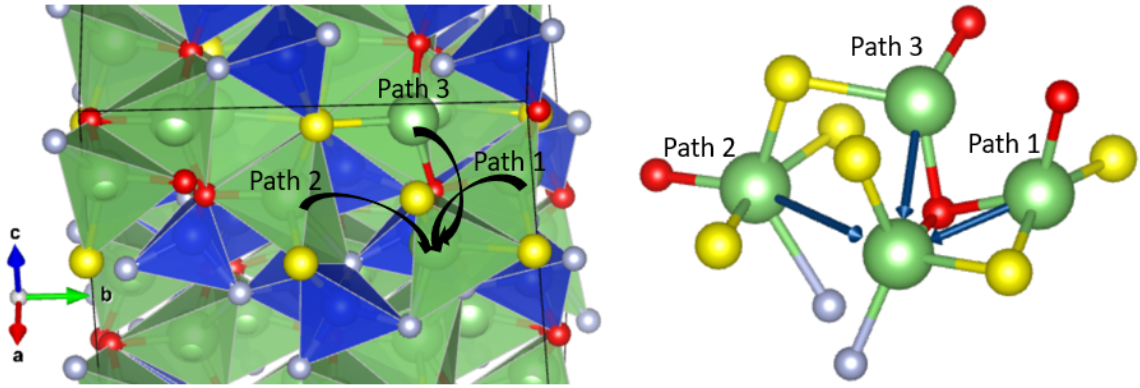

Figure 15: Illustration of Li migration path one, two and three found in $LiSiNO_{0.75}S_{0.25}$.

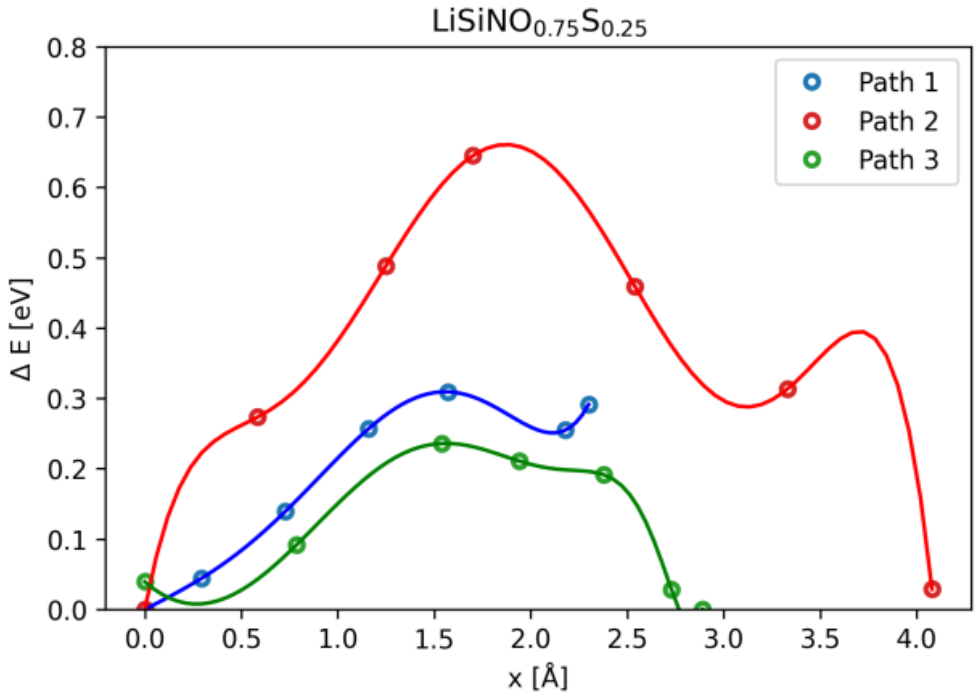

Figure 16: The migration energy for the three Li migration paths in $LiSiNO_{0.75}S_{0.25}$ plotted against the migration distance.

Table 8: The Migration energy barrier and migration distances for the the three Li-ion migration paths investigated.

	$E_a[eV]$	Distance [Å]
Path 1	0.31	2.30
Path 2	0.65	4.08
Path 3	0.24	2.89

6 Discussion

6.1 Structural analysis

6.1.1 Configurational stability

An essential factor in analysing the solid-solutions is to investigate their apparent stability. To draw accurate conclusions about the systems, we have to be certain that the configurations being investigated are stable representations of any experimental structures. Due to the solid-solutions vast amount of possible atomic configurations, only a minimal sample size of the possible configurations was analysed. Therefore it is important to realise that the results of the chosen configurations might not entirely reflect the actual reality of any experimental configurations. However, it is still possible to study potential trends between the chosen configurations and solid-solutions to gain a picture of the larger reality. When analysing the enthalpy of mixing and the Gibbs free energy of mixing, it is evident that the Gibbs free energy is quite similar to the enthalpy for both solid-solution systems. The similarity shows that the systems' entropy of mixing is relatively small. The positive deviation of mixing enthalpy and Gibbs free energy of mixing from ideality for both solid-solution systems shows that mixing to solid-solutions is an endothermic process. However, as the energies are relatively low, the materials should still be accessible to produce. While the mixing energies of $LiSi_{1-x}Ge_xNO$ peaks at 75% substitution, does the $LiSiNO_{1-x}S_x$ solid-solutions peak at 25%. These peaks indicate that the $LiSi_{0.25}Ge_{0.75}NO$ and the $LiSiNO_{0.75}S_{0.25}$ will be slightly less stable phases.

However, it is quite hard to judge the stability of the solid-solution systems based only on the few data points of the mixing enthalpy and Gibbs free energy of mixing that were calculated. To aid the stability analysis of the six specific solid-solution configurations chosen, the configurations' behaviour against Vegard's law was investigated. Vegard's law describes the expected linear relationship between the unit cell parameters and the composition of a solid-solution system. It is clear from figure 9 that for both systems, the 25% and 50% solid-solutions follow this linear relationship. However, both the 75% solid-solution configurations negatively deviate from the relationship. These results indicate the four 25% and 50% solid-solutions configurations to be more stable, while the stability of 75% solid-solution configurations could be lower. The $LiSi_{0.25}Ge_{0.75}NO$ configuration experience a relatively little, but still noticeable, decrease in the three unit parameters. However, the $LiSiNO_{0.25}S_{0.75}$ configuration experiences a similar deviation in the a and b unit parameters but a major decrease in the c parameter. Therefore it seems likely that the $LiSiNO_{0.25}S_{0.75}$ configuration is slightly more unstable compared to the $LiSi_{0.25}Ge_{0.75}NO$ configuration.

All ten different configurations of $LiSiNO_{0.25}S_{0.75}$, except configuration 8, had a volume around 1200 $Å^3$, while configuration 8 had a volume of 1652 $Å^3$. This configuration of the solid-solution more closely followed the linearity of Vegard's law. This irregularity would explain the suggested higher instability of the $LiSiNO_{0.25}S_{0.75}$ solid-solution not being shown in the enthalpy of mixing plot. The configurations with the lower volume had a more unordered anion structure, while configuration 8 had an anion structure that more closely resembled that of LiSiNS. Again due to the small sample size of studied configurations, this might not mean that all configurations of $LiSiNO_{0.25}S_{0.75}$ are unstable, but more that the result of the studied configurations might not accurately reflect that of a possible stable experimental configuration. An unstable anion-lattice can possibly explain this instability. The introduction of sulfide to the oxide anion-lattice contributes to a softening of the anion-lattice. Therefore an anion-lattice of 75% S and 25% O might not be compatible due to the

introduction of the smaller and more electronegative oxygen ions into the ordered S anion lattice of LiSiNS.

This difference in the unit cell between the configurations is not observed for the $LiSi_{0.25}Ge_{0.75}NO$ solid-solution. However, this does not rule out the possibility of configurations which more closely exhibit a linear relationship between unit parameters and composition. The instability of the $LiSi_{0.25}Ge_{0.75}NO$ configurations could be related to the increased concentration of the larger Ge ions making it more difficult for the smaller Si ions to fit into their site in the lattice.

6.1.2 Geometry optimisation

Similar trends in the unit parameters can be observed for both the LiSiNOS and LiSiGeNO solid-solutions. Firstly, the unit volume increases from 0%, 25% and 50% substituent. The increase can be explained by the larger size of the Ge and S ions compared to O and Si. Additionally, for the LiSiNOS structures, does the introduction of S into the anion-lattice result in weaker Li-S bonds compared to the Li-O bonds, and thus the unit cell experiences an expansion. For the LiSiGeNO structures, the introduction of Ge gives rise to the longer Ge-N bonds compared to the shorter Si-N bonds. Again this increase in bond lengths contributes to a large unit cell. The bond length development is due to the lower electronegativity of S and Ge compared to O and Si. The change to lower bond strength between anions and Li-ions in the LiSiNOS solid-solutions can result in higher Li mobility and therefore higher Li-ion conductivity. However, again the weaker sulfide bonds might indicate lower chemical stability for the sulfide structures.

The geometry optimised $LiSiNO_{0.25}S_{0.75}$ and $LiSi_{0.25}Ge_{0.75}$ structures both had a volume of 1260 $Å^3$ with identical unit parameters. The fact that both solid-solutions drop significantly in volume from the two 50% solid-solutions to identical unit size might suggest that the substitution of 75% of a larger ion to the LiSiNO structure results in an unstable structure. The two end-structures, LiSiNS and LiGeNO, both follow the initial trend of increased unit size. When comparing the LiSiNOS and LiSiGeNO solid-solutions it is clear that the LiSiNOS structures experience a much more significant unit cell increase than the LiSiGeNO structures. This difference can be explained by the S^{2-} relatively larger ionic radii compared to Ge^{4+}, and the change in anion-lattice further contributes to an increased unit cell. The unit cells' increased size might lead to larger bottlenecks in Li-migration paths. Especially the LiSiNOS solid-solutions' even larger unit cells can benefit from larger bottlenecks. However, a too-large unit cell might lead to extensive Li-Li distances, further inhibiting Li migration.

When comparing the average Li-Li distances for the solid-solutions in Tables 4 and 5, the same trends as for the unit cells reoccur. Again the Li-Li distances increase until the 75% substituent solid-solutions, where the distances drop drastically. However, for the Li-Li distances, the two solid-solutions are not identical. The $LiSiNO_{0.25}S_{0.75}$ have a longer average distance at 3.176Å, while $LiSi_{0.25}Ge_{0.75}NO$ has an average Li-Li distance at 2.979Å. The shorter average Li-Li distances for $LiSi_{0.25}Ge_{0.75}NO$ might be due to the arrangement of the Li-ions. In the LiSiGeNO structures, the Li-ions are more arranged in clusters creating $LiNO_3$ tetrahedra. However, due to the softening of the anion lattice with substituting S-ions, the Li-ions start to drift away from these clusters, creating higher average Li-Li distances. For the LiSiNOS solid-solutions one can also analyse the change in Li-anion distances with increased S concentration. Here it is evident that the average Li-O and Li-S distances increase slightly.

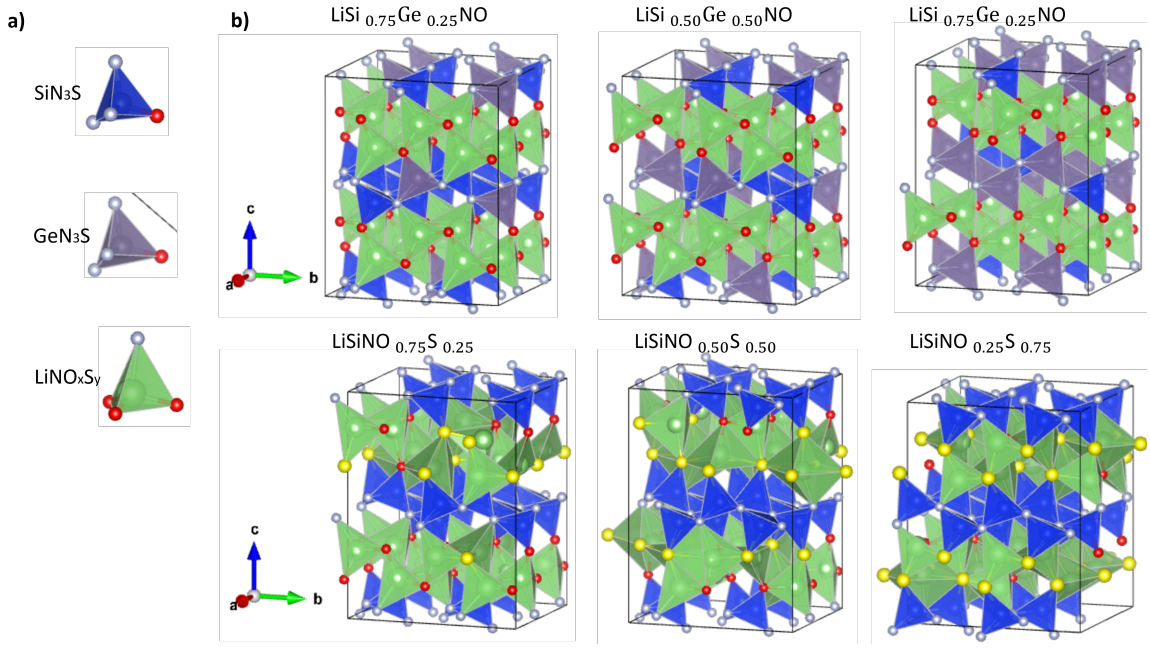

Figure 17: Figure 17 b) illustrates the polyhedra and their connectivity of the six solid-solutions. Each polyhedra are presented in the legend in figure 17 a).

Analysing the LiSiNOS solid-solution structures reveals a change in Li-position and $LiNA_x$ polyhedra with increasing S concentration. For the LiSiGeNO structures, increased Ge concentration only increases the average Li-Li distances while not changing the original $LiNO_3$ tetrahedra. For the LiSiNOS solid-solutions, the change in Li-ion positioning changes the $LiNA_x$ polyhedra and increases the coordination number of Li. It is evident that an increased S concentration leads to an increased amount of distorted $LiNOS_3$ tetrahedra and $LiNS_5$ octahedra. Figure 18 shows examples of the different polyhedra that exists in $LiSiNO_{0.75}S_{0.25}$, $LiSiNO_{0.50}S_{0.50}$ and $LiSiNO_{0.25}S_{0.75}$. This change in polyhedra is due to the resulting softening in the anion lattice, which increased S concentration brings. The softer anion lattice leads to the aforementioned drifting of the Li-ions away from the clusters. As a result, the average Li-anion coordination seems to increase with S concentration, enabling the formation of these distorted $LiNOS_3$ tetrahedra and $LiNS_5$ octahedra. Due to the geometry and increased size of the distorted tetrahedra and octahedral, these new polyhedral have edge-sharing properties. A consequence of the distorted tetrahedra and octahedra can be wider and more easily penetrable bottlenecks for Li-ions to migrate through. The existence of different polyhedra and their edge-sharing geometry might also improve Li migration due to the polyhedral connectivity enabling different and more accessible paths for the Li ions to migrate through.

All the solid-solutions retain the pure structures' 2D layered pathways formed by the Li-polyhedra. The 2D pathways can be seen in figure 17. Here the green Li-polyhedra form a pathway for enhanced Li-ion transport in the (a,b)-plane due to unhindered connectivity between Li-polyhedra. The 2D Li pathways enhance the ionic conductivity in the electrolytes due to the enhanced transport of the charge carrier, especially with the contributions from the edge-sharing Li-ion polyhedra of the LiSiNOS solid-solutions.

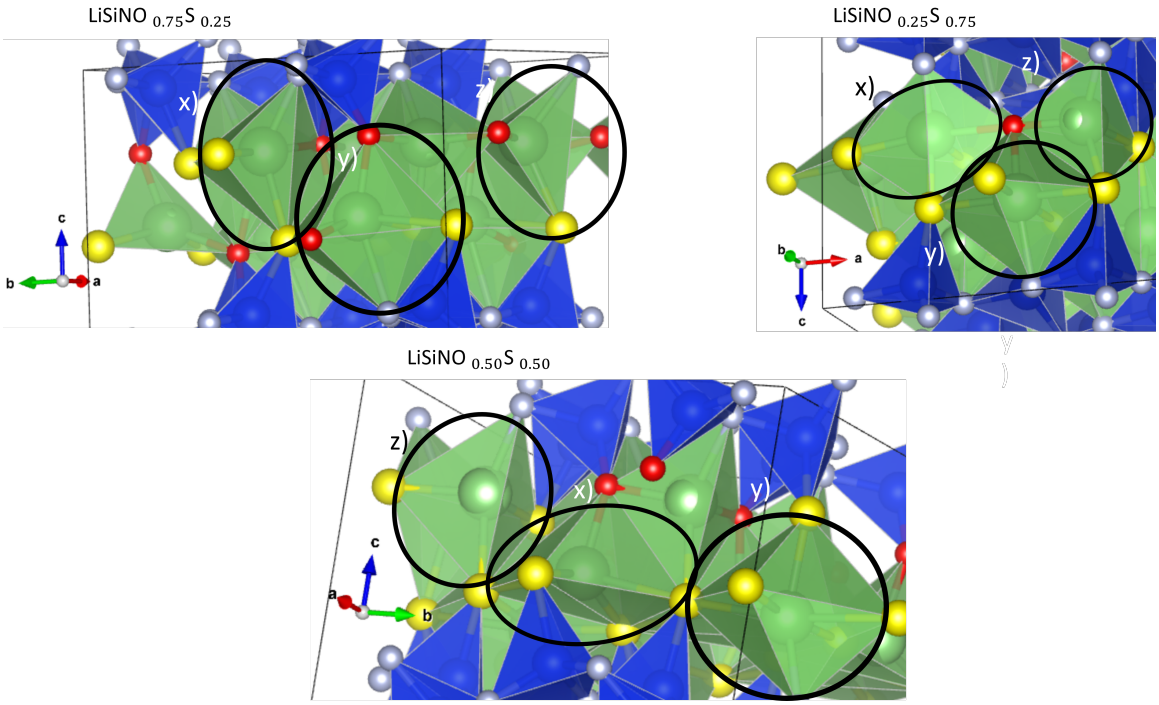

Figure 18: The figure illustrates the distorted LiO_xS_y tetrahedra, x), $LiNS_5$ octahedra, y), and $LiNO_3$ tetrahedraz), in $LiSiNO_{0.75}S_{0.25}$, a), $LiSiNO_{0.50}S_{0.50}$, and $LiSiNO_{0.25}S_{0.75}$.

6.2 Band Gap and Electrochemical stability window

The band gap of the solid-solutions can be used to suggest the materials' electrochemical stability. The band-gap was calculated with the PBEsol functional, which systematically underestimates the band-gap of materials. Therefore the calculated values of the band gaps will be lower than any actual experimental values. However, since the band-gap of the endpoints LiSiNO, LiGeNO and LiSiNS have previously been calculated with the much more accurate HSE06 hybrid functional in the preliminary work, the trends of the solid-solutions between the endpoints are undoubtedly significant. It is evident from figure 11 that both substituting with Ge and S leads to a lower band gap. When analysing the band-gap of the LiSiGeNO solid-solutions, an initial larger drop from LiSiNO to $LiSi_{0.75}Ge_{0.25}NO$ from 5.365 eV to 4.429 eV is seen when compared to the further steps toward LiGeNO. The relatively larger drop results from the introduction of Ge's s-orbitals in the conduction band, which are evident in the DOS plots in Figure 11. For LiSiNO, the conduction band minimum is determined by the Si p-orbitals. However, the band-gap is lowered since the Ge s-orbitals are more penetrative than the Si p-orbitals. From there, the system experience a linear decrease in band-gap towards LiGeNO's 3.191 eV as the Ge concentration increases.

The LiSiNOS solid-solutions, as predicted, also experience a decrease in band gap as O is substituted for S. Similarly to the LiSiGeNO system, the LiSiNOS system experience an even more significant initial drop in band gap to 4.047 eV when substituting 25% O with S in LiSiNO. This drop is explained by the increased electron shielding of the Sulphur core. The increased shielding contributes

to a higher energy of the S p-orbitals, which increases the valence band maximum, thus decreasing the band gap. Then with increasing S concentration, a linear decrease towards the band-gap of LiSiNS at 3.711 eV is observed. A slight drop from the linearity is observed for the $LiSiNO_{0.25}S_{0.75}$ structure, which has a value of 3.746 eV. The drop could be correlated to the structure's irregularly low unit volume. If the unit cell is too small, the S p-orbitals might be blocked by neighbouring ions, which would lead to much higher energy. This drop in band gap could again further indicate that the $LiSiNO_{0.25}S_{0.75}$ configuration is more unstable. When comparing the LiSiGeNO and LiSiNOS structures, it is clear that the introduction of S to the LiSiNO structure causes a more significant initial drop in electrochemical stability compared to the more subtle drop from Ge s-orbitals' introduction. However, further increasing the S concentration has a much lower impact on the band gap than increasing the Ge concentration. In the preliminary work, the LiSiNO and LiSiNS structures were found to have a higher band gap as oxide and sulfide materials, at 7.166 eV and 4.954 eV, respectively, when compared to experimental values of LLZO, LLTO and LGPS[17][16][14].

Table 9: A comparison of the band-gap of the solid-solutions and the pure structures calculated with the PBEsol functional and the band-gaps of other competing solid-state electrolytes calculated with the PBE functional.

Structure	Band-gap [eV]
LiSiNO	5.365
$LiSi_{0.75}Ge_{0.25}NO$	4.429
NASICON	4.340[18]
LLZO	4.300[17]
$LiSiNO_{0.75}S_{0.25}$	4.047
$LiSi_{0.50}Ge_{0.50}NO$	4.007
$LiSiNO_{0.50}S_{0.50}$	3.971
$LiSiNO_{0.25}S_{0.75}$	3.746
LiSiNS	3.711
LISICON	3.630[18]
$LiSi_{0.25}Ge_{0.75}NO$	3.573
LiGeNO	3.191
LLTO	2.560[18]
LGPS	2.210[]

In table 9 the band-gaps of the solid-solutions calculated with the PBEsol functional are compared against band-gaps of competing oxide and sulfide materials calculated with the regular GGA-PBE functional. Although the competing solid electrolytes are calculated with the regular GGA-PBE functional, the difference in calculated band-gap between the two functionals is negligible as the main effect is a slight difference in bond lengths and cell volume[33][36]. From the table, it is evident that the band-gap of the $LiSi_{0.75}Ge_{0.25}NO$ material outperforms all the other competing oxide materials except for pure LiSiNO. Further, it shows that the band-gap of the sulfide materials $LiSiNO_{0.75}S_{0.25}$, $LiSiNO_{0.50}S_{0.50}$ and $LiSiNO_{0.25}S_{0.75}$, as well as the oxide solid-solution $LiSi_{0.50}Ge_{0.50}NO$, is only outperformed by the oxide materials LiSiNO, $LiSi_{0.75}Ge_{0.25}NO$, NASICON and LLZO. The all oxide material $LiSi_{0.25}Ge_{0.75}NO$ shows poorer performance, as it only outperforms the oxide materials LLTO and LiGeNO. Therefore, when analysing the band-gap of the solid-solutions, the $LiSi_{0.75}Ge_{0.25}NO$, $LiSi_{0.50}Ge_{0.50}$ $LiSiNO_{0.75}S_{0.25}$ structures shows the most promise in high electrochemical stability.

The results thus show that the LiSiNOS and LiSiGeNO solid-solutions all experience a decrease in band gap from the LiSiNO structures but still perform well compared to competing solid electrolytes. This comparison suggests that the materials may still have high electrochemical stability when mixed to solid-solutions. The results are also especially promising for the $LiSiNO_{0.75}S_{0.25}$ and $LiSiNO_{0.50}S_{0.50}$ materials, as they are sulfide materials with very large band gaps relative to other sulfide materials, which typically have higher Li mobility. However, the calculated band-gaps have not been aligned to the potential of any high-performing cathodes or anodes. This impedes the possibility of concluding the effect of using the materials together with any standard electrodes. However, the high band gaps do suggest possible high compatibility for usage with high voltage cathodes to achieve battery cells with higher specific capacity and operating voltage.

6.3 Kinetics

6.3.1 Short term Li trajectories

100 ps of each structure were simulated to analyse the short-term Li displacements in each structure. The presented MSD measurements of each structure in figure 13 illustrate the degree of displacement of each Li-ion from its original reference position over a short time period of 60 ps. From the figure, it is clear to see that the Li-ions in the LiSiNOS solid-solutions deviate further from their reference site position than the Li-ions in the LiSiGeNO solid-solutions. LiSiNO starts with MSD values at around 0.19 $Å^2$, then $LiSiNO_{0.75}S_{0.25}$ increases to 0.29 $Å^2$ before reaching a maximum with $LiSiNO_{0.50}S_{0.50}$ at approximately 0.40 $Å^2$. The Li-ion MSD value then drops down to 0.19 $Å^2$ again with $LiSiNO_{0.25}S_{0.75}$ before LiSiNS ends at about 0.35$Å^2$. The initial increase can be explained by the larger unit cell when going to 25% and 50% S, giving the Li-ion more room to manoeuvre in, and the increasing softness of the anion lattice enabling more Li movement. Another explanation can be that introducing $LiNOS_3$ distorted tetrahedra, and LiS_5 octahedra again give the affected Li-ion more manoeuvrability. The significant drop in MSD for the 25% O and 75% S can be explained by the large drop in unit cell volume inhibiting Li movements and perhaps a change in the anion lattice. The LiSiGeNO solid-solutions, though, have much less MSD value variability for the different structures. For these solid-solutions we see a small increase going from LiSiNO to $LiSiNO_{0.75}S_{0.25}$ to $LiSiNO_{0.50}S_{0.50}$. Then we see a similar small decrease in value going further to $LiSiNO_{0.25}S_{0.75}$ and LiSiNS. The increase in unit cell volume can explain the initial increase in mobility. However, the decline in mobility after 50% Ge substitution might be explained by the high concentration of the larger-sized Ge ions starting to counteract the benefits of the larger volume and again start to inhibit Li movements. Additionally, does the substitution of Si with Ge mainly affect the non-conducting Si- and Ge tetrahedra layer. Since the Li-ions mainly migrate between Li-polyhedra in the (a,b)-layer, a change in the Si- and Ge polyhedra layer will therefore have little impact on the mobility of the Li-ions.

When comparing the values between the LiSiNOS and LiSiGeNO solid-solutions it is clear that substituting O for S gives a much greater impact on the local Li movement than substituting Si for Ge. This suggests that Li movement in LiSiNO structures is less dependent on unit cell size than on anion softness and Li-polyhedra. The comparatively much higher MSD values for the LiSiNOS solid-solutions suggest a possibility for a higher Li-diffusion and higher hopping frequency. Thus it can be concluded that the $LiSiNO_{0.50}S_{0.50}$ solid-solution have the best local short-term Li mobility, which indicates a possibility of the solid-solution having a higher conductivity of both LiSiNO and LiSiNS as well as the other solid-solutions investigated.

6.3.2 Long term diffusion

The observed trends of the MSD of the Li-ions from the 10 ns simulations are consistent with the trends of the short-term 100 ps simulations. Again the LiSiGeNO show Little change when increasing the concentration of Ge, while LiSiNOS show an increase towards a peak at 50% O and 50% S and then a drop for the $LiSiNO_{0.25}S_{0.75}$ structure. The results' consistency speaks to the ML-MD method's reliability in reproducing results. The most important result from the long-term simulations was the observed linear increase in mean square displacement for the Li ions of the $LiSiNO_{0.75}S_{0.25}$ and $LiSiNO_{0.50}S_{0.50}$ structures. A linear increase in MSD signifies movement of the Li-ions. This phenomenon could therefore signify an accomplished diffusive regime in the structures. The diffusion coefficients and the maximum likelihood values for the activation energy for $LiSiNO_{0.75}S_{0.25}$ and $LiSiNO_{0.50}S_{0.50}$ were estimated and are presented in Table 10.

Table 10: The estimated diffusion coefficient and the estimated maximum likelihood value for the activation energy for $LiSiNO_{0.75}S_{0.25}$ and $LiSiNO_{0.50}S_{0.50}$.

	$LiSiNO_{0.75}S_{0.25}$	$LiSiNO_{0.50}S_{0.50}$
D $[cm^2/s]$	2.06 ($\pm$1.20) $\cdot 10^{-11}$	1.04 ($\pm$0.48) $\cdot 10^{-10}$
$E_a[eV]$	2.43 ($\pm$0.63)	3.99 ($\pm$0.84)

The estimated values of Li self-diffusion coefficients are considerably low, which would signify inferior Li conductivity for the materials. Improved Li-ion conductivity is one of the most critical aspects of solid-state electrolytes; therefore, these numbers would strongly argue against the use of the solid-solutions as solid electrolytes. However, the estimated activation energy results are not consistent with the activation energy previously found for LiSiNO, LiSiNS and LiGeNO. This discrepancy might thus suggest that the achieved regime from the long-term simulations does not correspond to a Li diffusion regime.

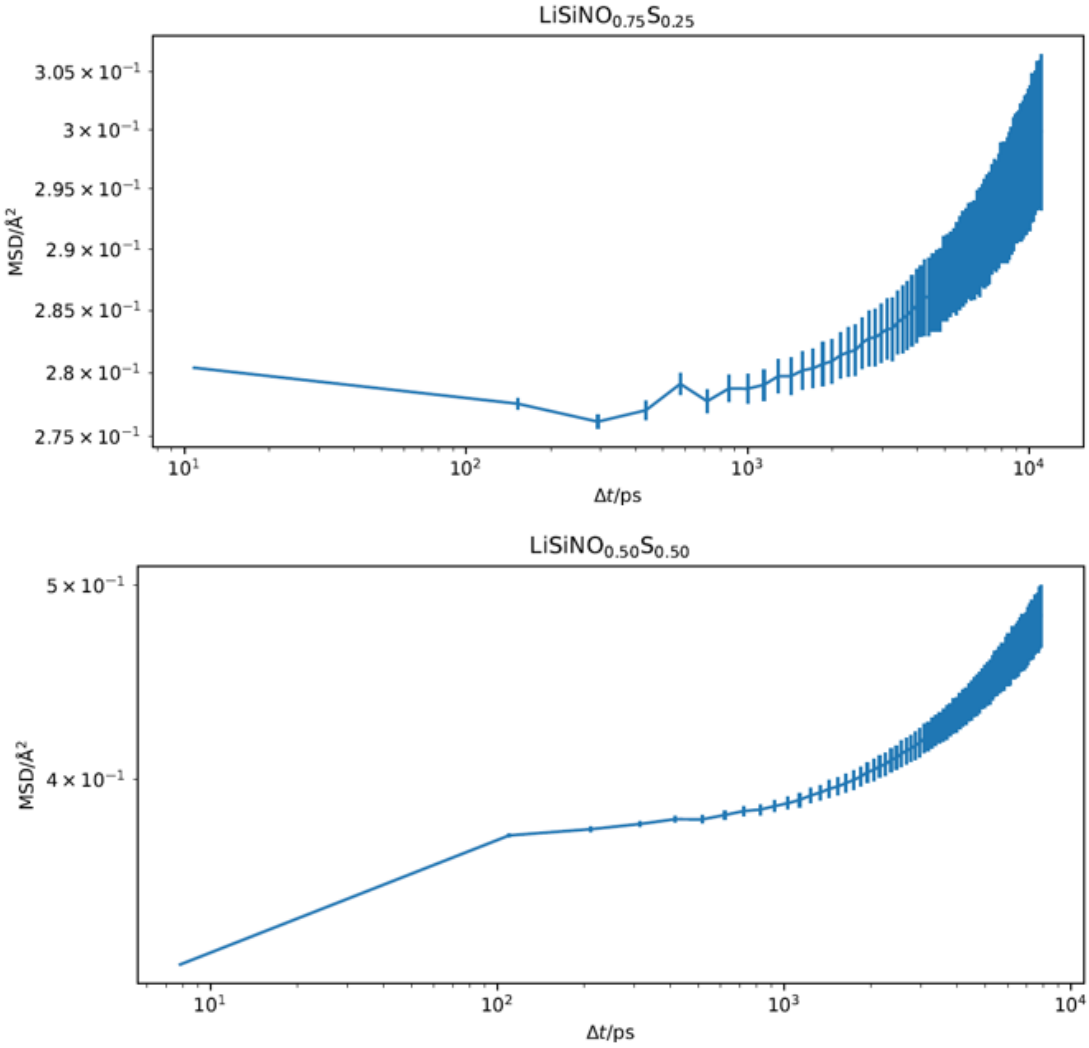

Figure 19: The calculated Li-MSD for $LiSiNO_{0.75}S_{0.25}$ and $LiSiNO_{0.50}S_{0.50}$ plotted against the simulated time on a logarithmic scale.

To more closely study the Li-MSD regimes for the structures, the MSD can be plotted on the logarithmic scale. The Li MSD for $LiSiNO_{0.75}S_{0.25}$ and $LiSiNO_{0.50}S_{0.50}$ are plotted with logarithmic axes in Figure 19. Both simulations show an initial low value in Li-MSD, followed by a steep non-linear increase when plotted on a logarithmic scale These regions of steep increase might actually signify ballistic regimes, where the Li-ions move within their coordination site without interfering with other particles. This would explain the low diffusion coefficients and high activation energy, as diffusion is not actually observed.

6.4 Li-ion Mobility

A nudged elastic band analysis was performed on $LiSiNO_{0.75}S_{0.25}$ to be able to get a better understanding of the Li-ion mobility, as well as compare the results of the long-term ML-MD simulations. The $LiSiNO_{0.75}S_{0.25}$ structure was chosen due to the achieved complete 10 ns ML-MD simulations suggesting a Li-ion diffusion regime. Three distinct Li-ion migration paths were found for an inserted Li-ion vacancy. It is evident from Table 8 that path three had the lowest migration energy barrier at 0.236 eV, followed by path one, which had an energy barrier of 0.309, and finally path two had the highest migration energy barrier at 0.645 eV. What is noticeable is the considerable difference between Path one and three and path two, at 2.30 Å, 2.89 Å and 4.08 Å, respectively. The shorter migration distance of path one and three could contribute to the lower migration barrier. The three paths are further illustrated in Figure 20, 21 and 22.

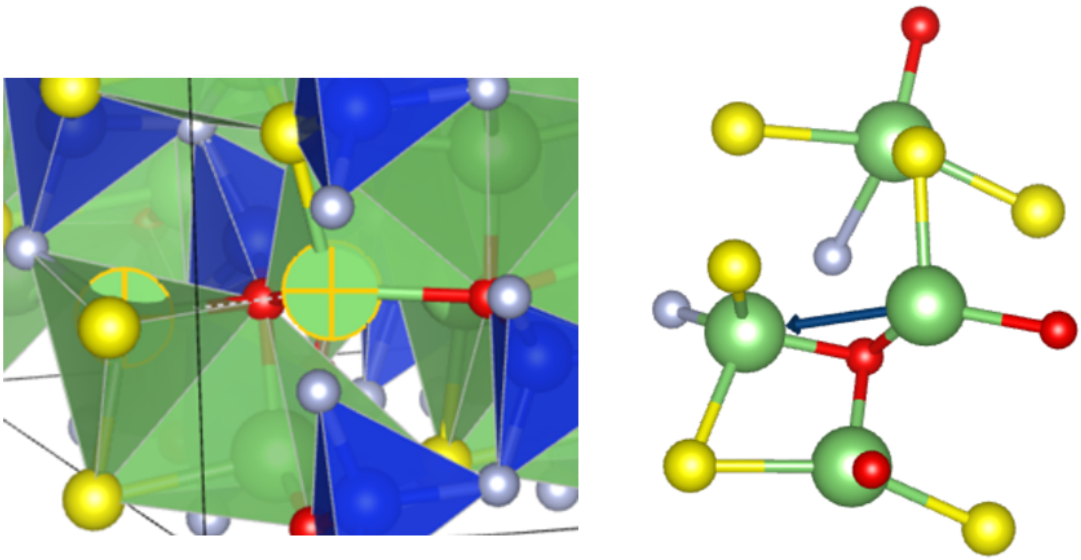

Figure 20: Illustration of Li-ion migration path 3 found in $LiSiNO_{0.75}S_{0.25}$

The low migration barrier of path three could be further explained by the local polyhedra surrounding the Li-ion. Figure 16 shows the Li-ion being located in a $LiNO_2S$ tetrahedron, where the migration path exits through the face of the tetrahedron and again enters through the face of the vacancy site $LiNOS_2$ tetrahedra, which it shares its corner with. The path leading through the face planes of the two tetrahedra results in a migration path with a large bottleneck. This significant bottleneck and the short migration distance lead to a quite low migration energy barrier. When comparing path three's migration energy barrier between $LiSiNO_{0.75}S_0.25$ and LiSiNOS, one can see that LiSiNO have the lowest energy barrier at 0.17 eV. This increase in energy is consistent with the increase in energy seen in LiSiNS, which had a migration barrier at 0.354 eV.

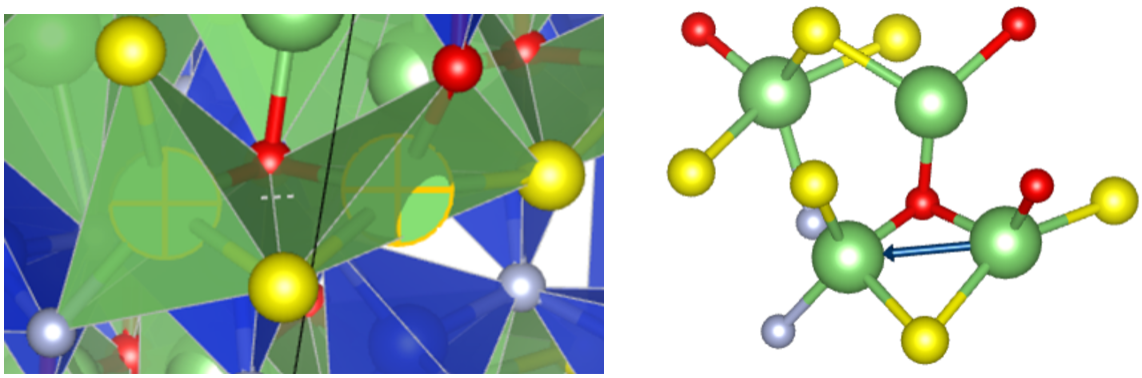

Figure 21: Illustration of Li-ion migration path 1 found in $LiSiNO_{0.75}S_{0.25}$

The second-lowest migration barrier, at 0.310 eV, was found in path 1. Again the migration barrier can be explained by the bottleneck of the path. Here does Li_2 inhibit a $LiNO_2S_3$ octahedron. The complete polyhedron of the ion position is not shown in figure 21 due to the imposed boundary condition. The Li-paths cross into the Li_1 tetrahedra through the shared edge. This edge creates a smaller bottleneck compared to the plane of the tetrahedra, which thus increases the energy barrier. Therefore the migration energy barrier is higher than for path 3, even though the edge-sharing properties lead to a shorter migration path. What is characteristic about path one, is the fact that the end position of the path have a higher energy compared to the start position. This means that the initial position is more stable than the end position. Additionally, the energy of the end position has almost as high energy as the energy peak of the path. The lower energy of the initial position would indicate a lower formation energy for the $LiNO_2S_3$ octahedra.

When compared to the equivalent Li migration path in LiSiNO, the migration energy barrier in $LiSiNO_{0.75}S_0.25$ is lower than LiSiNO's energy barrier at 0.422 eV. This decrease is a result of the increased polyhedra size caused by the introduction of the S-ions. The $LiSiNO_{0.75}S_0.25$ solid-solution also has a lower energy barrier than LiSiNS at 0.363. Therefore there might be a limit where the benefit of the increased polyhedra is surpassed by the detriment of the large S ions hindering migration.

Li migration path two had the highest migration energy barrier at 0.65 eV and the longest migration distance. This Li-ion is also located in a distorted $LiNO_2S_2$ tetrahedron. However, this distorted tetrahedron does not share an edge with the vacancy tetrahedra and therefore faces a longer migration path. Additionally, does the Li-ion not exit through the face-plane but rather through the one larger edge of the distorted tetrahedra. This geometry results in a smaller bottleneck compared to the more open face-plane exit of path 1. The smaller bottleneck combined with the longer migration results in a substantially higher migration energy barrier. The equivalent migration path in LiSiNO had a lower barrier at 0.59 eV, while LiSiNS's barrier of 0.76 eV again was higher. The trend of paths two and three show the expected results of substituting O of S, drifting the energy barrier of each specific path from the values of LiSiNO and toward that of LiSiNS. While the migration energy barrier of path one further decreases below the migration barrier of LiSiNS. The result then is that both paths two and three increase in energy, while path one decreases.

The average migration energy barrier of competing oxide and sulfide solid-state electrolytes was presented in Table 1. When comparing the calculated migration energy barriers of the

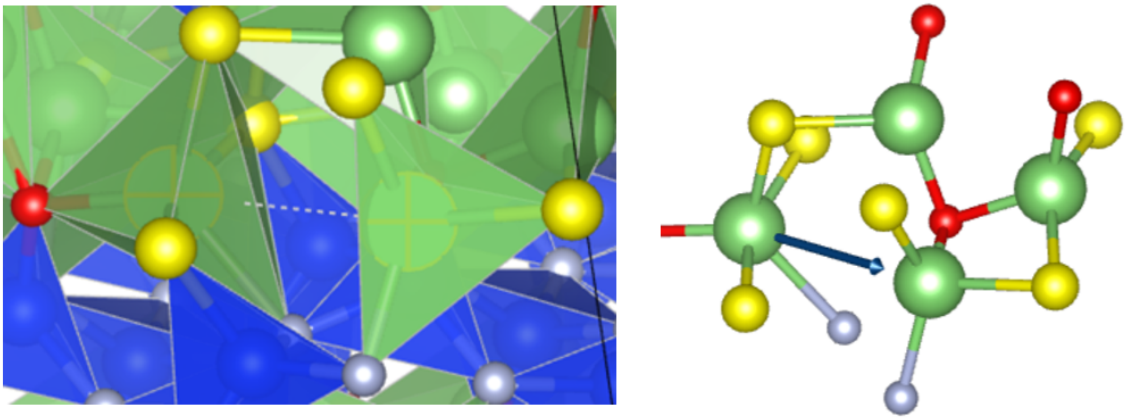

Figure 22: Illustration of Li-ion migration path 2 found in $LiSiNO_{0.75}S_{0.25}$

$LiSiNO_{0.75}S_{0.25}$ with the competing materials, the solid-solution emerges quite favourably against the oxide materials. Most of the competing oxide materials had a minimum of around 0.30-0.35 eV and a maximum of 0.40 eV. The exception here is the LISICON materials which had average migration energy barriers at 0.40-0.60 eV. However, this material can experience superionic conductivity, giving rise to a higher ionic conductivity despite higher migration barriers. The Lowest migration barrier of 0.24 eV for path three ranks well below the average minimum of the competing materials. Secondly, does the migration barrier of path one at 0.31 eV lay just above the lowest average migration barrier of LLTO and NASICON, while still below that of LLZO. However, the high migration barrier of path two at 0.65 eV is well over the maximum average of that of LLTO and NASICON, and lies around the maximum of LLZO. However, the results are quite middling compared to the sulfide materials. Only path 3 are on par with the average migration barrier of LGPS, being between 0.20-0.25 eV, while path 1 and 2 are quite high in comparison. The vast difference in values for the migration energy barrier found with the NEB analysis and the long-term ML-MD analysis further reinforces the theory that the regime observed for $LiSiNO_{0.75}S_{0.25}$ and $LiSiNO_{0.25}S_{0.75}$ were not a diffusion regime. Therefore, the estimated diffusion coefficient values and the maximum likelihood value for the activation energy estimated from the long-term ML-MD simulations are inaccurate for the materials.

7 Conclusion

The aim of this master's thesis was to analyse the structural data, band-gap and Li-migration of solid solutions between LiSiNO and LiGeNO and LiSiNS. Using DFT-calculations were the structures $LiSi_{1-x}Ge_xNO$ and $LiSiNO_{1-x}S_x$ with 25%, 50% and 75% substitution simulated and geometry optimised. Both the enthalpy of mixing and the Gibbs free energy mixing of the two systems were positive, proving the mixing to solid-solution to be an endothermic process. Analysing the solid-solutions relation to Vegard's law showed a large deviation from linearity of the c-lattice parameter for $LiSiNO_{0.25}S_{0.75}$, thus suggesting lower stability of the solid-solution's configuration. The result from the geometry optimisation further showed that the average coordination number of Li increased with S concentration leading to an increased amount of $LiNO_xS_y$ distorted tetrahedra and octahedra.

The analysis of the calculated density of states and band gap showed a decrease in band gap following increased Ge and S concentration. The results showed an initial larger drop for both $LiSi_{0.75}Ge_0.25NO$ and $LiSiNO_{0.75}S_{0.25}$ from LiSiNO, followed by a linear decrease towards the values of LiGeNO and LiSiNS respectively. The decrease in band gaps was due to the introduction of Ge's more penetrating s-orbitals lowering the conduction-band minimum of the LiSiGeNO structures and the increased shielding of the S core contributing to raising the valence-band maximum of the LiSiNOS structures. However, the LiSiGeNO structures still performed well compared to competing oxide solid-state electrolytes, especially $LiSi_{0.75}Ge_{0.25}$ which outperformed NASICON, LLZO, LISICON and LLTO despite having a lower band-gap of LiSiNO. The LiSiNOS solid-solutions also performed very well compared to the sulfide materials LGPS and LiSiNS. Although the band gaps were not aligned to the potentials of any cathodes and anodes, the electronic structure analysis concludes that the substitution of Si with Ge or O with S leads to decreased electrochemical stability.

A machine-learning molecular dynamics method was used to simulate 100 ps and 10 ns of the pure phases and the solid-solutions to analyse the Li-ion mobility in the solid-solution. The LiSiNOS materials showed a noticeable increase in Li-ion MSD when substituting O with S, which ultimately peaked with the $LiSiNO_{0.50}S_{0.50}$ structure. The LiSiGeNO system, however, did not show any development in Li-ion MSD with increased Ge concentration. The same trends were observed in the long-term ML-MD simulations, thus further supporting the reliability of the method. However, no diffusion regime was accomplished over the simulated 10 ns for any of the materials. Only a ballistic regime was observed for the $LiSiNO_{0.75}S_{0.25}$ and the $LiSiNO_{0.50}S_{0.50}$. A nudged elastic band analysis was performed on the $LiSiNO_{0.75}S_{0.25}$ structure to estimate the Li-ion migration further. Three Li-ion migration paths, equivalent to the three previously found in LiSiNO and LiSiNS, were found to an inserted Li vacancy. The three paths had migration energy barriers of 0.31, 0.65 and 0.24 eV, thus having one path with a relatively low energy barrier, one with a satisfactory energy barrier and one with a relatively high energy barrier. The materials thus showed the expected pattern of the energy barriers transitioning from the values found in LiSiNO towards that of LiSiNS' energy barriers, with the energy of path one even decreasing below that of LiSiNS.

The conclusion of the master is, therefore, that the process of mixing to the two solid-solution systems are both slightly endothermic. However, both systems show that substitution leads to lower electrochemical stability, while only LiSiNOS suggest improved Li-ion conductivity. Therefore the LiSiGeNO solid-solutions were not found to be suitable as solid-state electrolytes as it does not improve on the LiSiNO material. However, the LiSiNOS solid-solution was found to be promising, especially $LiSiNO_{0.50}S_{0.50}$ as it still shows promising electrochemical stability while seemingly improving Li-ion migration.

8 Further work

For further work, a much greater and more extensive analysis of all the possible configurations of the solid-solutions is needed. As in this thesis, only a fraction of the total configuration was analysed. This means that the results from this analysis are only an indication of what the larger picture of the solid-solutions would look like. Although the results from the total energy per atom of the configurations analysed, suggest little difference in energy between the different configurations. The exception is the $LiSiNO_{0.25}S_{0.75}$ solid-solution that experienced a significant difference in cell volume between the different configurations. The importance of an adequate configuration analysis is that the placement of the substituted ions can greatly affect the energy of the crystal structure. Therefore it is crucial to be certain that the configuration that is analysed would occur experimentally. The vast amount of possible non-symmetry equivalent configurations for each solid-solution demands a configuration analysis that can cheaply and superficially gather data about the energy of each configuration. Then a deeper analysis of the energy of the most promising configurations must follow.

Further, a longer and more extensive MD simulations must be performed to more accurately analyse the Li migration in the LiSiNO materials. In this analysis, a supercell with a size of 128 ions and a time frame of 10 ns was chosen to make the calculations feasible in the available time frame of the master thesis. However, with a too-small simulation cell, finite-size effects might occur. This means that the diffusing particles can influence nearby diffusing particles, and when the cell is too small, these particles might influence their mirror particle beyond the border conditions, leading to non-representative results. The simulated time frame also needs to be long enough for the Li particles to reach a diffusive regime for the diffusing particles in the material. Therefore, a thorough MD analysis over a much longer time and larger supercell is needed to understand the materials' Li-diffusion mechanics beyond that of specific NEB analysis at 0K. Additionally, would alignment of the calculated band-gap to high-performing cathodes and anodes be needed to better understand the electrochemical stability window. The band gap alone is not enough to draw any concrete conclusion about the electrochemical stability of the materials, as their VB-maximum and CB-minimum relative to the applied electrodes define the electrochemical stability.

For further work beyond what is mentioned so far in the analysis, could heterovalent doping of the LiSiNO materials be interesting. By utilising heterovalent doping, the charge carrier density can be increased by introducing more vacancies. The LiSiNO structures can be P-doped by substituting Si^{4+} with higher valency ions, such as 5+. An example might be substituting Si^{4+} with P^{5+} or Mn^{5+}. An advantage of doping with P^{5+} rather than Mn^{5+} is the better availability of P compared to Mn, which might lead to cheaper materials. Lastly, will an experimental sample production be precious to accurately describe the electrochemical stability and Li-ion conductivity at operating temperatures of the LiSiNO materials.

Even though the LiSiGeNO solid-solutions were not found to improve upon LiSiNO as a solid-state electrolyte, the materials could be utilised for different applications. As solid-solutions they could perhaps be used as n-type thermoelectrics. The fact that the depth of the conduction band can be changed as a function of Ge concentration could create an electronic structure favourable for n-type thermoelectrics. However, the materials' high band-gap could be an issue, as semiconductors are preferable for the use as n-type thermoelectrics[54]. If the solid-solutions exhibit the flat band edges seen in LiSiNO and LiGeNO the solid-solutions could achieve higher values of the Seebeck coefficient as solid-solutions, which would be crucial to be able to reach satisfactory ZT values.[54].

References

[1] IEA, "Global ev outlook," *IEA, Paris*, 2021.

[2] H. Abdi, B. Mohammadi-ivatloo, S. Javadi, A. R. Khodaei, and E. Dehnavi, "Chapter 7 - energy storage systems," in *Distributed Generation Systems* (G. Gharehpetian and S. M. Mousavi Agah, eds.), pp. 333–368, Butterworth-Heinemann, 2017.

[3] "Chapter 5 - integrated ess application and economic analysis," in *Grid-scale Energy Storage Systems and Applications* (F.-B. Wu, B. Yang, and J.-L. Ye, eds.), pp. 153–201, Academic Press, 2019.

[4] C. Liu, Z. G. Neale, and G. Cao, "Understanding electrochemical potentials of cathode materials in rechargeable batteries," *Materials Today*, vol. 19, no. 2, pp. 109–123, 2016.

[5] D. Na, B. Lee, B. Yoon, and I. Seo, "A solid-state thin-film electrolyte, lithium silicon oxynitride, deposited by using rf sputtering for thin-film batteries.," pp. 855–859, 2020.

[6] X. Zhang, L. Guo, B. Zhang, J. Yu, Y. Wang, K. Wu, H.-j. Wang, and M.-H. Lee, "From silicates to oxonitridosilicates: improving optical anisotropy for phase-matching as ultraviolet nonlinear optical materialselectronic supplementary information (esi) available: Calculated results of (sinxo4x)(4+x) (x = 0, 1, 2, 3, 4) anionic groups, the crystal structures of oxonitridosilicates, and electronic structures of si2n2o and lisino. see doi: 10.1039/d0cc07269a," vol. 57, no. 5, pp. 639–642, 2021.

[7] P. B. Balbuena, "Electrolyte materials - issues and challenges," *AIP Conference Proceedings*, vol. 1597, no. 1, pp. 82–97, 2014.

[8] M. D. Tikekar, S. Choudhury, Z. Tu, and L. A. Archer, "Design principles for electrolytes and interfaces for stable lithium-metal batteries," 2016.

[9] A. Yoshino, "The birth of the lithium-ion battery," *Angewandte Chemie International Edition*, vol. 51, no. 24, pp. 5798–5800, 2012.

[10] Y. Luo, F. Zheng, L. Liu, K. Lei, X. Hou, G. Xu, H. Meng, J. Shi, and F. Li, "A high-power aqueous zinc–organic radical battery with tunable operating voltage triggered by selected anions," *ChemSusChem*, vol. 13, no. 9, pp. 2239–2244, 2020.

[11] J. Lu, Z. Chen, Y. Cui, and K. Amine, "High-performance anode materials for rechargeable lithium-ion batteries," *Electrochemical Energy Reviews* ***1***, pp. 35–53, 2018.

[12] J. Kasemchainan, S. Zekoll, D. S. Jolly, Z. Ning, G. O. Hartley, J. Marrow, and P. G. Bruce, "Critical stripping current leads to dendrite formation on plating in lithium anode solid electrolyte cells," *Nature Materials,* ***18***, p. 1105–1111, 2019.

[13] T. Krauskopf, F. H. Richter, W. G. Zeier, and J. Janek, "Physicochemical concepts of the lithium metal anode in solid-state batteries," *Chemical Reviews*, vol. 120, no. 15, pp. 7745–7794, 2020. PMID: 32786669.

[14] T. Famprikis, P. Canepa, J. A. Dawson, and et. al., "Fundamentals of inorganic solid-state electrolytes for batteries," *Nat. Mater.* ***18***, p. 1278–1291, 2019.

[15] S. Ohno and et. al., "Materials design of ionic conductors for solid state batteries," *Progress in Energy*, vol. 2, 2020.

[16] S. Lou, F. Zhang, C. Fu, M. Chen, Y. Ma, G. Yin, and J. Wang, "Interface issues and challenges in all-solid-state batteries: Lithium, sodium, and beyond," *Advanced Materials*, vol. 33, no. 6, p. 2000721, 2021.

[17] H.-K. Tian, B. Xu, and Y. Qi, "Computational study of lithium nucleation tendency in li7la3zr2o12 (llzo) and rational design of interlayer materials to prevent lithium dendrites," *Journal of Power Sources*, vol. 392, pp. 79–86, 2018.

[18] T. Binninger, A. Marcolongo, M. Mottet, V. Weber, and T. Laino, "Comparison of computational methods for the electrochemical stability window of solid-state electrolyte materials," *J. Mater. Chem. A*, vol. 8, pp. 1347–1359, 2020.

[19] Y. Y. Ma, F. Xiao, S. Ye, Q. Y. Zhang, Z. H. Jiang, and Y. Qian, "Electronic and luminescence properties of LiSiON: Eu2, eu2/mn2as a potential phosphor for UV-based white LEDs," *ECS Journal of Solid State Science and Technology*, vol. 1, no. 1, pp. R1–R6, 2012.

[20] M. Weller, T. Overton, J. Rourke, and F. Armstrong, *Inorganic Chemistry*. Oxford University Press, 2010.

[21] S. Stølen, T. Grande, and N. L. Allan, *Chemical Thermodynamics of Materials*. John Wiley Sons, Ltd, 2005.

[22] A. M. Ganose and D. O. Scanlon, "Band gap and work function tailoring of sno2 for improved transparent conducting ability in photovoltaics," *J. Mater. Chem. C*, vol. 4, pp. 1467–1475, 2016.

[23] R. J. D. Tilley, *Understanding solids: The Science of Materials*. Wiley Sons, Ltd, 2013.

[24] A. R. West, *Solid State Chemistry And its Application*. Wiley Sons, Ltd, 2014.

[25] T. K. Schwietert, A. Vasileiadis, and M. Wagemaker, "First-principles prediction of the electrochemical stability and reaction mechanisms of solid-state electrolytes," *JACS Au*, vol. 1, no. 9, pp. 1488–1496, 2021.

[26] J. B. Goodenough and Y. Kim, "Challenges for rechargeable li batteries," *Chemistry of Materials*, vol. 22, no. 3, pp. 587–603, 2010.

[27] F. Jensen, *Introduction to Computational Chemistry*. John Wiley and Sons, Ltd., 2nd ed. ed., 2007.

[28] A. R. Leach, "Molecular modelling : principles and applications," 2001.

[29] J. Z. H. Zhang, *Theory and Application of Quantum Molecular Dynamics*. World Scientific Publishing Co. Pte. Ltd., 1999.

[30] D. S. Sholl and J. A. Steckel, *Density Functional Theory: a Practical Introduction*. John Wiley Sins, Inc, 2009.

[31] T. Shida, *The Chemical Bond, A Fundamental Quantum-Mechanical Picture*. Springer-Verlag, 2004.

[32] K. A. Baseden and J. W. Tye, "Introduction to density functional theory: Calculations by hand on the helium atom," *Journal of Chemical Education*, vol. 91, no. 12, pp. 2116–2123, 2014.

[33] M. Siddique, A. U. Rahman, A. Iqbal, B. Ul Haq, S. Azam, and A. Nadeem, Asif Qayyum, "A systematic first-principles investigation of structural, electronic, magnetic, and thermoelectric properties of thorium monopnictides thpn (pn=n, p, as): A comparative analysis of theoretical predictions of lda, pbesol, pbe-gga, wc-gga, and lda+u methods," *Int J Thermophys*, vol. 40, 2019.

[34] G.-X. Zhang, A. M. Reilly, A. Tkatchenko, and M. Scheffler, "Performance of various density-functional approximations for cohesive properties of 64 bulk solids," *New Journal of Physics*, vol. 20, p. 063020, jun 2018.

[35] J. M. Skelton, D. Tiana, S. C. Parker, A. Togo, I. Tanaka, and A. Walsh, "Influence of the exchange-correlation functional on the quasi-harmonic lattice dynamics of ii-vi semiconductors," *The Journal of Chemical Physics*, vol. 143, no. 6, p. 064710, 2015.

[36] I. A. G. Ramirez, L. A. A. Varilla, and J. A. Montoya, "A DFT study about the effects of exchange-correlation functional on the structural and electronic properties of anatase," *Journal of Physics: Conference Series*, vol. 1219, p. 012019, may 2019.

[37] D. Frenkel, "Understanding molecular simulation : from algorithms to applications," 2002.

[38] D. Marx, "Ab initio molecular dynamics : basic theory and advanced methods," 2009.

[39] S. Nosé, "A unified formulation of the constant temperature molecular dynamics methods," *The Journal of Chemical Physics*, vol. 81, no. 1, pp. 511–519, 1984.

[40] R. Jinnouchi, J. Lahnsteiner, F. Karsai, G. Kresse, and M. Bokdam, "Phase transitions of hybrid perovskites simulated by machine-learning force fields trained on the fly with bayesian inference," *Phys. Rev. Lett.*, vol. 122, p. 225701, Jun 2019.

[41] R. Jinnouchi, F. Karsai, and G. Kresse, "On-the-fly machine learning force field generation: Application to melting points," *Phys. Rev. B*, vol. 100, p. 014105, Jul 2019.

[42] R. Jinnouchi, F. Karsai, C. Verdi, R. Asahi, and G. Kresse, "Descriptors representing two- and three-body atomic distributions and their effects on the accuracy of machine-learned inter-atomic potentials," *The Journal of Chemical Physics*, vol. 152, no. 23, p. 234102, 2020.

[43] K. Okhotnikov, T. Charpentier, and S. Cadars, "Supercell program: a combinatorial structure-generation approach for the local-level modeling of atomic substitutions and partial occupancies in crystals," *Journal of Cheminformatics*, vol. 8, 2016.

[44] G. Kresse and J. Hafner *Phys. Rev.*, B47, 558 (1993); ibid. 49 , 14 251 (1994).

[45] G. Kresse and J. furthermåller *Comput. Mat. Sci.*, 6 , 15 (1996).

[46] G. Kresse and J. furthermåller *Phys. Rev.*, B 54 , 11 169 (1996).

[47] R. Grau-Crespo, S. Hamad, C. R. A. Catlow, and N. H. de Leeuw, "Symmetry-adapted configurational modelling of fractional site occupancy in solids," *Journal of Physics: Condensed Matter*, vol. 19, p. 256201, may 2007.

[48] Z. Rong, D. Kitchaev, P. Canepa, W. Huang, and G. Ceder, "An efficient algorithm for finding the minimum energy path for cation migration in ionic materials," *The Journal of Chemical Physics*, vol. 145, no. 7, p. 074112, 2016.

[49] B. J. Morgan, "Mechanistic origin of superionic lithium diffusion in anion-disordered li6ps5x argyrodites," *Chemistry of Materials*, vol. 33, no. 6, pp. 2004–2018, 2021. PMID: 33840894.

[50] G. Krenzer, C.-E. Kim, K. Tolborg, B. J. Morgan, and A. Walsh, "Anharmonic lattice dynamics of superionic lithium nitride," *J. Mater. Chem. A*, vol. 10, pp. 2295–2304, 2022.

[51] I. K, Momma F, "Vesta 3 for three-dimensional visualization of crystal, volumetric and morphology data."

[52] A. M. Ganose, A. J. Jackson, and D. O. Scanlon, "sumo: Command-line tools for plotting and analysis of periodic *ab initio* calculations," *Journal of Open Source Software*, vol. 3, no. 28, p. 717, 2018.

[53] J. D. Hunter, "Matplotlib: A 2d graphics environment," *Computing in Science & Engineering*, vol. 9, no. 3, pp. 90–95, 2007.

[54] K. B. Spooner, A. M. Ganose, W. W. W. Leung, J. Buckeridge, B. A. D. Williamson, R. G. Palgrave, and D. O. Scanlon, "Babi2o6: A promising n-type thermoelectric oxide with the pbsb2o6 crystal structure," *Chemistry of Materials*, vol. 33, no. 18, pp. 7441–7456, 2021.

Appendix

A Configurations

A.1 $LiSiNO_{0.75}S_{0.25}$

Here are the total energy per atom for each of the geometry-optimised configurations for each solid-solutions presented.

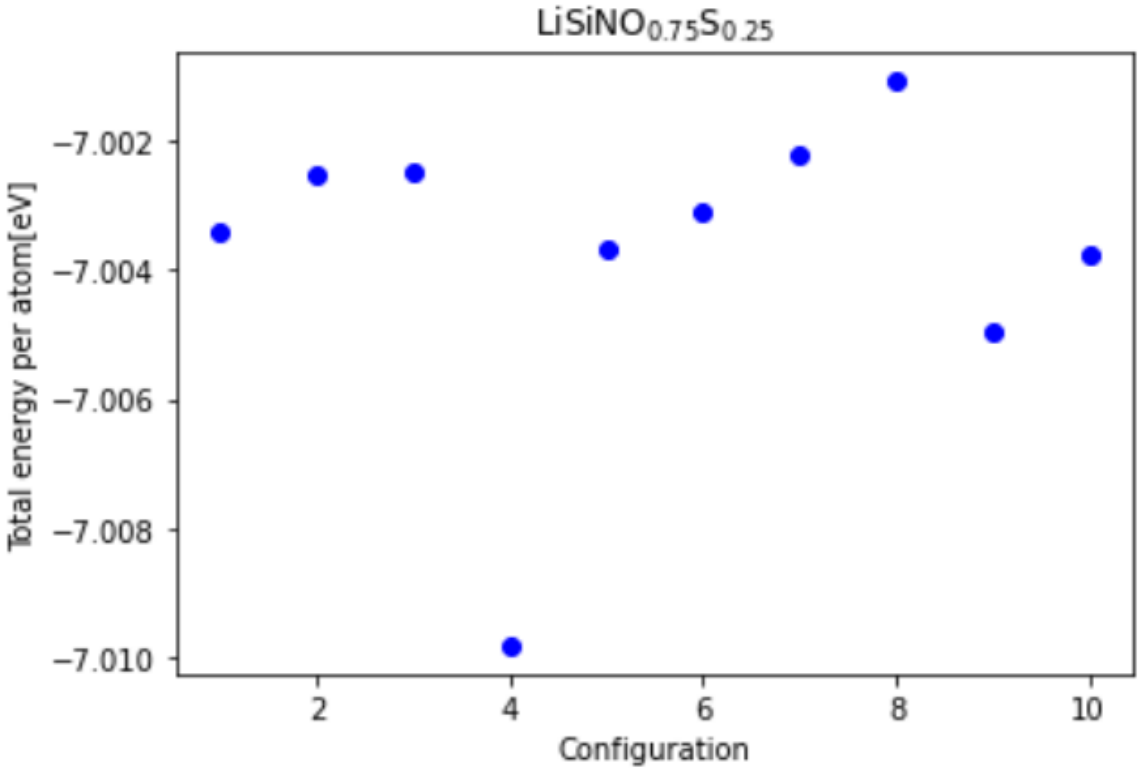

Figure 23: The total energy per atom for each of the ten configurations chosen of $LiSiNO_{0.75}S_{0.25}$.

A.2 $\mathbf{LiSiNO_{0.50}S_{0.50}}$

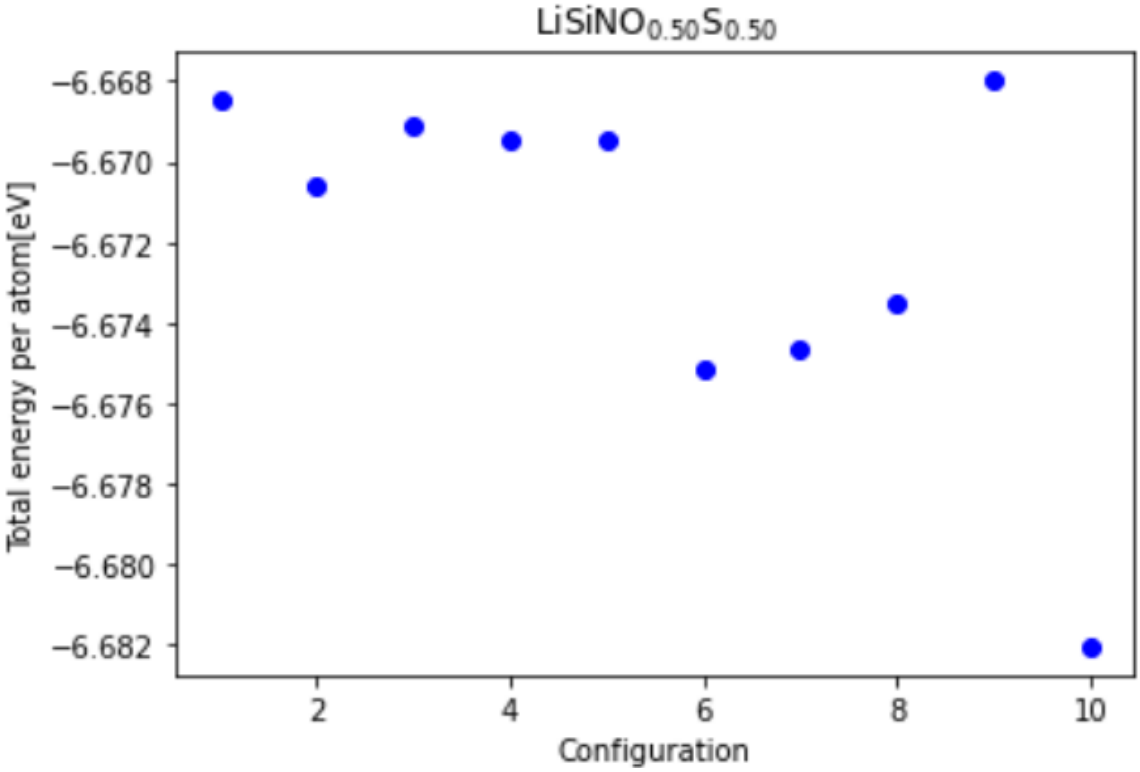

Figure 24: The total energy per atom for each of the ten configurations chosen of $LiSiNO_{0.50}S_{0.50}$.

A.3 $\mathbf{LiSiNO_{0.25}S_{0.75}}$

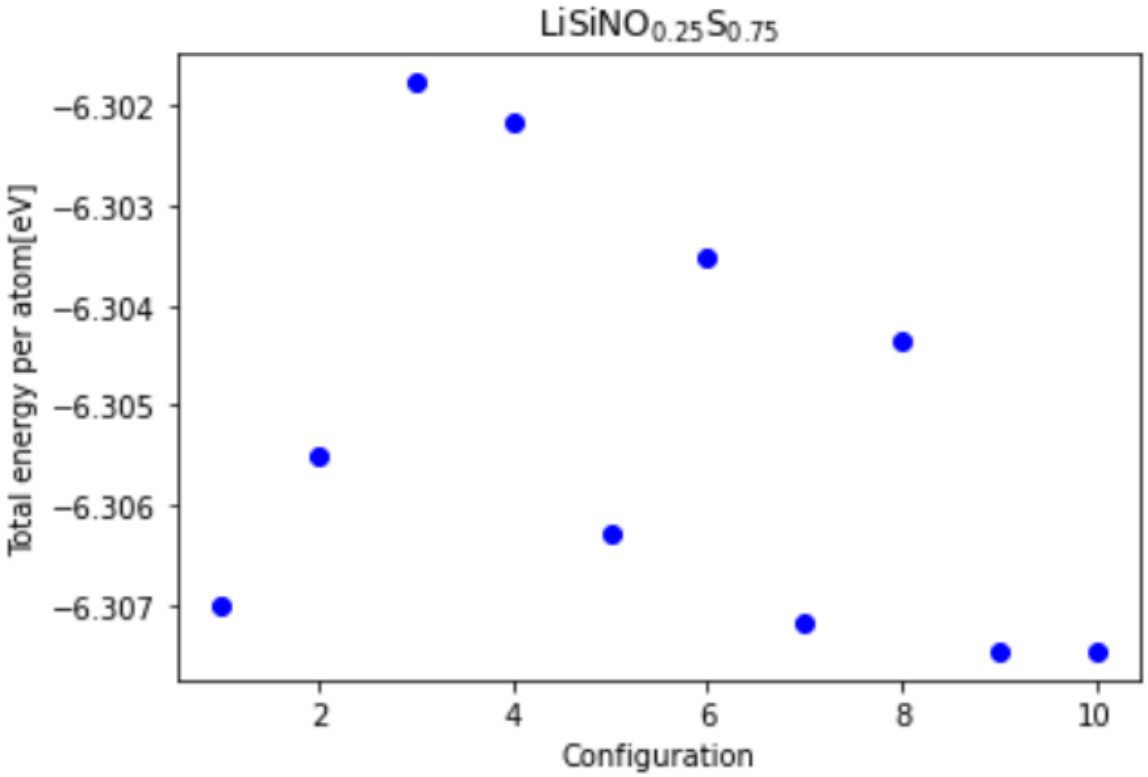

Figure 25: The total energy per atom for each of the ten configurations chosen of $LiSiNO_{0.25}S_{0.75}$.

A.4 $\mathbf{LiSi_{0.75}Ge_{0.25}NO}$

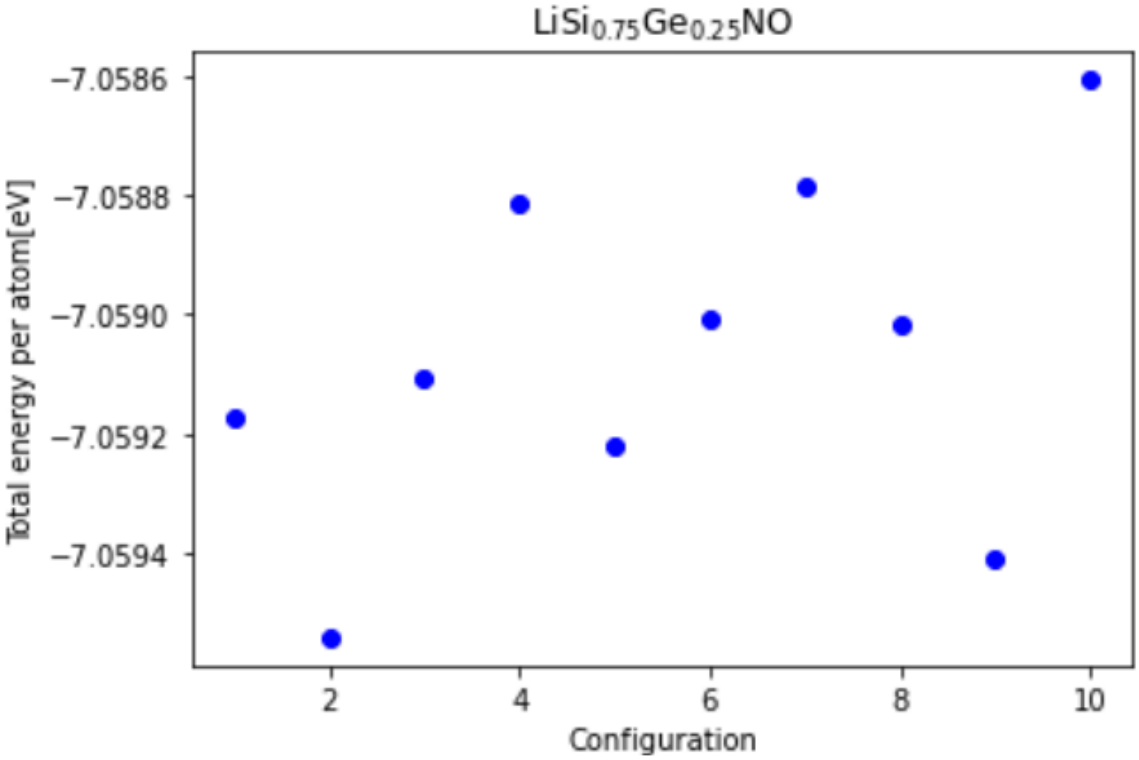

Figure 26: The total energy per atom for each of the ten configurations chosen of $LiSi_{0.75}Ge_{0.25}NO$.

A.5 $LiSi_{0.50}Ge_{0.50}NO$

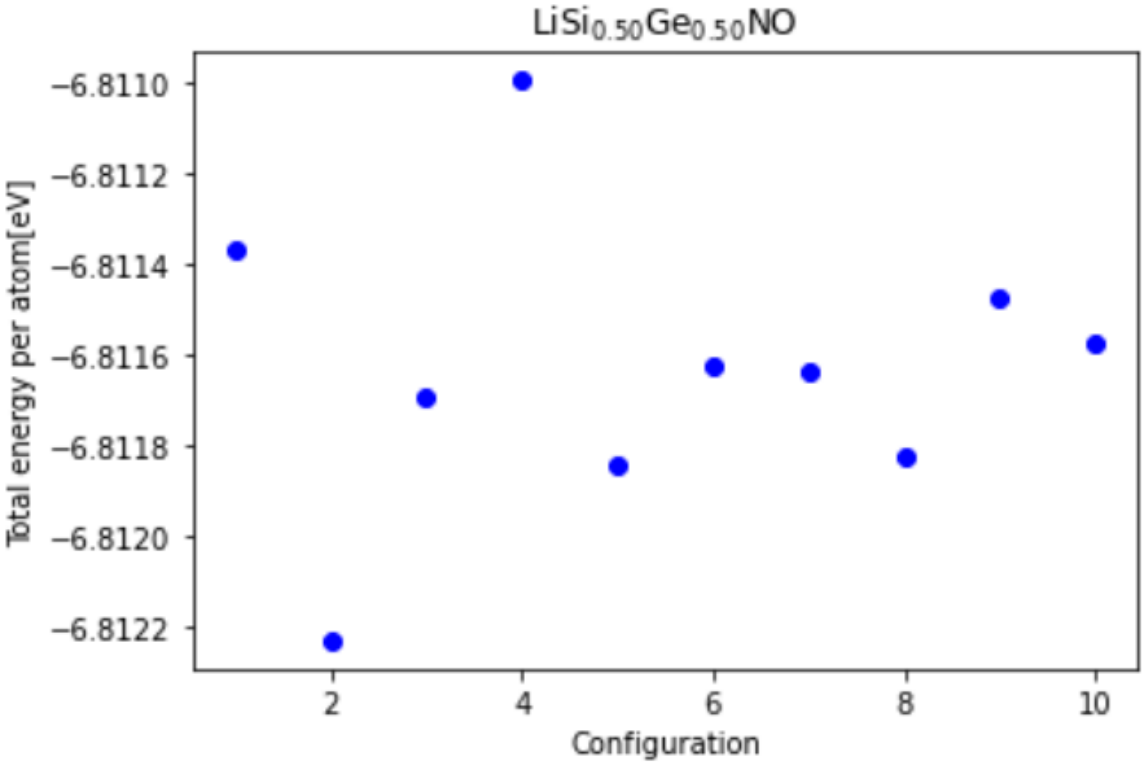

Figure 27: The total energy per atom for each of the ten configurations chosen of $LiSi_{0.50}Ge_{0.50}NO$.

A.6 $LiSi_{0.25}Ge_{0.75}NO$

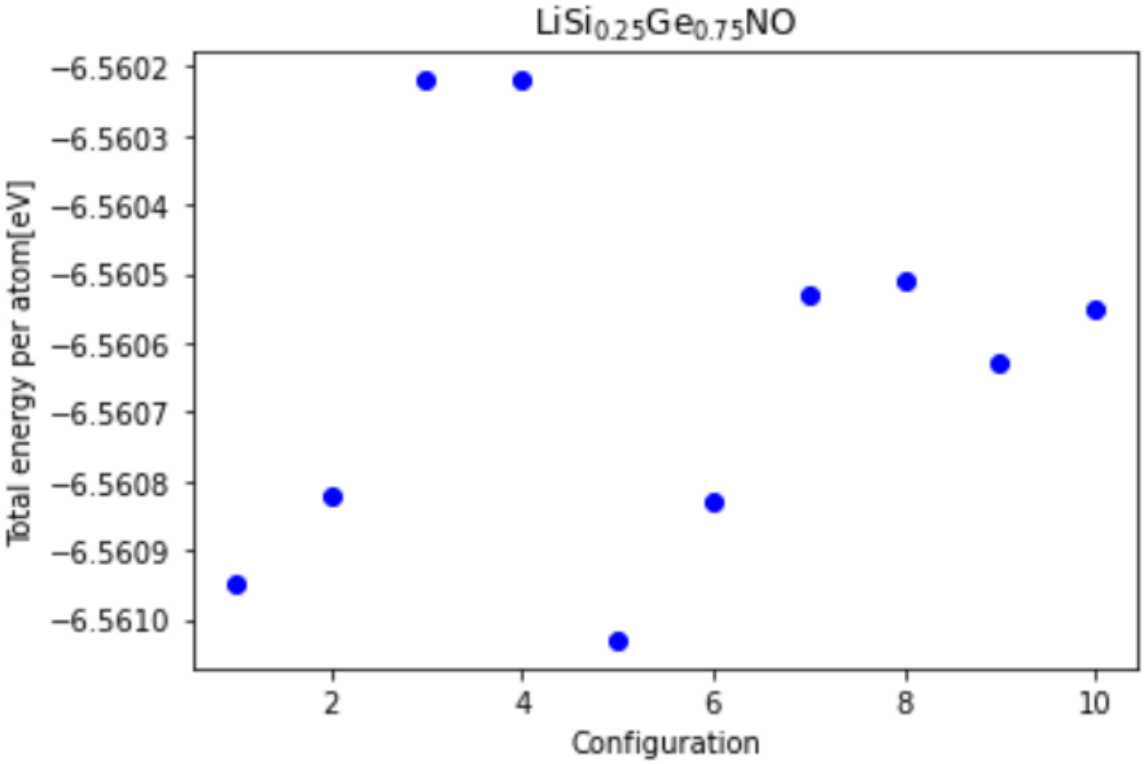

Figure 28: The total energy per atom for each of the ten configurations chosen of $LiSi_{0.25}Ge_{0.75}NO$.

B Density of States plots

The density of states plots for each solid-solution are presented with a legend over each present orbital.

B.1 $LiSiNO_{0.75}S_{0.25}$

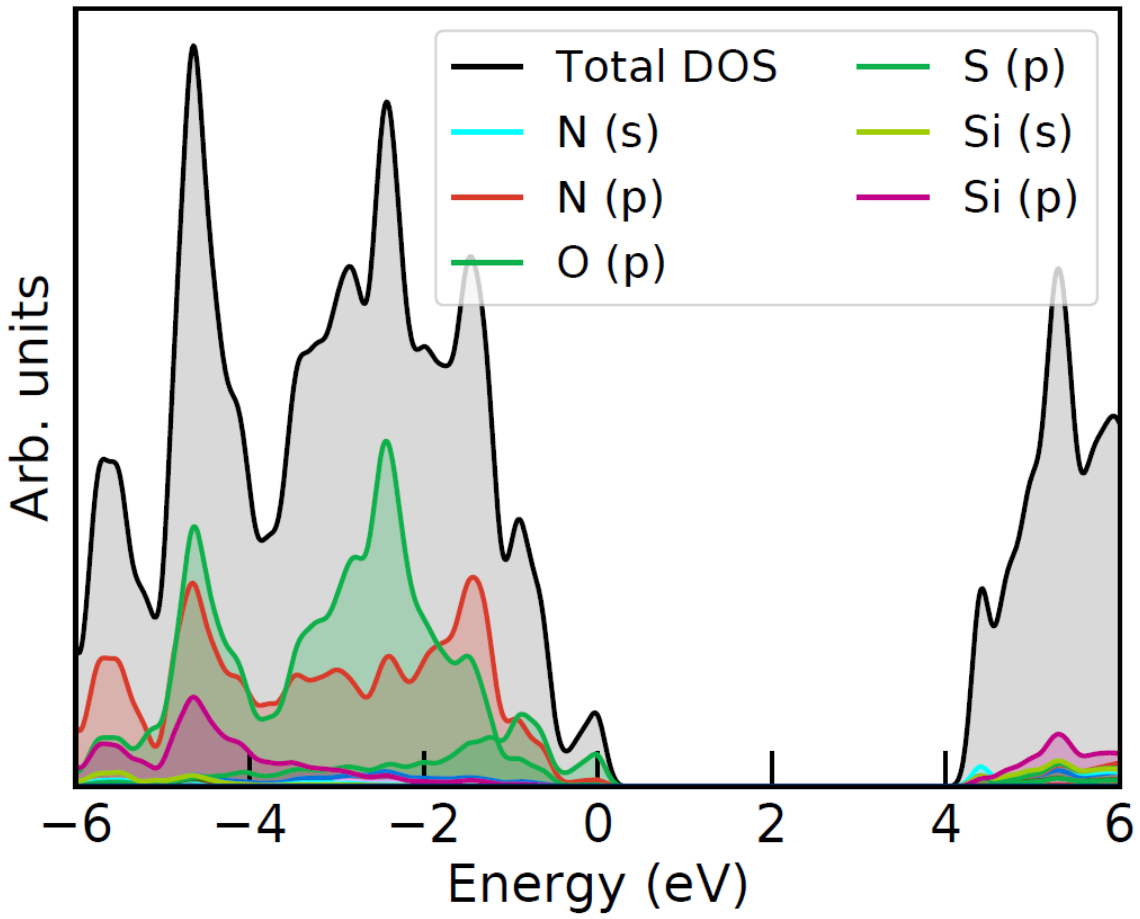

Figure 29: The dos plot for the structure $LiSiNO_{0.75}S_{0.25}$

B.2 $LiSiNO_{0.50}S_{0.50}$

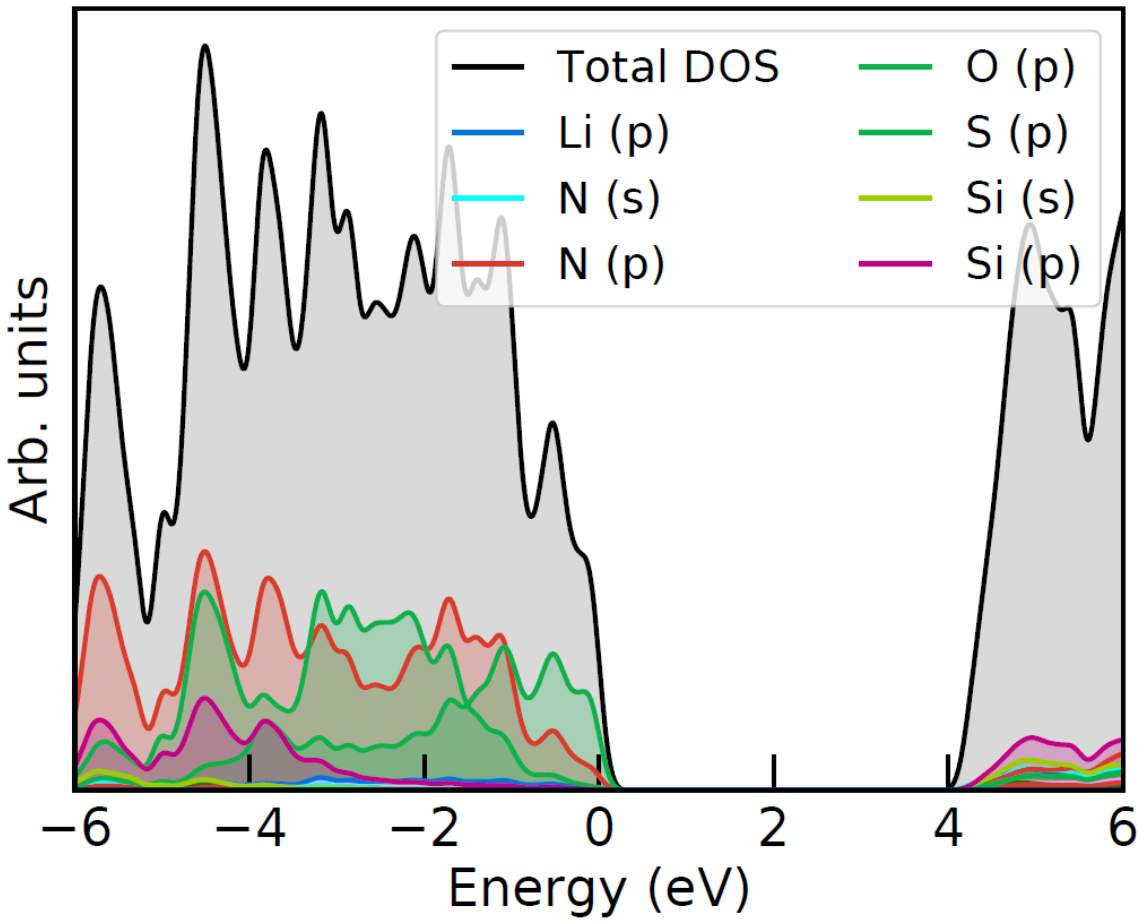

Figure 30: The dos plot for the structure $LiSiNO_{0.50}S_{0.50}$

B.3 $LiSiNO_{0.25}S_{0.75}$

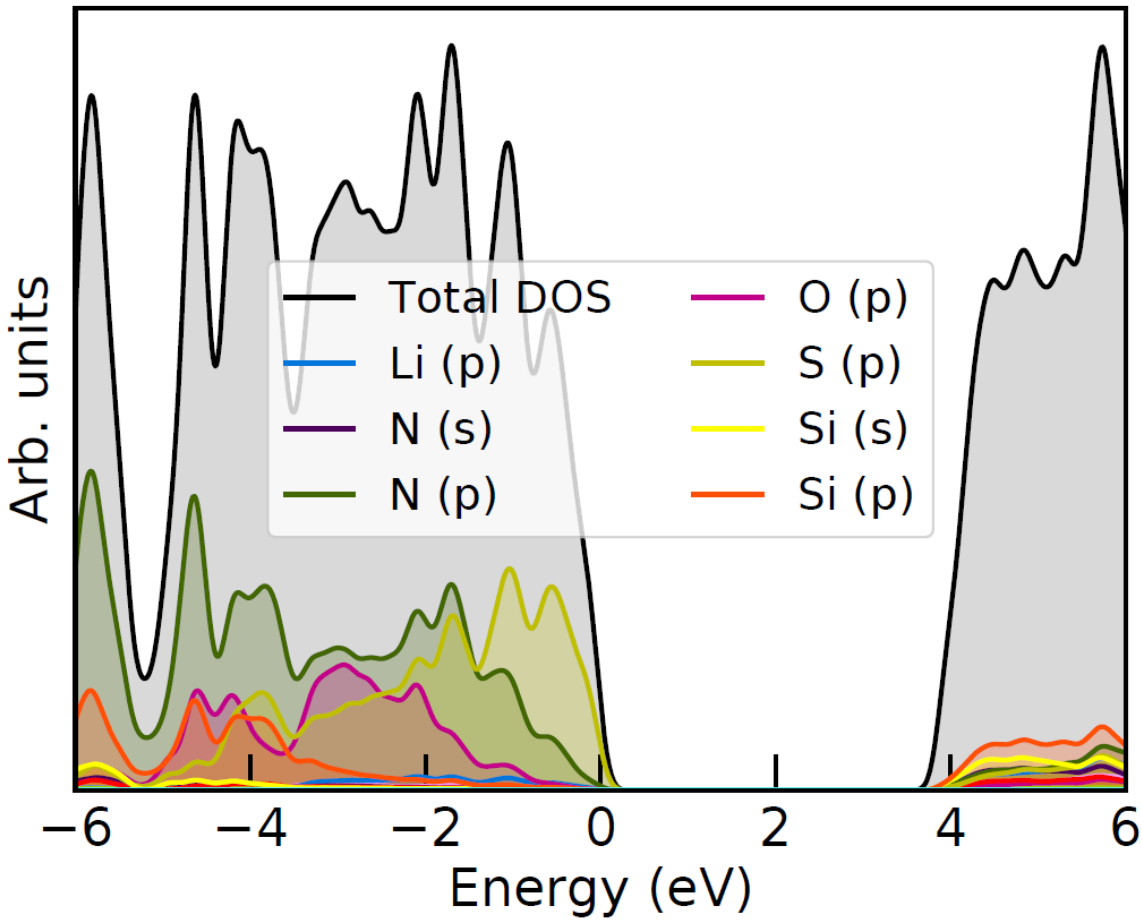

Figure 31: The dos plot for the structure $LiSiNO_{0.25}S_{0.75}$

B.4 $LiSi_{0.75}Ge_{0.25}NO$

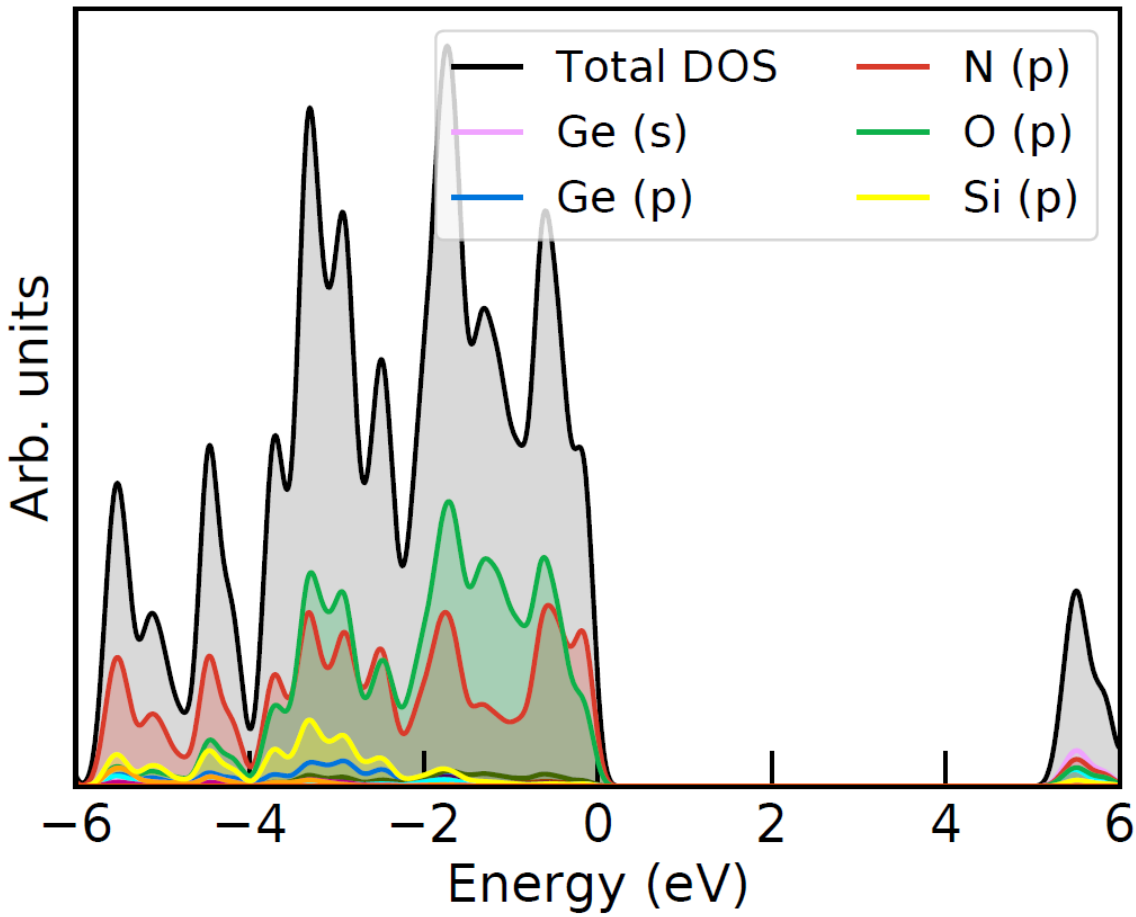

Figure 32: The dos plot for the structure $LiSi_{0.75}Ge_{0.25}NO$

B.5 $LiSi_{0.50}Ge_{0.50}NO$

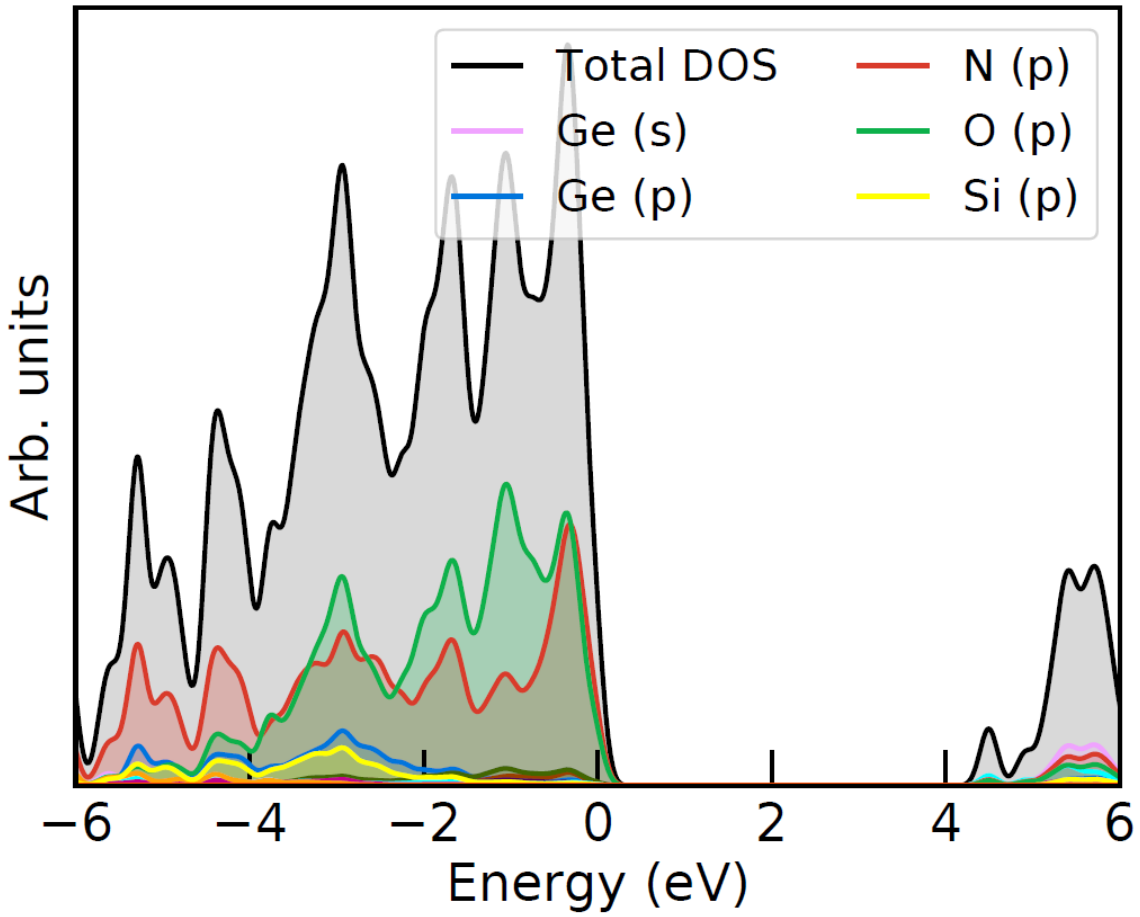

Figure 33: The dos plot for the structure $LiSi_{0.50}Ge_{0.50}NO$

B.6 $LiSi_{0.25}Ge_{0.75}NO$

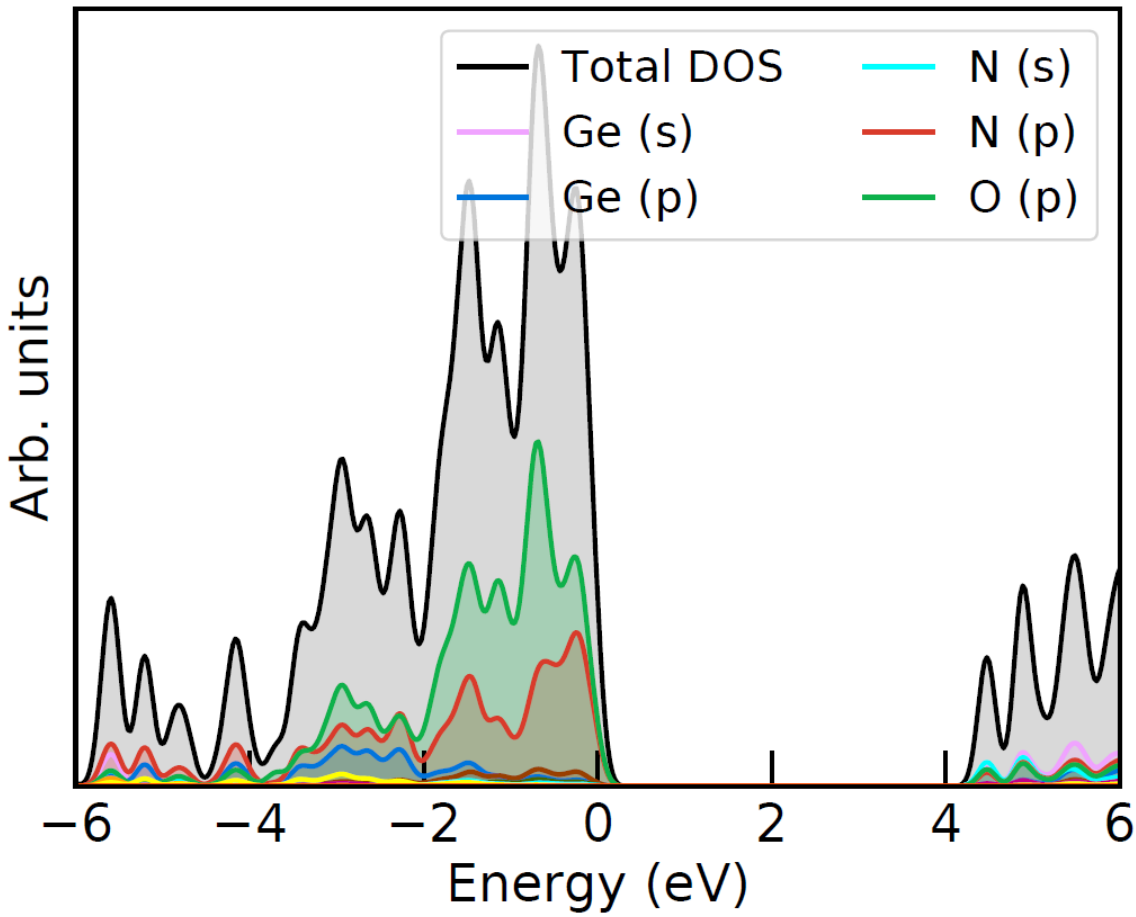

Figure 34: The dos plot for the structure $LiSi_{0.25}Ge_{0.75}NO$

C Bayesian error of short term MD

The bayesian error for the simulated 100 ps for all 9 structures are presented.

C.1 LiSiNO

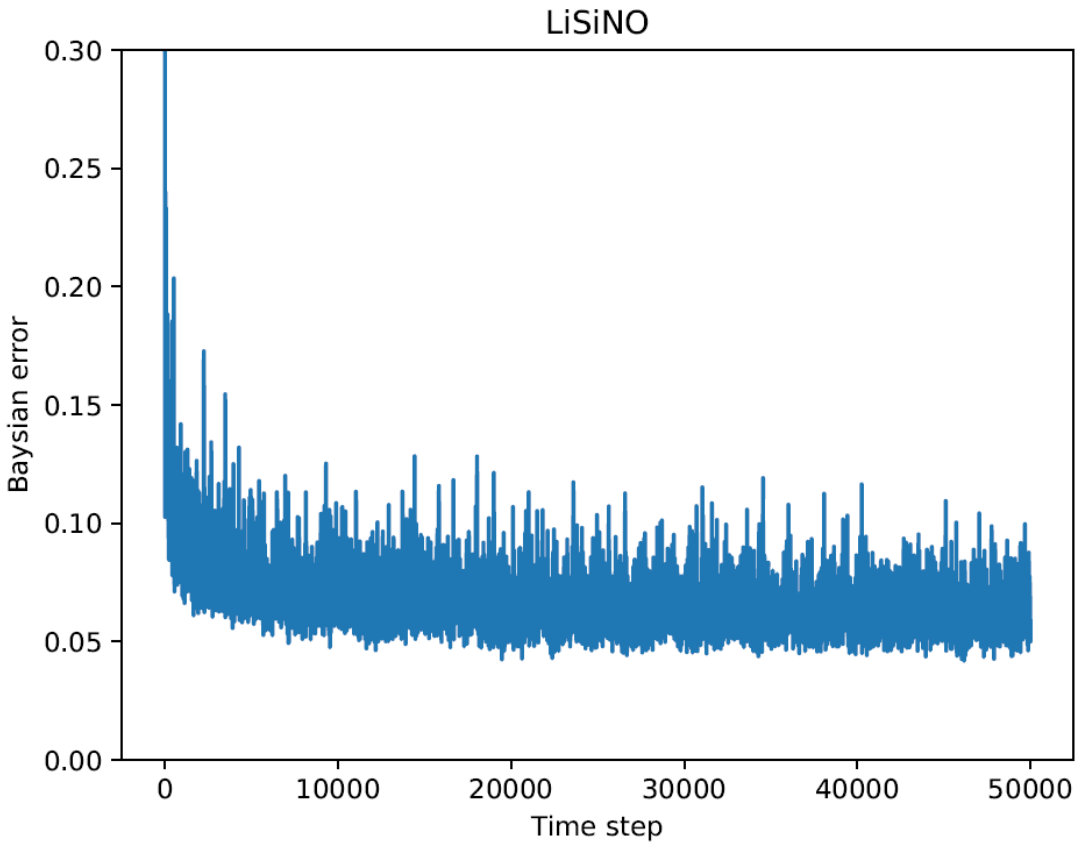

Figure 35: The bayesian error for the 100 ps calculated ML-MD simulations for LiSiNO.

C.2 $\mathbf{LiSiNO_{0.75}S_{0.25}}$

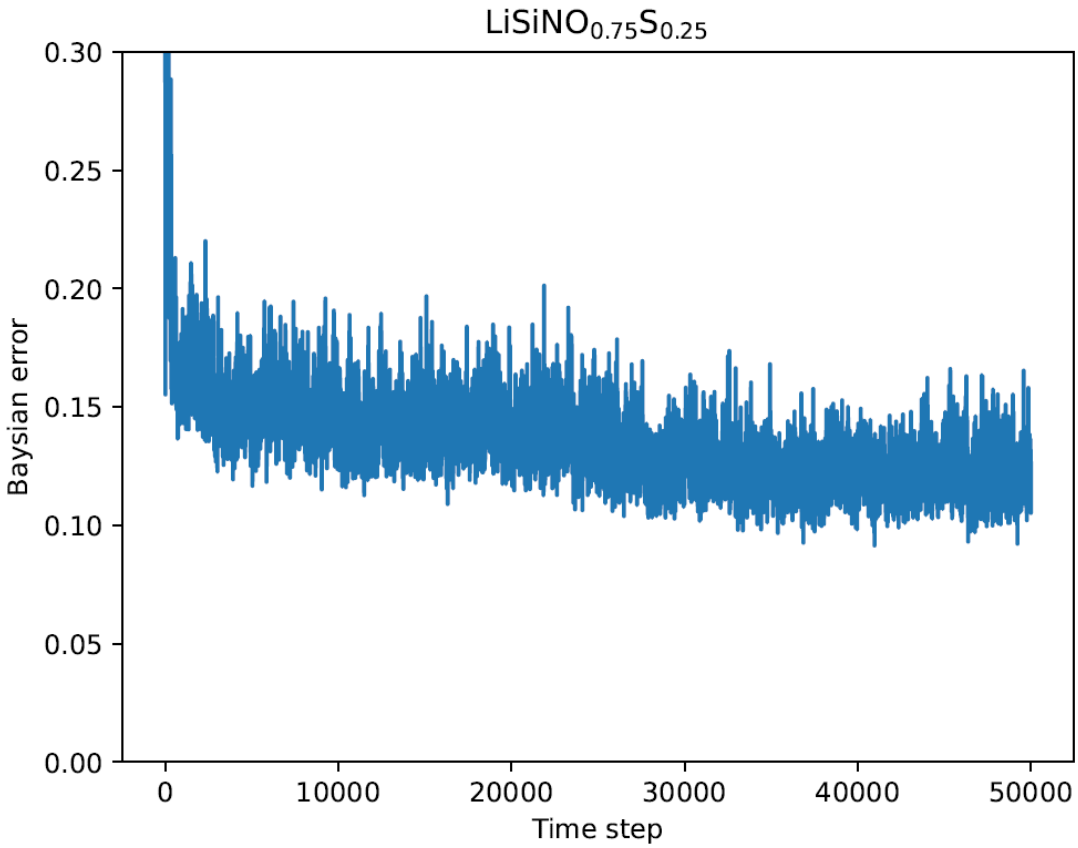

Figure 36: The bayesian error for the 100 ps calculated ML-MD simulations for $LiSiNO_{0.75}S_{0.25}$.

C.3 $\mathbf{LiSiNO_{0.50}S_{0.50}}$

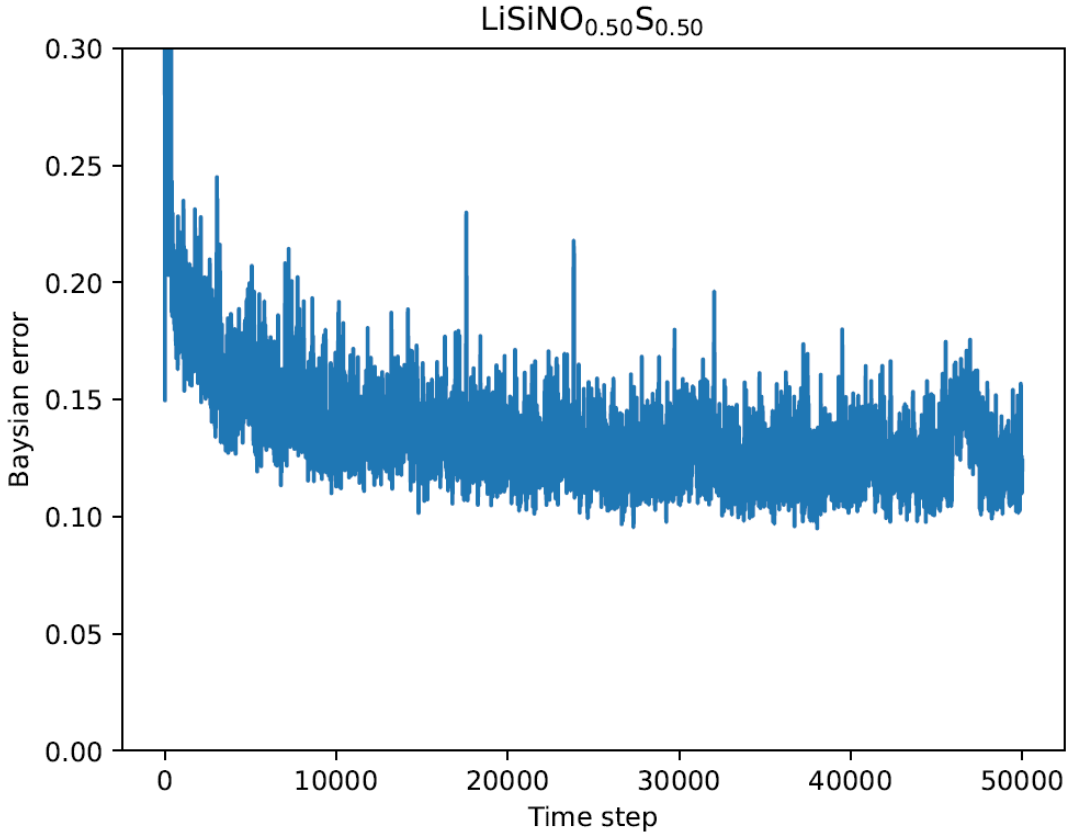

Figure 37: The bayesian error for the 100 ps calculated ML-MD simulations for $LiSiNO_{0.50}S_{0.50}$.

C.4 $\mathbf{LiSiNO_{0.25}S_{0.75}}$

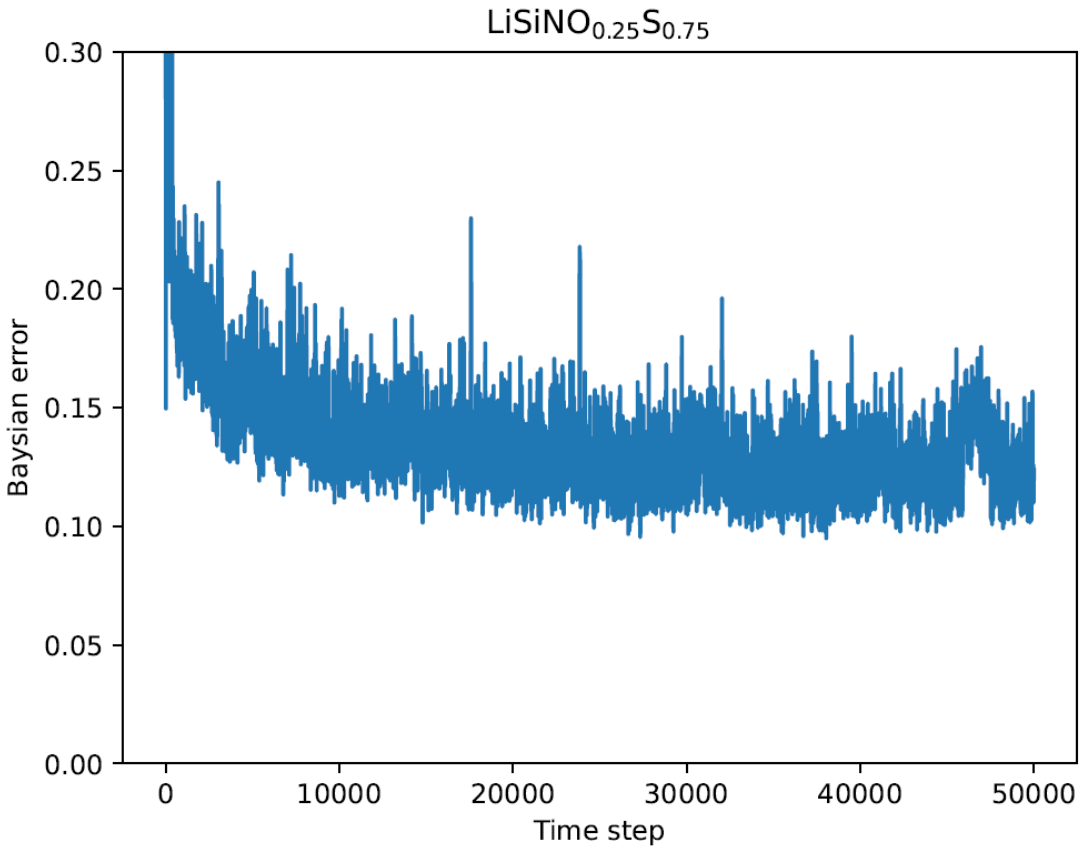

Figure 38: The bayesian error for the 100 ps calculated ML-MD simulations for $LiSiNO_{0.25}S_{0.75}$.

C.5 LiSiNS

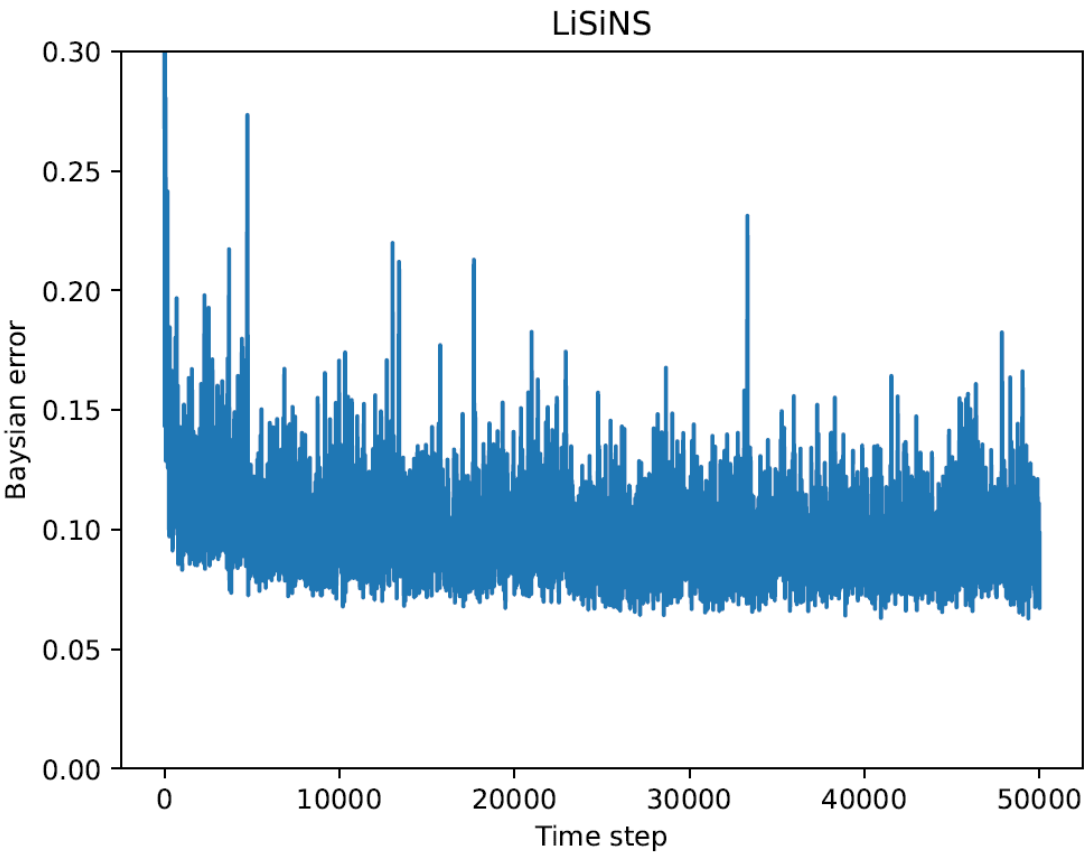

Figure 39: The bayesian error for the 100 ps calculated ML-MD simulations for LiSiNS.

C.6 $LiSi_{0.75}Ge_{0.25}NO$

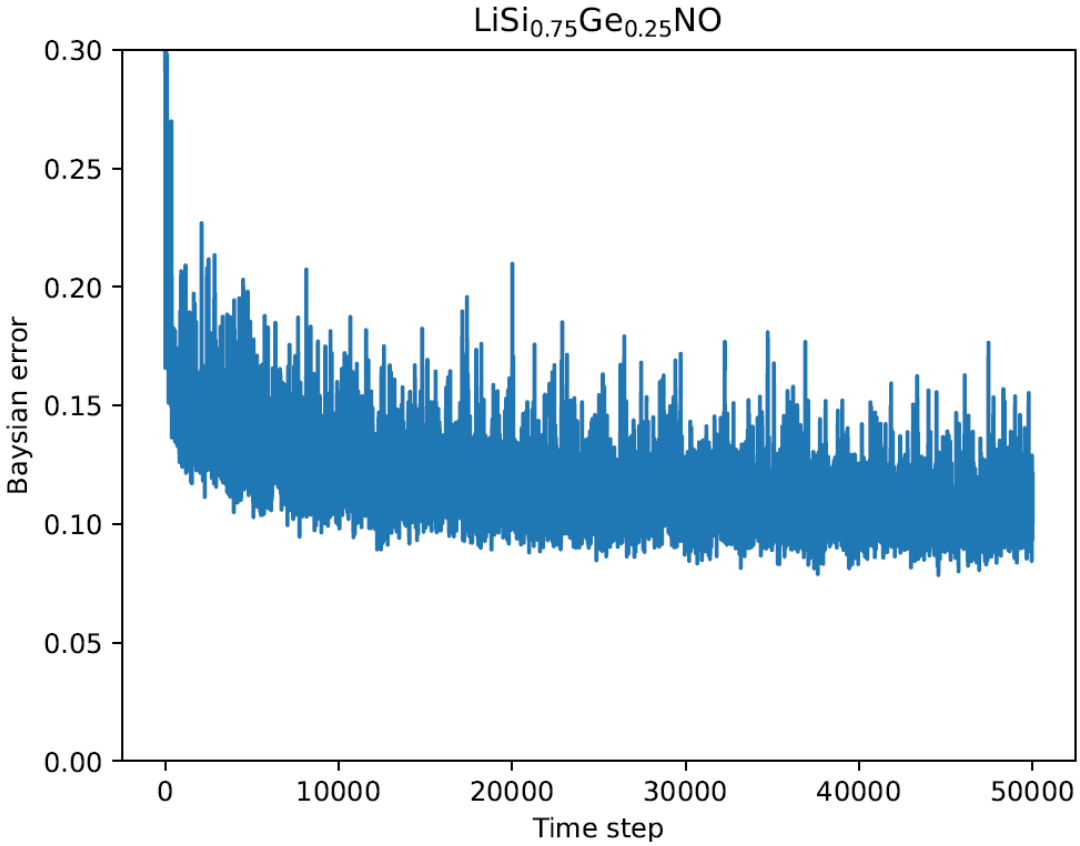

Figure 40: The bayesian error for the 100 ps calculated ML-MD simulations for $LiSi_{0.75}Ge_{0.25}NO$.

C.7 $\mathbf{LiSi_{0.50}Ge_{0.50}NO}$

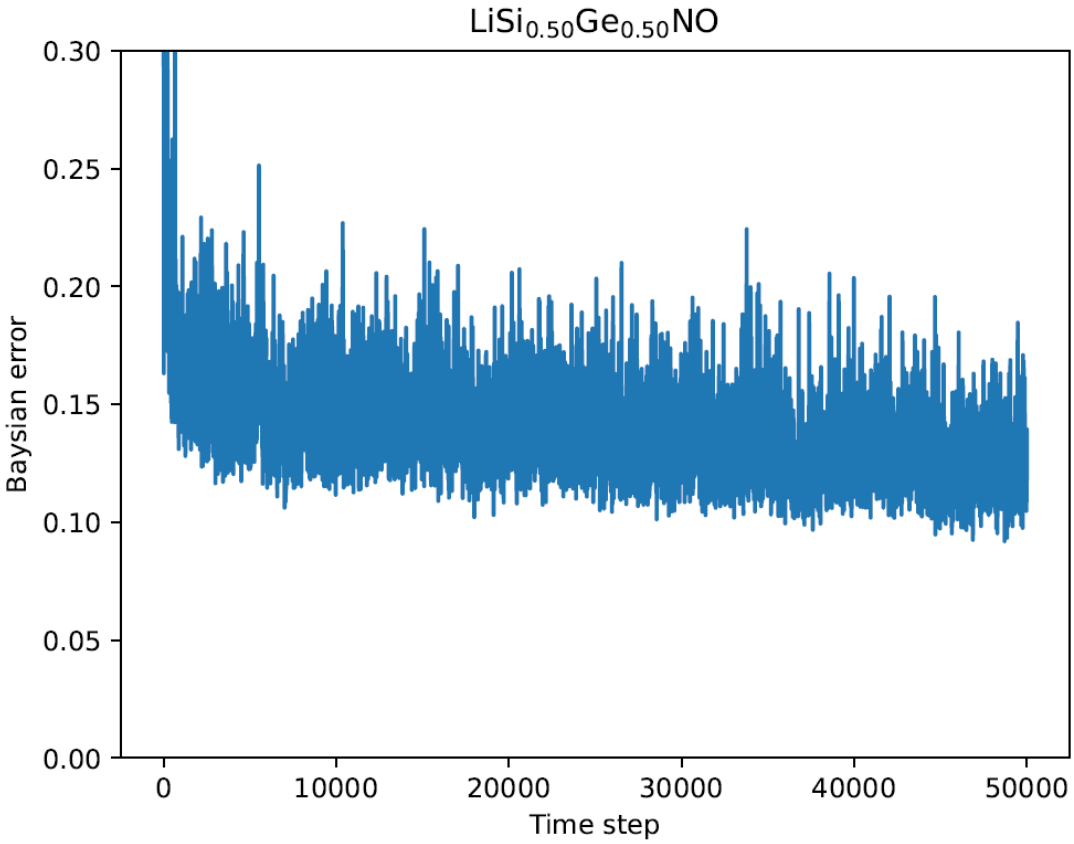

Figure 41: The bayesian error for the 100 ps calculated ML-MD simulations for $LiSi_{0.50}Ge_{0.50}NO$.

C.8 $\mathbf{LiSi_{0.25}Ge_{0.75}NO}$

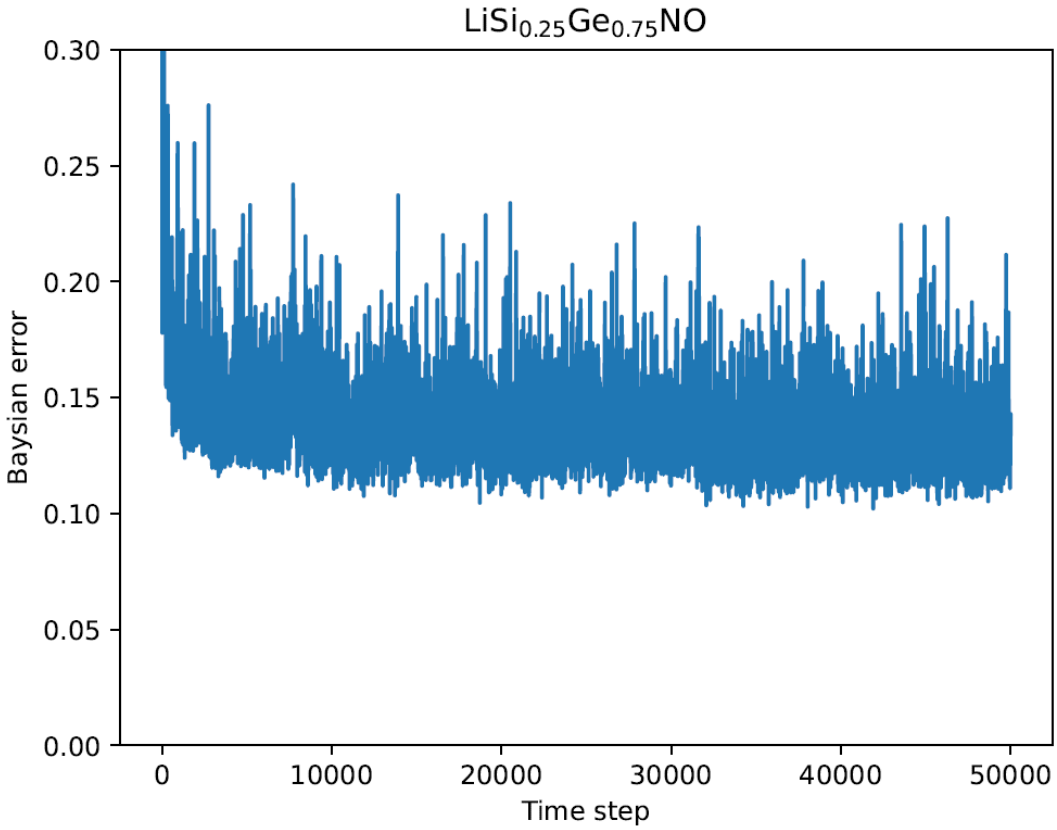

Figure 42: The bayesian error for the 100 ps calculated ML-MD simulations for $LiSi_{0.25}Ge_{0.75}NO$.

C.9 LiGeNO

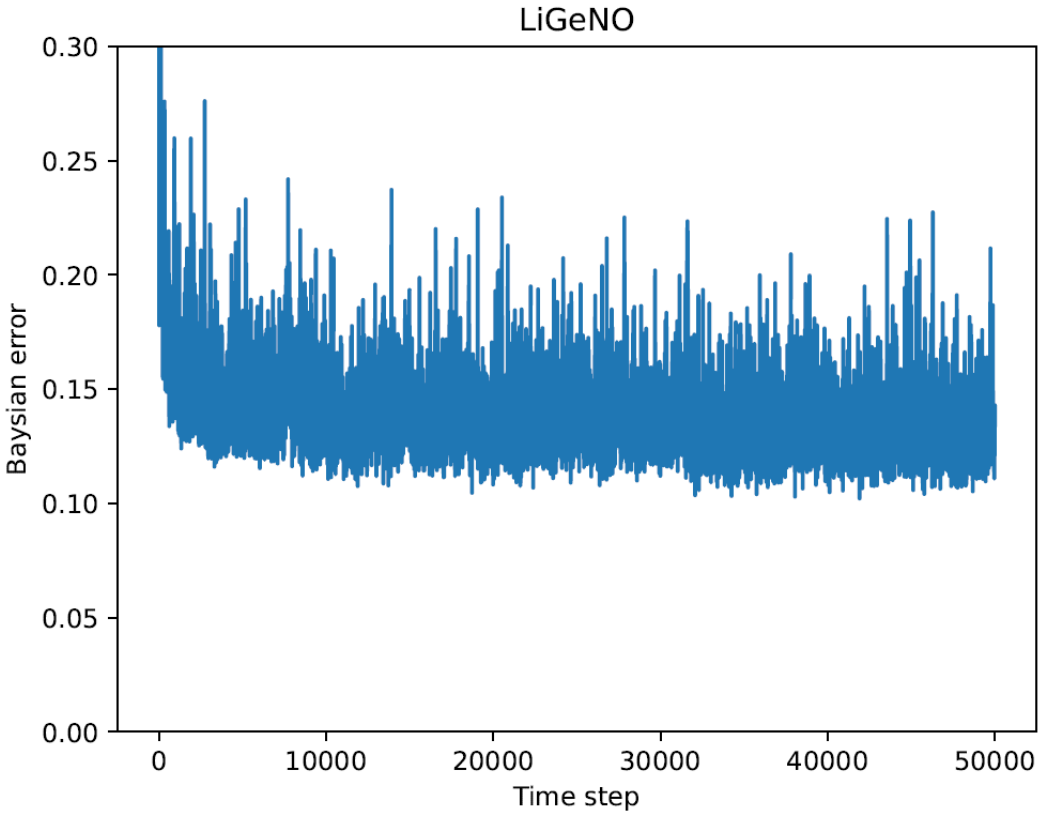

Figure 43: The bayesian error for the 100 ps calculated ML-MD simulations for LiGeNO.

D MSD measurement of the long term MD simulations

The MSD are plotted against the simulated time for all the long term ML-MD simulations.

D.1 LiSiNO

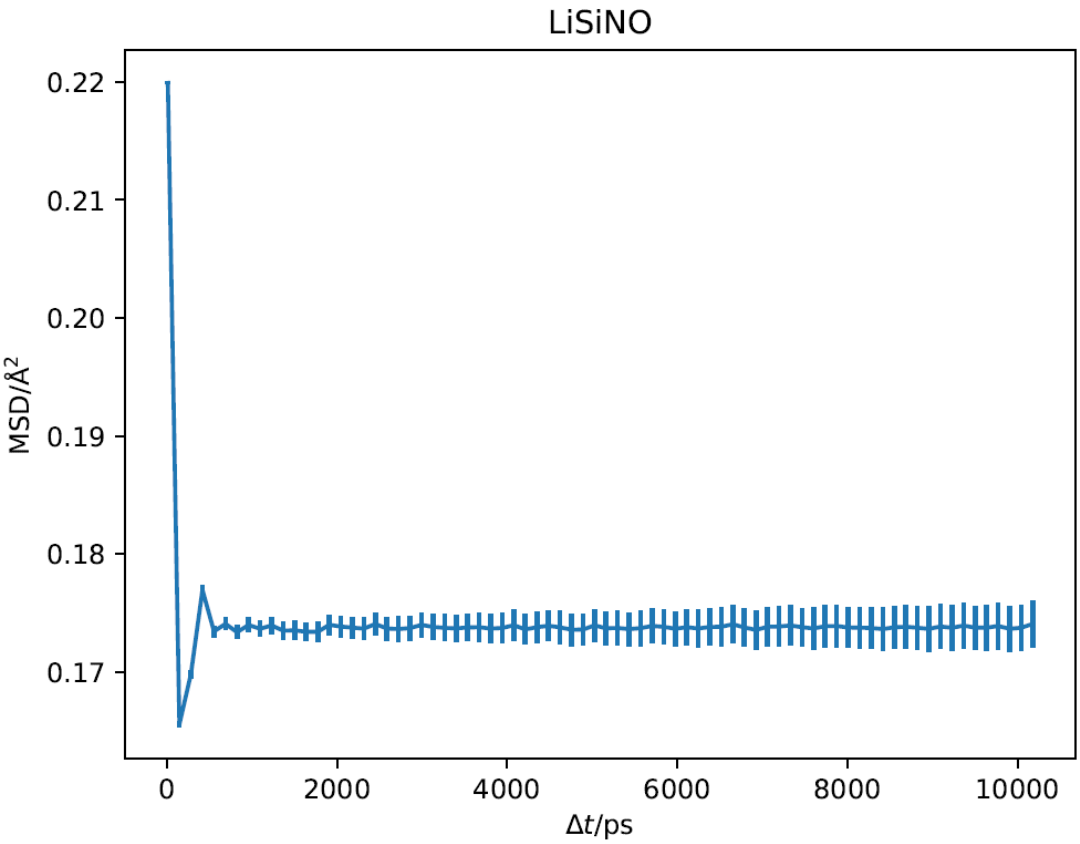

Figure 44: The calculated MSD for the long term MD simulation of LiSiNO plotted against the simulated time.

D.2 $\mathbf{LiSiNO_{0.75}S_{0.25}}$

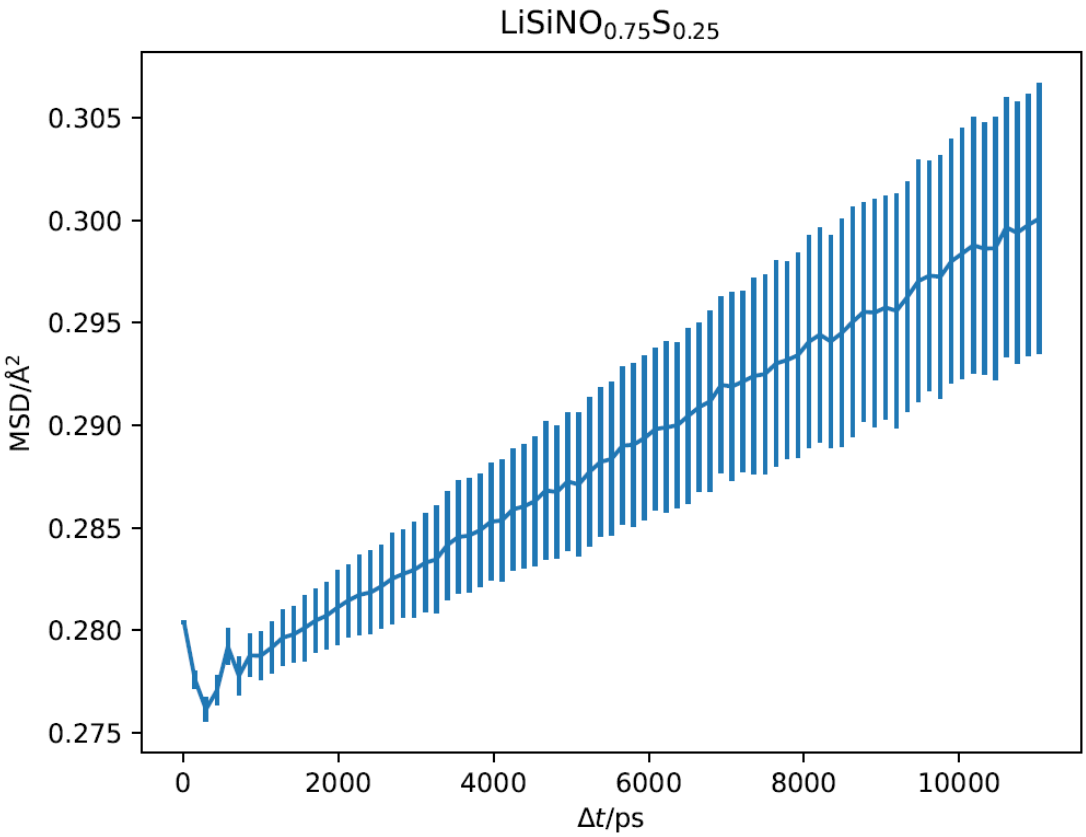

Figure 45: The calculated MSD for the long term MD simulation of $LiSiNO_{0.75}S_{0.25}$ plotted against the simulated time.

D.3 $\mathbf{LiSiNO_{0.50}S_{0.50}}$

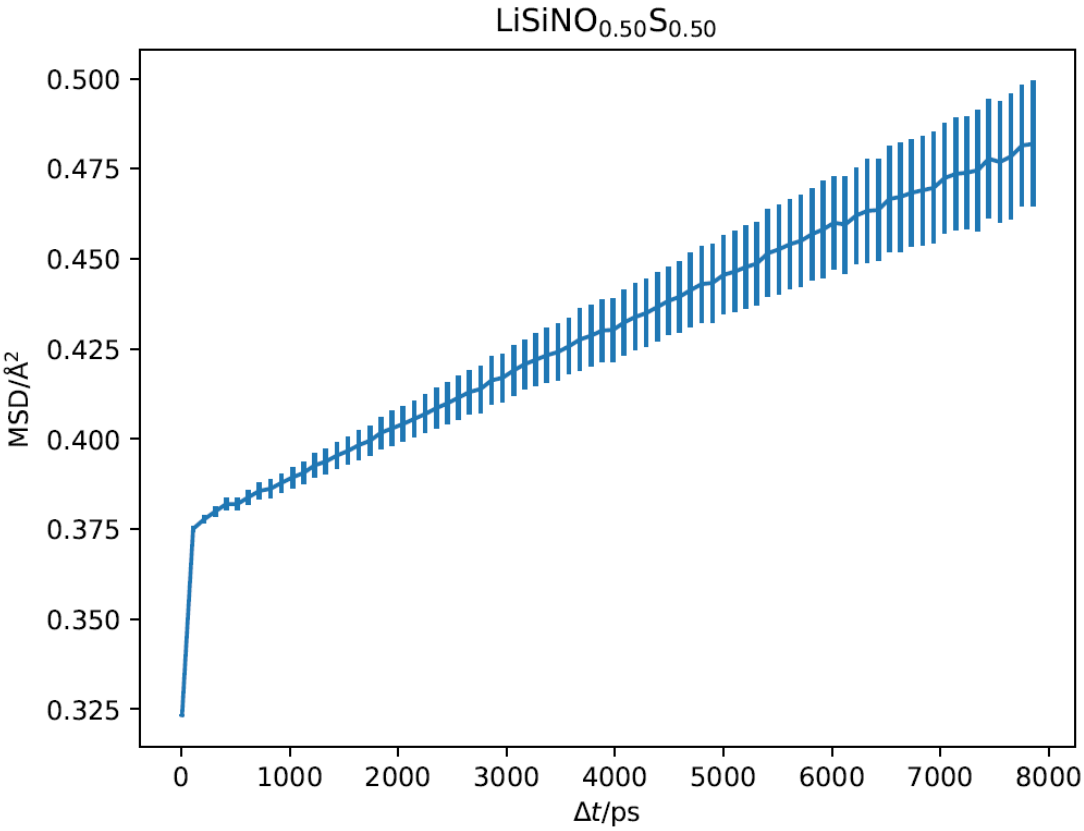

Figure 46: The calculated MSD for the long term MD simulation of $LiSiNO_{0.50}S_{0.50}$ plotted against the simulated time.

D.4 $LiSiNO_{0.25}S_{0.75}$

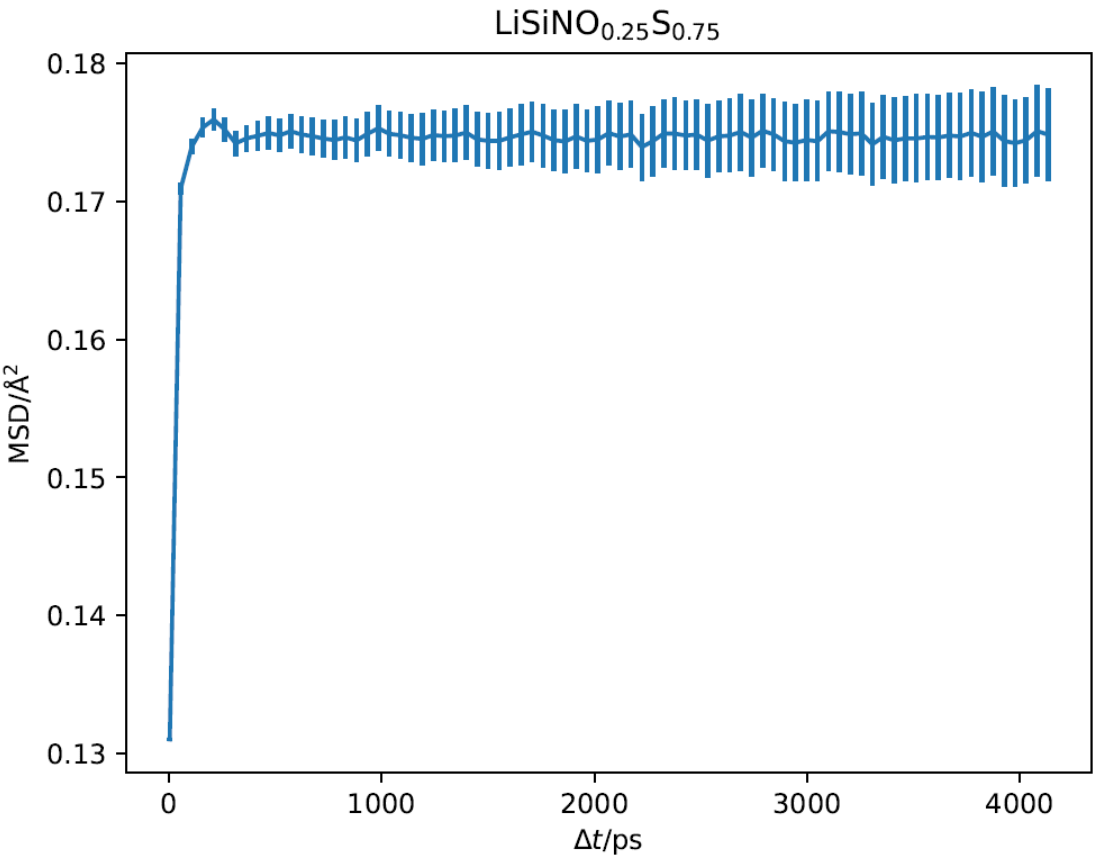

Figure 47: The calculated MSD for the long term MD simulation of $LiSiNO_{0.25}S_{0.75}$ plotted against the simulated time.

D.5 LiSiNS

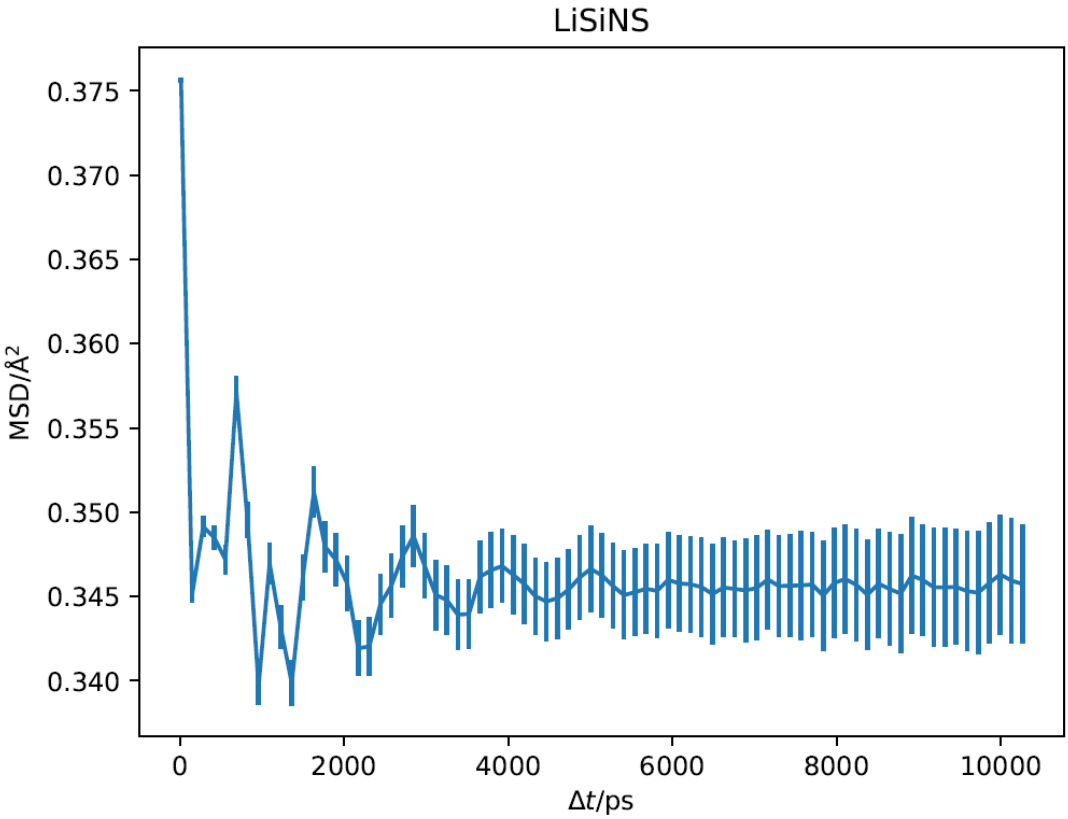

Figure 48: The calculated MSD for the long term MD simulation of LiSiNS plotted against the simulated time.

D.6 $LiSi_{0.75}Ge_{0.25}NO$

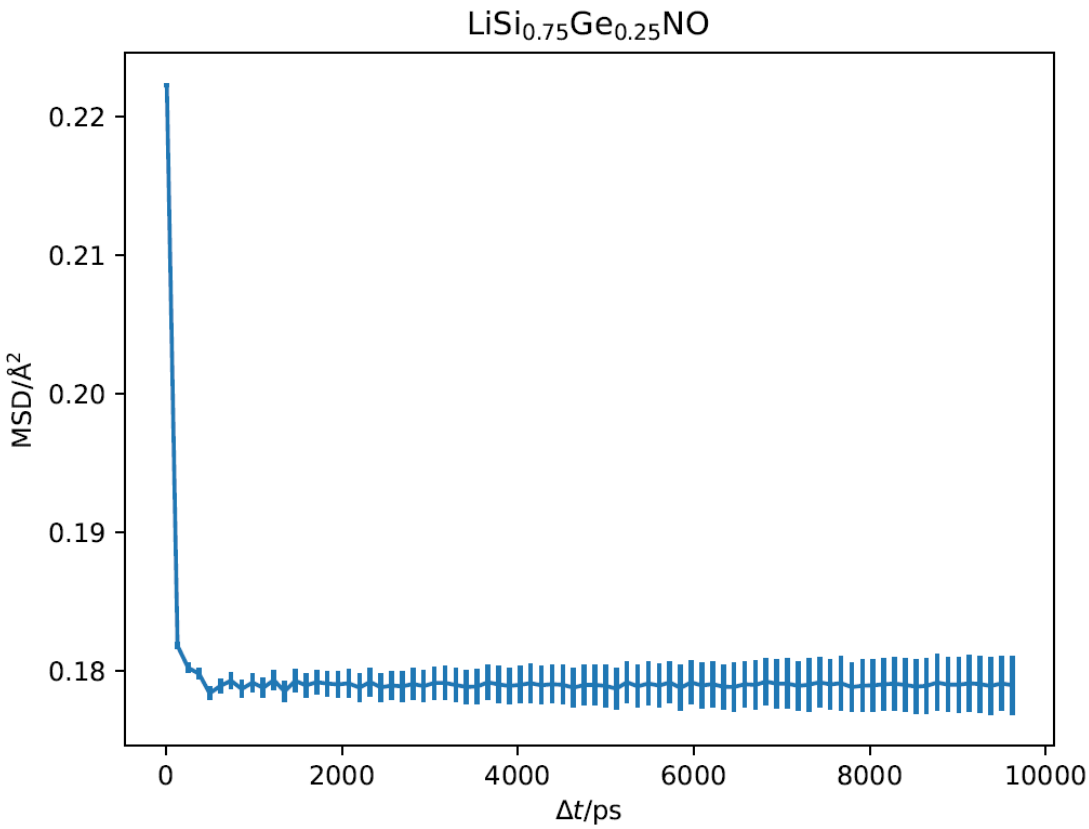

Figure 49: The calculated MSD for the long term MD simulation of $LiSi_{0.75}Ge_{0.25}NO$ plotted against the simulated time.

D.7 $LiSi_{0.50}Ge_{0.50}NO$

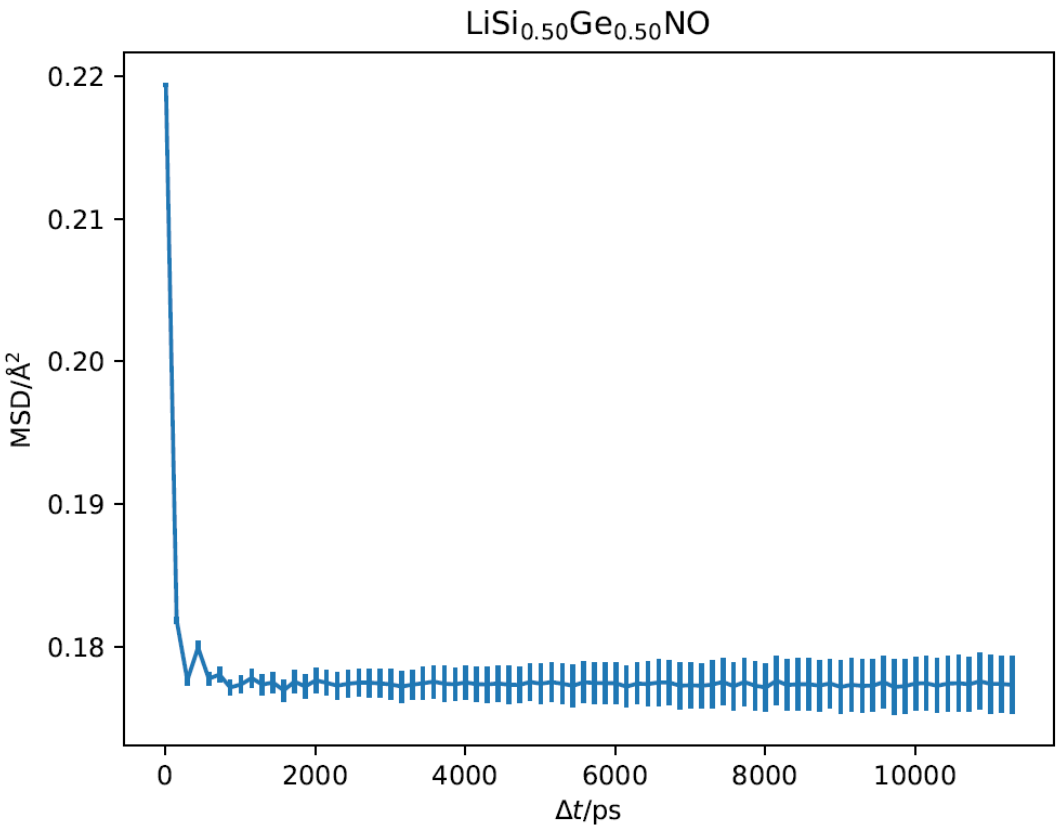

Figure 50: The calculated MSD for the long term MD simulation of $LiSi_{0.50}Ge_{0.50}NO$ plotted against the simulated time.

D.8 LiGeNO

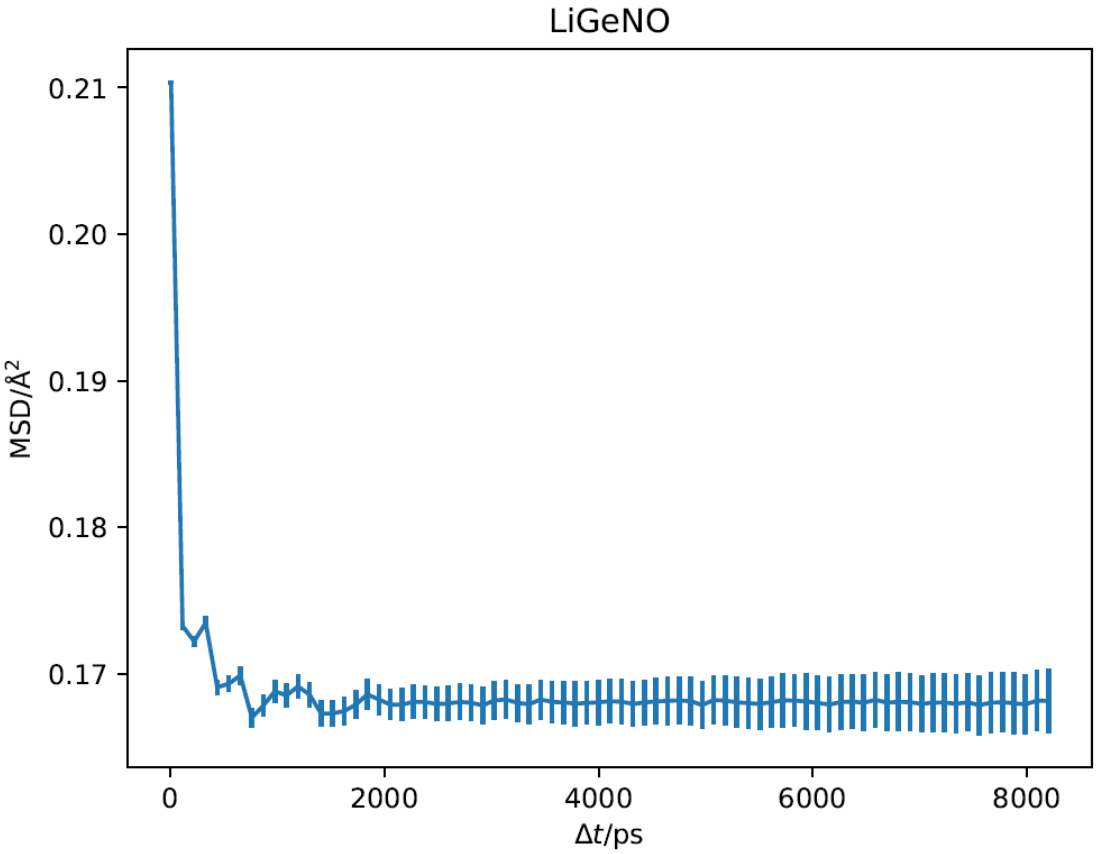

Figure 51: The calculated MSD for the long term MD simulation of LiGeNO plotted against the simulated time.

E INCAR files

E.1 Relaxation of the Supercell

```
SYSTEM = Generic Input

start Parameters
  NWRITE      = 2       ! Medium-level information output
  ISTART      = 1       ! read existing wavefunction; if there
  INIWAV      = 1       ! Random initial wavefunction; otherwise
  ICORELEVEL  = 1       ! Print core levels
  !ICHARG     = 11      ! Non-selfconsistent: GGA/LDA band structures
  !NBANDS     = 130     ! No. bands

parallelisation
  NCORE   = 16          ! No. cores per orbital
  !LPLANE = .TRUE.      ! Real space distribution; supercells
  !KPAR   = 2           ! K-point parallelisation

electronic relaxation
  PREC     = Normal   ! Precision level
  ALGO     = Normal     ! SCF minimisation algorithm; 38/48 combo
  ENMAX    = 500        ! Plane-wave cutoff
  NELM     = 200        ! Max SCF steps
  NELMIN   = 2          ! Min SCF steps
  EDIFF    = 1E-08      ! SCF energy convergence
  GGA      = PS         ! PBEsol exchange-correlation
  LASPH    = .TRUE.     ! Non-spherical elements; d/f convergence
  LREAL    = .FALSE.      ! Projection operators: automatic
  ADDGRID  = .TRUE.     ! Increase grid; helps GGA convergence
  !IVDW = 11            ! Grimme's D3 VDW correction

ionic relaxation
  EDIFFG = -1E-06       ! Ionic convergence; eV/AA^3
  NSW    = 100          ! Max ionic steps
  IBRION = 1            ! Algorithm: 0-MD; 1-Quasi-New; 2-CG
  ISIF   = 2            ! Stress/relaxation: 2-Ions, 3-Shape/Ions/V, 7-Vol
  ISYM   = 0            ! Symmetry: 0-none; 2=GGA; 3=hybrids
  NBLOCK = 1            ! Update XDATCAR every X steps
  KBLOCK = 40           ! Update PCDAT and DOSCAR every X*NBLOCK steps
  ISMEAR = 0            ! Gaussian smearing; metals:1
  SIGMA  = 0.02         ! Smearing value in eV; metals:0.2
  IWAVPR = 1            ! charge density extrapolation: 0-non 1-charg 2-wave 3-comb
  POTIM  = 0.1        ! Timestep in fs

misc
  LORBIT  = 11          ! PAW radii for projected DOS
```

```
  NEDOS    = 2000        ! DOSCAR points

magnetic
  ISPIN    = 2           ! Enable spin polarisation
```

E.2 Calculation of Density of States with PBEsol functional

```
SYSTEM = Generic Input

start Parameters
  NWRITE      = 2       ! Medium-level information output
  ISTART      = 1       ! read existing wavefunction; if there
  INIWAV      = 1       ! Random initial wavefunction; otherwise
  ICORELEVEL  = 1       ! Print core levels
  !ICHARG     = 11      ! Non-selfconsistent: GGA/LDA band structures
  !NBANDS     = 130     ! No. bands

parallelisation
  NCORE   = 16          ! No. cores per orbital
  !LPLANE = .TRUE.      ! Real space distribution; supercells
  !KPAR   = 2           ! K-point parallelisation

electronic relaxation
  PREC     = Normal   ! Precision level
  ALGO     = Normal     ! SCF minimisation algorithm; 38/48 combo
  ENMAX    = 500        ! Plane-wave cutoff
  NELM     = 200        ! Max SCF steps
  NELMIN   = 2          ! Min SCF steps
  EDIFF    = 1E-08      ! SCF energy convergence
  GGA      = PS         ! PBEsol exchange-correlation
  LASPH    = .TRUE.     ! Non-spherical elements; d/f convergence
  LREAL    = .FALSE.      ! Projection operators: automatic
  ADDGRID  = .TRUE.     ! Increase grid; helps GGA convergence
  !IVDW = 11            ! Grimme's D3 VDW correction

ionic relaxation
  EDIFFG = -1E-06       ! Ionic convergence; eV/AA^3
  NSW    = 0          ! Max ionic steps
  IBRION = 1          ! Algorithm: 0-MD; 1-Quasi-New; 2-CG
  ISIF   = 3          ! Stress/relaxation: 2-Ions, 3-Shape/Ions/V, 7-Vol
  ISYM   = 2          ! Symmetry: 0-none; 2-GGA; 3-hybrids
  NBLOCK = 1          ! Update XDATCAR every X steps
  KBLOCK = 40         ! Update PCDAT and DOSCAR every X*NBLOCK steps
  ISMEAR = -5          ! Gaussian smearing; metals:1
  SIGMA  = 0.02       ! Smearing value in eV; metals:0.2
  IWAVPR = 1          ! charge density extrapolation: 0-non 1-charg 2-wave 3-comb
  POTIM  = 0.1       ! Timestep in fs

misc
  LORBIT  = 11        ! PAW radii for projected DOS
  NEDOS   = 2000      ! DOSCAR points
```

E.3 Calculation of Band Structure with PBEsol functional

```
SYSTEM = Generic Input

start Parameters
  NWRITE      = 2       ! Medium-level information output
  ISTART      = 1       ! read existing wavefunction; if there
  INIWAV      = 1       ! Random initial wavefunction; otherwise
  ICORELEVEL  = 1       ! Print core levels
  !ICHARG     = 11      ! Non-selfconsistent: GGA/LDA band structures
  !NBANDS     = 130     ! No. bands

parallelisation
  NCORE   = 16          ! No. cores per orbital
  !LPLANE = .TRUE.      ! Real space distribution; supercells
  !KPAR   = 2           ! K-point parallelisation

electronic relaxation
  PREC     = Normal   ! Precision level
  ALGO     = Normal     ! SCF minimisation algorithm; 38/48 combo
  ENMAX    = 500        ! Plane-wave cutoff
  NELM     = 200        ! Max SCF steps
  NELMIN   = 2          ! Min SCF steps
  EDIFF    = 1E-08      ! SCF energy convergence
  GGA      = PS         ! PBEsol exchange-correlation
  LASPH    = .TRUE.     ! Non-spherical elements; d/f convergence
  LREAL    = .FALSE.      ! Projection operators: automatic
  ADDGRID  = .TRUE.     ! Increase grid; helps GGA convergence
  !IVDW = 11            ! Grimme's D3 VDW correction

ionic relaxation
  EDIFFG = -1E-06       ! Ionic convergence; eV/AA^3
  NSW    = 0          ! Max ionic steps
  IBRION = 1          ! Algorithm: 0-MD; 1-Quasi-New; 2-CG
  ISIF   = 3          ! Stress/relaxation: 2-Ions, 3-Shape/Ions/V, 7-Vol
  ISYM   = 2          ! Symmetry: 0-none; 2-GGA; 3-hybrids
  NBLOCK = 1          ! Update XDATCAR every X steps
  KBLOCK = 40         ! Update PCDAT and DOSCAR every X*NBLOCK steps
  ISMEAR = -5          ! Gaussian smearing; metals:1
  SIGMA  = 0.02       ! Smearing value in eV; metals:0.2
  IWAVPR = 1          ! charge density extrapolation: 0-non 1-charg 2-wave 3-comb
  POTIM  = 0.1       ! Timestep in fs

misc
  LORBIT  = 11        ! PAW radii for projected DOS
  NEDOS   = 2000      ! DOSCAR points
```

E.4 Relaxation of migration start and end points

```
SYSTEM = Generic Input

start Parameters
  NWRITE      = 2       ! Medium-level information output
  ISTART      = 1       ! read existing wavefunction; if there
  INIWAV      = 1       ! Random initial wavefunction; otherwise
  ICORELEVEL  = 1       ! Print core levels
  !ICHARG     = 11      ! Non-selfconsistent: GGA/LDA band structures
  !NBANDS     = 130     ! No. bands

parallelisation
  NCORE   = 16          ! No. cores per orbital
  !LPLANE = .TRUE.      ! Real space distribution; supercells
  !KPAR   = 2           ! K-point parallelisation

electronic relaxation
  PREC     = Normal   ! Precision level
  ALGO     = Normal     ! SCF minimisation algorithm; 38/48 combo
  ENMAX    = 500        ! Plane-wave cutoff
  NELM     = 200        ! Max SCF steps
  NELMIN   = 2          ! Min SCF steps
  EDIFF    = 1E-05      ! SCF energy convergence
  GGA      = PS         ! PBEsol exchange-correlation
  LASPH    = .TRUE.     ! Non-spherical elements; d/f convergence
  LREAL    = .FALSE.      ! Projection operators: automatic
  ADDGRID  = .TRUE.     ! Increase grid; helps GGA convergence

ionic relaxation
  EDIFFG = 0.01       ! Ionic convergence; eV/AA^3
  NSW    = 340          ! Max ionic steps
  IBRION = 1           ! Algorithm: 0-MD; 1-Quasi-New; 2-CG
  ISIF   = 2           ! Stress/relaxation: 2-Ions, 3-Shape/Ions/V, 7-Vol
  ISYM   = 0           ! Symmetry: 0-none; 2=GGA; 3=hybrids
  NBLOCK = 1           ! Update XDATCAR every X steps
  KBLOCK = 40          ! Update PCDAT and DOSCAR every X*NBLOCK steps
  ISMEAR = 0           ! Gaussian smearing; metals:1
  SIGMA  = 0.02        ! Smearing value in eV; metals:0.2
  IWAVPR = 1           ! charge density extrapolation: 0-non 1-charg 2-wave 3-comb
  POTIM  = 0.1        ! Timestep in fs

misc
  LORBIT  = 11         ! PAW radii for projected DOS
  NEDOS   = 2000       ! DOSCAR points

magnetic
  ISPIN   = 2          ! Enable spin polarisation
```

```
!MAGMOM  = 5 0        ! Initial magnetic momoment on each ion
NUPDOWN = 1          ! Enforce spin multiplet
```

E.5 Relaxation of intermediate images

```
SYSTEM = Generic Input

start Parameters
  NWRITE      = 2       ! Medium-level information output
  ISTART      = 1       ! read existing wavefunction; if there
  INIWAV      = 1       ! Random initial wavefunction; otherwise
  ICORELEVEL  = 1       ! Print core levels
  !ICHARG     = 11      ! Non-selfconsistent: GGA/LDA band structures
  !NBANDS     = 130     ! No. bands

parallelisation
  NCORE   = 16          ! No. cores per orbital
  !LPLANE = .TRUE.      ! Real space distribution; supercells
  !KPAR   = 2           ! K-point parallelisation

electronic relaxation
  PREC     = Normal   ! Precision level
  ALGO     = Normal     ! SCF minimisation algorithm; 38/48 combo
  ENMAX    = 500      ! Plane-wave cutoff
  NELM     = 200        ! Max SCF steps
  NELMIN   = 2          ! Min SCF steps
  EDIFF    = 1E-05      ! SCF energy convergence
  GGA      = PS         ! PBEsol exchange-correlation
  LASPH    = .TRUE.     ! Non-spherical elements; d/f convergence
  LREAL    = .FALSE.      ! Projection operators: automatic
  ADDGRID  = .TRUE.     ! Increase grid; helps GGA convergence
  ionic relaxation
  EDIFFG  = -0.02       ! Ionic convergence; eV/AA^3
  NSW     = 190          ! Max ionic steps
  IBRION  = 1           ! Algorithm: 0-MD; 1-Quasi-New; 2-CG
  ISIF    = 2           ! Stress/relaxation: 2-Ions, 3-Shape/Ions/V, 7-Vol
  ISYM    = 0           ! Symmetry: 0-none; 2-GGA; 3-hybrids
  NBLOCK  = 1           ! Update XDATCAR every X steps
  KBLOCK  = 40          ! Update PCDAT and DOSCAR every X*NBLOCK steps
  ISMEAR  = 0           ! Gaussian smearing; metals:1
  SIGMA   = 0.02        ! Smearing value in eV; metals:0.2
  IWAVPR  = 1           ! charge density extrapolation: 0-non 1-charg 2-wave 3-comb
  POTIM   = 0.1        ! Timestep in fs

misc
  LORBIT   = 11         ! PAW radii for projected DOS
  NEDOS    = 2000       ! DOSCAR points
  !LVHAR   = .TRUE.     ! Ionic and Hartree potential
  !RWIGS   = 1.5 1.5    ! Radii for each atomic species
  !LOPTICS = .TRUE.     ! Output OPTIC file
  LVTOT    = .TRUE.     ! Electrostatic potential
```

```
  !LELF    = .TRUE.     ! Localisation function
  LCLIMB = .TRUE. ! turns on the "climbing image, i.e. one image is always at the
  ↪  top of the barrier"
  IMAGES = 5 ! number of images
  ICHAIN = 0 ! can't remember what this does
  SPRING = -5 ! spring constant between the images, -5 always seems to work

magnetic
  ISPIN    = 2          ! Enable spin polarisation
  !MAGMOM  = 5 0        ! Initial magnetic momoment on each ion
  NUPDOWN = 1          ! Enforce spin multiplet
```

E.6 Warm up, Short term MD

```
SYSTEM = Generic Input

start Parameters
  NWRITE      = 2       ! Medium-level information output
  ISTART      = 1       ! read existing wavefunction; if there
  INIWAV      = 1       ! Random initial wavefunction; otherwise
  ICORELEVEL  = 1       ! Print core levels
  !ICHARG     = 11      ! Non-selfconsistent: GGA/LDA band structures
  !NBANDS     = 130     ! No. bands

parallelisation
  NCORE   = 16          ! No. cores per orbital
  !LPLANE = .TRUE.      ! Real space distribution; supercells
  !KPAR   = 2           ! K-point parallelisation

electronic relaxation
  PREC     = low   ! Precision level
  ALGO     = Normal      ! SCF minimisation algorithm; 38/48 combo
  ENMAX    = 500         ! Plane-wave cutoff
  NELM     = 200         ! Max SCF steps
  NELMIN   = 2           ! Min SCF steps
  EDIFF    = 1E-04       ! SCF energy convergence
  GGA      = PS          ! PBEsol exchange-correlation
  LASPH    = .TRUE.      ! Non-spherical elements; d/f convergence
  LREAL    = Auto        ! Projection operators: automatic
  ADDGRID  = .TRUE.      ! Increase grid; helps GGA convergence
  !IVDW = 11            ! Grimme's D3 VDW correction
  LWAVE = .FALSE.
  LCHARG = .FALSE.


ionic relaxation
  EDIFFG = -0.02        ! Ionic convergence; eV/AA^3
  NSW    = 2000           ! Max ionic steps
  IBRION = 0            ! Algorithm: 0-MD; 1-Quasi-New; 2-CG
  ISIF   = 2            ! Stress/relaxation: 2-Ions, 3-Shape/Ions/V, 7-Vol
  ISYM   = 0            ! Symmetry: 0-none; 2=GGA; 3=hybrids
  NBLOCK = 1            ! Update XDATCAR every X steps
  KBLOCK = 40           ! Update PCDAT and DOSCAR every X*NBLOCK steps
  ISMEAR = 0            ! Gaussian smearing; metals:1
  SIGMA  = 0.02         ! Smearing value in eV; metals:0.2
  IWAVPR = 1            ! charge density extrapolation: 0-non 1-charg 2-wave 3-comb
  POTIM  = 2        ! Timestep in fs

#Machine learning paramters
  ML_LMLFF = .TRUE.
```

```
  ML_ISTART = 0

misc
  !LORBIT  = 11          ! PAW radii for projected DOS
  !NEDOS   = 2000        ! DOSCAR points
  MDALGO = 2            ! NVT
  SMASS = 1.0
  TEBEG = 0            ! Beginning T
  TEEND = 800
```

E.7 Equilibrium run, Short term MD

```
SYSTEM = Generic Input

start Parameters
  NWRITE      = 2       ! Medium-level information output
  ISTART      = 1       ! read existing wavefunction; if there
  INIWAV      = 1       ! Random initial wavefunction; otherwise
  ICORELEVEL  = 1       ! Print core levels
  !ICHARG     = 11      ! Non-selfconsistent: GGA/LDA band structures
  !NBANDS     = 130     ! No. bands

parallelisation
  NCORE   = 16          ! No. cores per orbital
  !LPLANE = .TRUE.      ! Real space distribution; supercells
  !KPAR   = 2           ! K-point parallelisation

electronic relaxation
  PREC     = low   ! Precision level
  ALGO     = Normal      ! SCF minimisation algorithm; 38/48 combo
  ENMAX    = 500         ! Plane-wave cutoff
  NELM     = 200         ! Max SCF steps
  NELMIN   = 2           ! Min SCF steps
  EDIFF    = 1E-04       ! SCF energy convergence
  GGA      = PS          ! PBEsol exchange-correlation
  LASPH    = .TRUE.      ! Non-spherical elements; d/f convergence
  LREAL    = Auto        ! Projection operators: automatic
  ADDGRID  = .TRUE.      ! Increase grid; helps GGA convergence
  !IVDW = 11            ! Grimme's D3 VDW correction
  LWAVE = .FALSE.
  LCHARG = .FALSE.


ionic relaxation
  EDIFFG = -0.02        ! Ionic convergence; eV/AA^3
  NSW    = 2000           ! Max ionic steps
  IBRION = 0            ! Algorithm: 0-MD; 1-Quasi-New; 2-CG
  ISIF   = 2            ! Stress/relaxation: 2-Ions, 3-Shape/Ions/V, 7-Vol
  ISYM   = 0            ! Symmetry: 0-none; 2=GGA; 3=hybrids
  NBLOCK = 1            ! Update XDATCAR every X steps
  KBLOCK = 40           ! Update PCDAT and DOSCAR every X*NBLOCK steps
  ISMEAR = 0            ! Gaussian smearing; metals:1
  SIGMA  = 0.02         ! Smearing value in eV; metals:0.2
  IWAVPR = 1            ! charge density extrapolation: 0-non 1-charg 2-wave 3-comb
  POTIM  = 2        ! Timestep in fs

#Machine learning paramters
  ML_LMLFF = .TRUE.
```

```
  ML_ISTART = 0

misc
  !LORBIT  = 11          ! PAW radii for projected DOS
  !NEDOS   = 2000        ! DOSCAR points
  MDALGO = 2            ! NVT
  SMASS = 1.0
  TEBEG = 800           ! Beginning T
  TEEND = 800
```

E.8 Production run, Short term MD

```
SYSTEM = Generic Input

start Parameters
  NWRITE      = 2       ! Medium-level information output
  ISTART      = 1       ! read existing wavefunction; if there
  INIWAV      = 1       ! Random initial wavefunction; otherwise
  ICORELEVEL  = 1       ! Print core levels
  !ICHARG     = 11      ! Non-selfconsistent: GGA/LDA band structures
  !NBANDS     = 130     ! No. bands

parallelisation
  NCORE   = 16          ! No. cores per orbital
  !LPLANE = .TRUE.      ! Real space distribution; supercells
  !KPAR   = 2           ! K-point parallelisation

electronic relaxation
  PREC     = low   ! Precision level
  ALGO     = Normal      ! SCF minimisation algorithm; 38/48 combo
  ENMAX    = 500         ! Plane-wave cutoff
  NELM     = 200         ! Max SCF steps
  NELMIN   = 2           ! Min SCF steps
  EDIFF    = 1E-04       ! SCF energy convergence
  GGA      = PS          ! PBEsol exchange-correlation
  LASPH    = .TRUE.      ! Non-spherical elements; d/f convergence
  LREAL    = Auto        ! Projection operators: automatic
  ADDGRID  = .TRUE.      ! Increase grid; helps GGA convergence
  !IVDW = 11            ! Grimme's D3 VDW correction
  LWAVE = .FALSE.
  LCHARG = .FALSE.


ionic relaxation
  EDIFFG = -0.02        ! Ionic convergence; eV/AA^3
  NSW    = 50000          ! Max ionic steps
  IBRION = 0            ! Algorithm: 0-MD; 1-Quasi-New; 2-CG
  ISIF   = 2            ! Stress/relaxation: 2-Ions, 3-Shape/Ions/V, 7-Vol
  ISYM   = 0            ! Symmetry: 0-none; 2=GGA; 3=hybrids
  NBLOCK = 1            ! Update XDATCAR every X steps
  KBLOCK = 40           ! Update PCDAT and DOSCAR every X*NBLOCK steps
  ISMEAR = 0            ! Gaussian smearing; metals:1
  SIGMA  = 0.02         ! Smearing value in eV; metals:0.2
  IWAVPR = 1            ! charge density extrapolation: 0-non 1-charg 2-wave 3-comb
  POTIM  = 2        ! Timestep in fs

#Machine learning paramters
  ML_LMLFF = .TRUE.
```

```
  ML_ISTART = 0

misc
  !LORBIT  = 11          ! PAW radii for projected DOS
  !NEDOS   = 2000        ! DOSCAR points
  MDALGO = 2            ! NVT
  SMASS = 1.0
  TEBEG = 800           ! Beginning T
  TEEND = 800
```

E.9 Long term MD

```
SYSTEM = Generic Input

start Parameters
  NWRITE      = 2       ! Medium-level information output
  ISTART      = 1       ! read existing wavefunction; if there
  INIWAV      = 1       ! Random initial wavefunction; otherwise
  ICORELEVEL  = 1       ! Print core levels
  !ICHARG     = 11      ! Non-selfconsistent: GGA/LDA band structures
  !NBANDS     = 130     ! No. bands

parallelisation
  NCORE   = 16          ! No. cores per orbital
  !LPLANE = .TRUE.      ! Real space distribution; supercells
  !KPAR   = 2           ! K-point parallelisation

electronic relaxation
  PREC     = low   ! Precision level
  ALGO     = Normal      ! SCF minimisation algorithm; 38/48 combo
  ENMAX    = 500         ! Plane-wave cutoff
  NELM     = 200         ! Max SCF steps
  NELMIN   = 2           ! Min SCF steps
  EDIFF    = 1E-04       ! SCF energy convergence
  GGA      = PS          ! PBEsol exchange-correlation
  LASPH    = .TRUE.      ! Non-spherical elements; d/f convergence
  LREAL    = Auto        ! Projection operators: automatic
  ADDGRID  = .TRUE.      ! Increase grid; helps GGA convergence
  !IVDW = 11            ! Grimme's D3 VDW correction
  LWAVE = .FALSE.
  LCHARG = .FALSE.


ionic relaxation
  EDIFFG = -0.02        ! Ionic convergence; eV/AA^3
  NSW    = 2000000          ! Max ionic steps
  IBRION = 0            ! Algorithm: 0-MD; 1-Quasi-New; 2-CG
  ISIF   = 2            ! Stress/relaxation: 2-Ions, 3-Shape/Ions/V, 7-Vol
  ISYM   = 0            ! Symmetry: 0-none; 2=GGA; 3=hybrids
  NBLOCK = 1            ! Update XDATCAR every X steps
  KBLOCK = 40           ! Update PCDAT and DOSCAR every X*NBLOCK steps
  ISMEAR = 0            ! Gaussian smearing; metals:1
  SIGMA  = 0.02         ! Smearing value in eV; metals:0.2
  IWAVPR = 1            ! charge density extrapolation: 0-non 1-charg 2-wave 3-comb
  POTIM  = 2        ! Timestep in fs

#Machine learning paramters
  ML_LMLFF = .TRUE.
```

```
  ML_ISTART = 1

misc
  !LORBIT  = 11          ! PAW radii for projected DOS
  !NEDOS   = 2000        ! DOSCAR points
  MDALGO = 2            ! NVT
  SMASS = 1.0
  TEBEG = 800           ! Beginning T
  TEEND = 800
```

Vegard Vesterdal Viki

Computational Prediction and Characterisation of Novel Li-ion Solid Electrolytes based on Earth Abundant LiSiNO

NTNU
Norwegian University of
Science and Technology